Master's Programme in Electronics and Nanotechnology

Multiwavelength Spectral Analysis of Accretion Disk and Astrophysical Jet Connection in Low-Mass X-ray Binaries

Moniaallonpituustutkimus kertymäkiekon ja astrofysikaalisen hiukkassuihkun välisestä yhteydestä matalamassaisissa röntgenkaksoistähdissä

Alexandros Binios

Aalto University
School of Electrical
Engineering

MASTER'S
THESIS

Multiwavelength Spectral Analysis of Accretion Disk and Astrophysical Jet Connection in Low-Mass X-ray Binaries

Alexandros Binios

School of Electrical Engineering

Thesis submitted for examination for the degree of Master of Science in Technology.
Helsinki 28.9.2020

Supervisor

Prof. Anne Lähteenmäki

Advisor

Ph.D. Karri I. I. Koljonen

Aalto University
School of Electrical
Engineering

Aalto University, P.O. BOX 11000, 00076 AALTO
www.aalto.fi
Abstract of the master's thesis

Author Alexandros Binios

Title Multiwavelength Spectral Analysis of Accretion Disk and Astrophysical Jet Connection in Low-Mass X-ray Binaries

Degree programme Master's Programme in Electronics and Nanotechnology

Major Space Science and Technology **Code of major** ELEC3039

Supervisor Prof. Anne Lähteenmäki

Advisor Ph.D. Karri I. I. Koljonen

Date 28.9.2020 **Number of pages** 110+13 **Language** English

Abstract

X-ray binaries (XRBs) are powerful double star systems where a normal star feeds through accretion a compact object, e.g. a black hole, and the liberation of accretion energy results in strong radiation throughout the electromagnetic spectrum. Performing simultaneous multiwavelength observations of XRBs allow us to study their fundamental astrophysical properties and processes, which are ultimately governed by the mass flow rate from the donor star to the accretor. The primary objective of this master's thesis was to perform multiwavelength spectral studies of known XRBs focusing on the accretion disk and astrophysical jet connection, i.e. the disk–jet connection, and to determine their spectral models and states at different observation periods. The data sets used in this master's thesis comprised of (quasi-)simultaneous multiwavelength observations. The principal instrument of this thesis was the Very Large Telescope's X-shooter, and its observations constituted the foundation of the collected (quasi-)simultaneous data sets. This thesis examines four different low-mass X-ray binary (LMXB) targets including MAXI J1820+070, a recently discovered LMXB.

This master's thesis ultimately presents novel and unprecedented broadband observations and results for the main target MAXI J1820+070. Based on the spectral modelling of the observations, the results show how the MAXI J1820+070 first was in the low/hard state in mid-April 2018, then had entered the high/soft state in following observations in mid-July 2018, and finally in late September had transitioned to the intermediate-hard state. During mid-April 2018, the astrophysical jets were dominating and extended from the radio to the near-infrared spectrum. In mid-July, the astrophysical jets were no longer detected, and the accretion disk governed the emission spectrum in the X-shooter band. Additionally, this master's thesis presents two novel value pairs for the jet break frequency ν_b as a function of the X-ray power law photon index Γ for black hole systems.

Keywords X-ray binary, multiwavelength, multifrequency, accretion disk, astrophysical jet, disk–jet connection, X-ray astronomy, X-shooter

Aalto University
School of Electrical Engineering

Aalto-yliopisto, PL 11000, 00076 AALTO
www.aalto.fi
Diplomityön tiivistelmä

Tekijä Alexandros Binios

Työn nimi Moniaallonpituustutkimus kertymäkiekon ja astrofysikaalisen hiukkassuihkun välisestä yhteydestä matalamassaisissa röntgenkaksoistähdissä

Koulutusohjelma Elektroniikka ja nanotekniikka

Pääaine Avaruustiede- ja tekniikka **Pääaineen koodi** ELEC3039

Työn valvoja Prof. Anne Lähteenmäki

Työn ohjaaja Ph.D. Karri I. I. Koljonen

Päivämäärä 28.9.2020 **Sivumäärä** 110+13 **Kieli** Englanti

Tiivistelmä

Röntgenkaksoistähdet ovat erittäin voimakkaita kaksoistähtiä, joissa normaali tähti syöttää materiaa massavirran kautta kompaktiin kohteeseen, kuten esimerkiksi mustaan aukkoon, ja tämän prosessin seuraksena vapautuu suuria määriä energiaa koko sähkömagneettisen spektrin läpi. Samanaikaiset moniaallonpituustutkimukset mahdollistavat röntgenkaksoistähtien perustavanlaatuisten astrofysikaalisten ominaisuuksien ja prosessien tutkimisen. Tämän diplomityön päätavoitteena on toteuttaa moniaallonpituustutkimus matalamassaisista röntgenkaksoistähdistä keskittyen niiden kertymäkiekon ja hiukkassuihkujen väliseen yhteyteen, jotta niiden spektritilat voidaan määrittää eri havaintojaksojen aikana. Diplomityössä käytetään samanaikaista ja lähes samanaikaista moniaallonpituusdataa aina radioalueelta röntgenalueelle asti. Diplomityön pääinstrumenttina oli X-shooter-instrumentti, jonka havainnot muodostivat perustan muille havainnoille. Diplomityössä tutkitaan yhteensä neljää eri matalamassaista röntgenkaksoistähteä.

Diplomityön tuloksissa esitetään ennennäkemättömän laaja moniaallonpituustutkimus ja sen tulokset pääkohteesta MAXI J1820+070, jonka todetaan olleen kovassa röntgenspektritilassa huhtikuussa 2018, jonka jälkeen se oli siirtynyt pehmeään röntgenspektritilaan saman vuoden heinäkuussa, kunnes lopulta 2018 lokakuun alussa se oli päätynyt keskikovaan röntgenspektritilaan. Huhtikuun havaintojen aikana astrofysikaalisten suihkujen todettiin yltävän aina radioalueelta lähi-infrapunaalueelle. Heinäkuun havainnossa astrofysikaalisia hiukkassuihkuja ei havaittu, ja kertymäkiekko dominoi emissiollaan X-shooter-alueella. Lisäksi, tässä diplomityössä esitetään kaksi uutta arvoparia röntgenspektriin sovitetulle potenssilain eksponentille ν_b ja hiukkassuihkua mallintavan optisesti tiheän ja harvan synkrotronispektrin välisen leikkaustaajuuden Γ yhteydelle mustan aukon järjestelmille.

Avainsanat Röntgenkaksoistähti, moniaallonpituus, monitaajuus, kertymäkiekko, hiukkassuihku, kertymäkiekon ja hiukkassuihkun välinen yhteys, röntgentähtitiede, X-shooter

Preface

I want to thank Karri Koljonen for his superb guidance and willingness to share his time while he mentored me during my master's thesis. He has always been ready to help me and to answer my questions. I feel privileged to be his first thesis student. Thank you Karri for this opportunity and for your guidance.

I want to express my deepest gratitude for the mother of my three children, Ira Sgouros, who has constantly supported and helped me throughout my studies and my thesis work. I am also grateful to my parents, and especially to my late grandmother and grandfather who always took care of me when I was young, and constantly supported my thirst for information.

Finally, I would like to thank my whole family – Ira, Stavros, Stefanos, and Alexandra – for their patience during my thesis work.

Helsinki, Finland, Earth, the 28th of September, 2020.

Alexandros Binios

Esipuhe

Haluan kiittää Karri Koljosta hänen erinomaisesta tuestaan ja avustaan opettaessaan minua röntgenkaksoistähtien salaisuuksien selvittämisessä. Hän on ollut aina valmiina neuvomaan ja vastaamaan kysymyksiini. Kiitos sinulle Karri tästä mahdollisuudesta ja opastuksesta.

Suurin kiitokseni on lasteni äidille Ira Sgourokselle, joka on tukenut minua sekä opiskeluiden että diplomityön aikana päivittäin. Haluan myös kiittää vanhempiani, ja erityisesti isoäitiäni ja isoisääni, jotka pitivät minusta aina huolta lapsena ja olivat valmiita vastaamaan loputtomaan tiedonjanooni.

Lopuksi haluan myös kiittää koko perhettäni – Iraa, Stavrosta, Stefanosta sekä Alexandraa – heidän jaksamisestaan sinä aikana, kun olen tehnyt diplomityötäni.

Helsinki, Suomi, Maa, 28.9.2020.

Alexandros Binios

The sky calls to us. If we do not destroy ourselves,
we will one day venture to the stars.

–Carl Sagan

We are just a slightly advanced breed of monkeys
on a minor planet orbiting an average star, ...

–Stephen Hawking

The first principle is that you must not fool yourself
– and you are the easiest person to fool.

–Richard Feynman

There is nothing impossible to him who will try.

–Alexander the Great

Contents

Symbols and Abbreviations

Greek Symbols

α	Spectral index
γ	Lorentz factor
ε	Radiative efficiency
κ	Opacity
λ	Wavelength
μ_{e}	Average molecular mass per electron
ν	Frequency
ν_b	Jet break frequency
π	Mathematical constant
σ	Stefan–Boltzmann constant
σ_{T}	Thomson scattering cross-section for the electron
χ^2	Chi-squared statistic
Γ	Photon power law index

Latin Symbols

c	Speed of light in vacuum
h	Planck constant
$\hbar$	Reduced Planck constant
k	Boltzmann constant
m	Mass
m_0	Rest mass
m_e	Electron rest mass
m_H	Mass of the hydrogen atom
m_p	Proton rest mass
r	Accretion disk radius
r_ISCO	Innermost stable circular orbit radius
r_Ph	Photon sphere's radius
r_S	Schwarzschild radius
v	The relative velocity between inertial reference frames
$\mathbf{B}$	Magnetic field strength
$B_{\nu,T}$	Planck's law
F_Gra	Gravitational force
F_Rad	Radiation force
G	Gravitational constant
I_ν	Intensity
$\mathbf{J}$	Angular momentum
L	Luminosity
L_Edd	Eddington luminosity
M	Mass of an astronomical object
$\dot{M}$	Accretion rate
$M_\odot$	Solar mass
M_Ch	Chandrasekhar limit
$\dot{M}_\mathrm{Edd}$	Eddington accretion limit
Q	Electric charge
R	Radius
R_{in}	Inner radius of the accretion disk
R_{out}	Outer radius of the accretion disk
T	Temperature

Units

μm	micrometre
cm	centimetre
erg	erg
keV	kiloelectronvolt
kg	kilogram
km	kilometre
kpc	kiloparsec
m	metre
mJy	millijansky
nm	nanometre
pc	parsec
s	second
GHz	gigahertz
Hz	hertz
J	joule
MHz	megahertz
THz	terahertz
Å	ångström

Abbreviations

AGN	Active Galactic Nuclei
ALMA	Atacama Large Millimeter/Submillimeter Array
AMI	Arcminute Microkelvin Imager
AMI-LA	Arcminute Microkelvin Imager Large Array
AMI-SA	Arcminute Microkelvin Imager Small Array
APEX	Atacama Pathfinder Experiment
ASCII	American Standard Code for Information Interchange
BAT	Burst Alert Telescope
BH	Black Hole
BHXRB	Black Hole X-ray Binary
ESO	European Southern Observatory
FITS	Flexible Image Transport System
HEASARC	High Energy Astrophysics Science Archive Research Center
HID	Hardness–Intensity Diagram
HMXB	High-Mass X-ray Binary
HS	High/Soft State
IH	Intermediate-Hard State
IMXB	Intermediate-Mass X-ray Binary
IS	Intermediate-Soft State
ISCO	Innermost Stable Circular Orbit
ISIS	Interactive Spectral Interpretation System
ISM	Interstellar Medium
LH	Low/Hard State
LMXB	Low-Mass X-ray Binary
LOFAR	Low-Frequency Array
MATLAB	Matrix Laboratory
MAXI	*Monitor of All-sky X-ray Image*
MHD	Magnetohydrodynamic
MIR	Mid-Infrared
NIR	Near-Infrared (X-shooter wavelength range 1020–2480 nm)
NS	Neutron Star
NTE	Nordic Optical Telescope's Transient Explorer

PCA	Proportional Counter Array
PI	Principal Investigator
QO	Quiescent/Off State
R	R – Language and Environment for Statistical Computing
RATAN–600	Radio Astronomical Telescope Academy Nauk – 600
REFLEX	Recipe Flexible Execution Workbench
RLO	Roche-Lobe Overflow
RXTE	*Rossi X-ray Timing Explorer*
SMA	Submillimeter Array
SOXS	Son of X-shooter
SPL	Steep Power Law State
SWA	Stellar Wind Accretion
Swift	*Neil Gehrels Swift Observatory*
TD	Thermal Dominant State
UVB	Ultraviolet-Blue (X-shooter wavelength range 300–560 nm)
VH	Very High State
VIS	Visible (X-shooter wavelength range 560–1020 nm)
VISIR	VLT Spectrometer and Imager for the Mid-Infrared
VLA	Karl G. Jansky Very Large Array
VLT	Very Large Telescope
WD	White Dwarf
WSRT	Westerbork Synthesis Radio Telescope
XRB	X-ray Binary
XRT	X-ray Telescope

List of Figures

List of Tables

1. Introduction

As long as we can remember, our species and most likely even our closest archaic human ancestors before us, have gazed into the night sky wondering what secrets it beholds. Over four billion years of continuous evolution has provided us with spectacular eyesight at wavelengths that we understandably call visible light, but there is much to be learned beyond this fraction of the electromagnetic spectrum from the night sky itself. Our eyes are a limitation to see the other wavelengths, and additionally our planet's atmosphere is opaque for many of these wavelengths beyond our sight. The positive side of being on a planet with an opaque atmosphere is that it allowed the evolution of our species to reach an epoch where we can study the wonders of the Universe itself – and to perform studies we do not know of being performed anywhere else in the Cosmos presently. Over time we gradually mastered a variety of techniques that led to optical telescopes, and ultimately to a variety of instruments that allowed us to capture the night sky at wavelengths never seen before – both with ground-based and spaceborne telescopes. The first radio telescopes were utilised in the 1930s, followed by X-ray instruments a few decades later. With these decisive milestones, multiwavelength astronomy was ready to be carried out for the first time in humankind's history. X-ray astronomy is the logical continuity to expand the wavelengths in astronomical research, and its possibility has had a profound significance to X-ray astronomy, and for all fields of astronomy and astrophysics. X-ray astronomy has revealed the high-energy spectrum of the Cosmos to the human species, and continues to open new possibilities with the improvements in X-ray instrumentation.

This master's thesis focuses on multiwavelength studies of X-ray binaries (XRBs). XRBs are powerful double star systems that have evolved from ordinary binary stars through major stellar evolution events. XRBs consist of a normal, non-degenerate star feeding a compact object, either a stellar-mass black hole (BH) or a neutron star (NS). The study of XRBs is crucial to the understanding of the astrophysical jets, the accretion disk, and their interconnectedness along with the processes and mechanisms taking place near the BH that allow ultimately the channelling of energy to high-energy streams. Additionally, the detailed studies of XRBs provide information of the formation and evolution of compact binary stars, the processes involved in the mass-transfer phases, and complements our understanding of larger scale similar structures known as the active galactic nuclei (AGN). AGN are supermassive BHs that are accreting matter in the centres of galaxies. This master's thesis main focus is on low-mass X-ray binaries (LMXBs) which have a stellar-mass star as the compact object's companion, and hence much less massive than high-mass X-ray binaries (HMXBs) that have companion stars with masses more than ten solar masses ($M_{\odot}$).

The main selection criteria for the LMXB sources studied in this master's thesis was the availability of data from the Very Large Telescope's (VLT's) X-shooter instrument – the only instrument in the world capable of simultaneous broadband observations spanning from the near-infrared to the ultraviolet spectrum. The broadband spectrum is pivotal in the study of emission components from XRBs especially during outbursts since the X-shooter's wavelength range overlaps the region where the both optically thin jet emission and the optically thick emission from the accretion disk are seen. The multiwavelength observations allow us to determine the fundamental properties of the accretion disk and the astrophysical jets. The additional requirement for the source selection in this master's thesis was the availability of (quasi-)simultaneous X-ray and radio observations. Other data sets, such as observations at mid-infrared and submillimetre wavelengths were included when possible. The selected targets are the MAXI J1820+070, the MAXI J1659−152, the SWIFT J1753.5−0127, and the GRS 1915+105 – which are all BH candidate LMXBs.

1.1 Motivation

Even after several decades of research work, the formation of astrophysical jets and their connection to the accretion mechanisms are still poorly understood. Black hole X-ray binaries (BHXRBs) offer us the possibility of monitoring full-scale outburst episodes. XRBs radiate throughout the electromagnetic spectrum, and observations performed with instruments ranging from the ultraviolet to the near-infrared bands are capable of capturing the emission from both the accretion flow and the astrophysical jets. These observations are of paramount importance, and they can be used to determine the fundamental properties of the accretion disk and the astrophysical jets, e.g. which emission processes are taking place, what are the large-scale physical structures of the accretion disk, or what is the particle distribution, and height of the acceleration region in the astrophysical jets?

XRBs offer us the possibility to examine the astrophysical jet and accretion disk dependency, known as the disk–jet connection (also called disk–jet coupling) on human timescales, something that we cannot achieve with solely studying AGN. On the other hand, AGN provide us information which cannot be determined from XRBs due to their compactness, such as the imaging of the BH's event horizon. Now, assuming that the accretion process and the formation of astrophysical jets are the same for both XRBs and AGN, we can now study them with the same astrophysical concepts. Thus, we can use the results obtained from studying the fast-evolving XRBs to infer the properties of the AGN with the scaling of the BH mass. This is possible due to the accretion of matter enabling the astrophysical jets to be formed, and this dependency being linearly proportional to the BH's mass. This gives us an understanding of how BHs and their growth affect a galaxy's evolution.

In other words, XRBs offer us to examine the centuries of evolution in active galactic nuclei in a matter of hours to days, opposed to centuries or even millennia of AGN studies, while AGN bring us closer to the centre of the BH and its events, something we cannot observe with XRBs due to their compactness and the distances between us and the targets of interest. Thus, these observations of XRBs and AGN complement each other while ultimately allowing the detailed astrophysical modelling of the two simultaneously.

1.2 Research questions

Currently, despite decades of research, our current knowledge on BHXRBs and the disk–jet connection is still limited – especially, the formation of astrophysical jets and the conditions that gives rise to them and governs their behaviour. One of the yet unsolved questions related to BHXRBs is what astrophysical conditions are needed for the formation of the astrophysical jets, and how the inflowing accretion power is distributed? Is most of the energy being channelled to the astrophysical jets, or do the astrophysical jets and the accretion disk winds compete for the same mass-flow supply? And what are the overall physical properties and parameters of the astrophysical jets, e.g. their composition and magnetic fields?

In order to shine light on these mysteries and to provide answers to these fundamental questions, we need simultaneous multiwavelength observations of BHXRB outbursts – in order to monitor the wide-range changes throughout the electromagnetic spectrum during an outburst, and to be able to distinguish between different emission mechanisms taking place. With these observations we can study the disk–jet connection and its applications in detail, and additionally provide more information on whether it is possible to unify all the physics of astrophysical jets and outflows associated with compact objects from stellar-mass to supermassive BHs? Ultimately, this master's thesis provides answers for the following research questions:

- What are the fundamental properties and parameters of the astrophysical jets during the (quasi-)simultaneous multiwavelength observation periods?
- What are the best-fit model parameters for the concurrent broadband observation periods?
- What is the spectral energy distribution of the targets during their concurrent observation periods?
- What are the emission processes during the different multiwavelength observation periods?
- How have the targets evolved during different observation periods?

1.3 Thesis objectives and goals

The prime objective of this master's thesis was to study BHXRB targets which have been observed (quasi-)simultaneously with the Very Large Telescope's X-shooter instrument along with radio and X-ray observatories. These simultaneous observations enable us to conduct a multiwavelength spectral analysis for the qualified XRB targets at different periods in order to fit spectral models, and to determine the emission mechanisms taking place. This enable us to study these targets and their astrophysical properties, especially the disk–jet connection along with the X-ray spectral states. [1, 2, 3]

One of the main research interests of this thesis focuses on the jet break frequency (ν_b) and photon law index (Γ) connection in BHXRBs. The jet break frequency ν_b marks the location where the optically thick emission transitions to the optically thin emission in the astrophysical jet spectrum, and the jet break frequency ν_b is additionally the peak of the synchrotron emission. The jet break corresponds to the most compact region in the jet where the electrons are first accelerated, i.e. the first acceleration zone. This jet break frequency ν_b is usually found from the radio to the near-infrared regions. [4, 5]

The photon power law index Γ gives the high-energy power law of the hard X-ray spectra, and it is defined as $\Gamma = \alpha + 1$ where α is the spectral index. BHXRBs have a relation between the jet break frequency ν_b and the X-ray hardness, and this feature seems to be common for all BHXRBs. The jet break frequency ν_b shifts during state transitions, and additionally during a specific state, e.g. as a BHXRB is in a hard state, its jet break frequency can move to higher frequencies within the outburst. Furthermore, determining the jet break frequency ν_b gives additional information about the underlying processes taking place and evolving during an outburst event. [4, 5]

An empirical relation between the photon power law index Γ and the jet break frequency ν_b has been specifically investigated by Koljonen et al. [6] where they interpret is as a connection between the plasma conditions near the BH's event horizon and the outflow properties which can be seen in figure 1 on the next page.

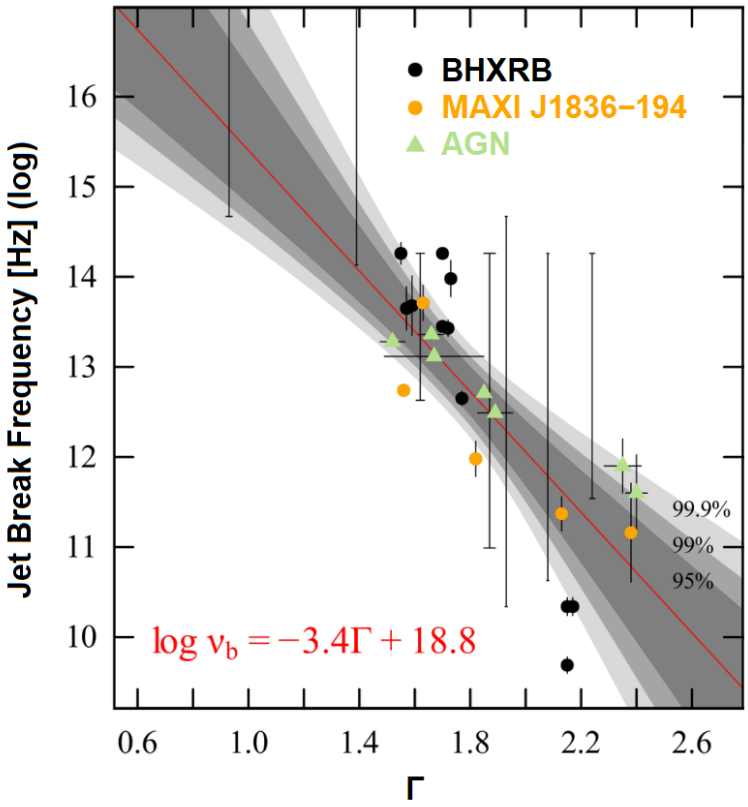

Figure 1: The jet break frequency (ν_b) as a function of the X-ray power law photon index (Γ) for BHXRB systems. Image credit Koljonen et al. [6] with slight modifications done by the master's thesis author.

One of the key discoveries of Koljonen et al. was that the power law photon index Γ correlates with the characteristic astrophysical jet spectrum's break frequency ν_b over a wide range systems and masses of BHs, thus showing that the correlation is not dependent on the mass or spin of the BH. This reveals that the fundamental properties governing the astrophysical jets are critically linked on the conditions of plasma near the BHs of all masses. Previously, only a few jet break frequencies ν_b had been identified due to the lack of simultaneous multiwavelength observations, especially in the mid-infrared and near-infrared regions, and because the accretion disk or the companion star was dominating the region around the jet break frequencies ν_b. Fortunately, we have more suitable instrumentation and faster response times dedicated to multiwavelength campaigns nowadays.

The VLT's X-shooter is an ideal instrument for these purposes, as it monitors the very region where multiple emission mechanisms take place, and thus allows to distinguish and constrain the accretion disk and astrophysical jet models, and to provide crucial information about the emission mechanisms taking place in the near-infrared to the ultraviolet regions, as there are many plausible contributing emission components and their combinations which include synchrotron radiation from the astrophysical jets, viscous and X-ray irradiated heating from the accretion disk, and synchrotron radiation from the hot inner accretion flow.

Koljonen et al. conclude that further research is needed to determine the nature of the jet break frequency and the spectral slope of the optically thin part of the jet spectrum, which can be achieved by detailed modelling of the spectral energy distributions of BHXRBs. This can be achieved with multiwavelength observations in the future, and a special point of interest is on BHXRBs which are in their low accretion phase, i.e. in the quiescent spectral state, as these observations would further extend the validity of the empirical correlation.

One of the main objectives of this master's thesis and its research is to provide valuable additions to the overall research results presented in Koljonen et al. [6]. This includes to investigate whether other BHXRB targets exhibit the jet break frequency ν_b versus the X-ray power photon law index Γ correlation. This can be only determined if the multiwavelength spectra of the targets are first modelled and fitted with appropriate spectral models. Thus, the main objectives and goals of this master's thesis can be listed as consisting of the following:

- **Objective:** Create a sample of BHXRB targets which have (quasi-) simultaneous data sets available from X-shooter along with the radio and X-ray observations.
- **Objective:** Perform spectral modelling for the different black hole X-ray binary targets with the available multiwavelength data sets.
- **Goal:** Model and determine the spectral models and X-ray spectral states the black hole X-ray binaries targets exhibit during their multiwavelength observation campaigns.
- **Goal:** Determine whether new values for the jet break frequency ν_b as a function of the X-ray power law photon index Γ can be obtained from the available black hole X-ray binary targets and their results.

1.4 Author's contributions

The author of this master's thesis started by searching and compiling a list of known XRB targets. After listing them, the author investigated which of these targets had observations done with the European Southern Observatory's (ESO) VLT, specifically with the VLT's multiwavelength X-shooter instrument comprising of near-infrared, visible and ultraviolet-blue bandwidths. Then the author listed all the XRB targets with X-shooter observations and began to search which of these targets had simultaneous and quasi-simultaneous data sets within $\pm$ 5 days available from all the other required wavelengths, i.e. radio and X-ray observations. This was done by conducting a literature research survey and additionally searching directly data sets from different observatory data archives such as the High Energy Astrophysics Science Archive Research Center (HEASARC) data archive [7]. This was the prerequisite for an XRB target being accepted as a potential source of investigation to this thesis, in essence satisfying the requirement of having simultaneous and quasi-simultaneous multiwavelength data sets comprising at least of X-shooter, radio and X-ray observations at a certain observation period.

The author found ultimately four targets that satisfied the selection criteria for further investigation. The author then acquired the X-shooter's raw data sets of the selected targets through the ESO's science archive facility with the exception of the MAXI J1820+070's raw data sets that were directly received from the principal investigator (PI) Koljonen. The author reduced the acquired X-shooter raw data sets with the dedicated ESO Recipe Flexible Execution Workbench (REFLEX) (hereafter EsoReflex) X-shooter pipeline, and performed telluric atmospheric corrections with the EsoReflex pipeline Molecfit. This was followed by screening and removing portions that were affected by the atmospheric absorption regions with Matrix Laboratory (MATLAB, hereafter Matlab), and then performed interstellar extinction corrections to the reduced data sets with R – the language and environment for statistical computing. After carefully performing the previous steps, the author next fitted astrophysical models to the different states of the selected four different targets at all available time periods with the Interactive Spectral Interpretation System (ISIS). The author was responsible for writing this master's thesis, and also made the schematics and drawings presented in this master's thesis.

1.5 Thesis structure

The structure of the thesis is divided into six chapters. The first chapter gives an introduction for this master's thesis followed by the motivation, the research questions, the objectives and goals of this thesis. The author's contributions and the master's thesis structure are presented as well. The second chapter of the thesis introduces the reader to general concepts and information regarding XRBs, specifically their classification, components, and the astrophysical processes related to XRBs and their astrophysical spectral states. The third chapter presents the selected XRB targets and their main known properties, gives an overview of the observatories used to obtain the necessary data sets for this thesis, and explains the used data analysis methods, programs and procedures in detail. The obtained results of all of the studied targets are presented in the fourth chapter. The fifth chapter provides discussion related to the obtained results. The final chapter of this master's thesis is the sixth chapter which concludes the thesis with a small summary of this master's thesis and its results. Acknowledgements, references and appendices are presented at the end of the master's thesis following the main chapters.

2. X-ray binaries

This chapter is the theoretical foundation of this master's thesis as it introduces the reader to the necessary astrophysical concepts, background data and theory, radiation mechanisms, and covers XRBs and their components in detail. XRBs are binary stars, which consist of a compact object and a normal star. The compact object, which is sometimes referred to as the compact star, is usually a NS or a stellar-mass BH. The compact objects are the accretors of the binary system. The accretor, as the name implies, is the companion which accumulates matter from the companion star known as the donor. The donor star is generally a normal main-sequence star, which feeds the accretor through mass-transfer. The matter flowing from the donor to the accretor forms an accretion disk around the compact object, and is ultimately the source which enables the formation of astrophysical jets. XRBs are usually discovered because of their intense X-ray brightness which is coming from immediate surroundings of the accretor such as the inner accretion disk. The donor star can be usually observed in other wavelengths, for example in the optical spectrum, and this together with observations from the accretor allow us to identify the fundamental properties of the binary system – such as the orbital period and the masses of the accretor and the donor star. [8] A typical LMXB is pictured in figure 2 where one can see the donor star's matter being transferred to the accretor, and thus enabling the formation of the accretion disk and the powerful astrophysical jets.

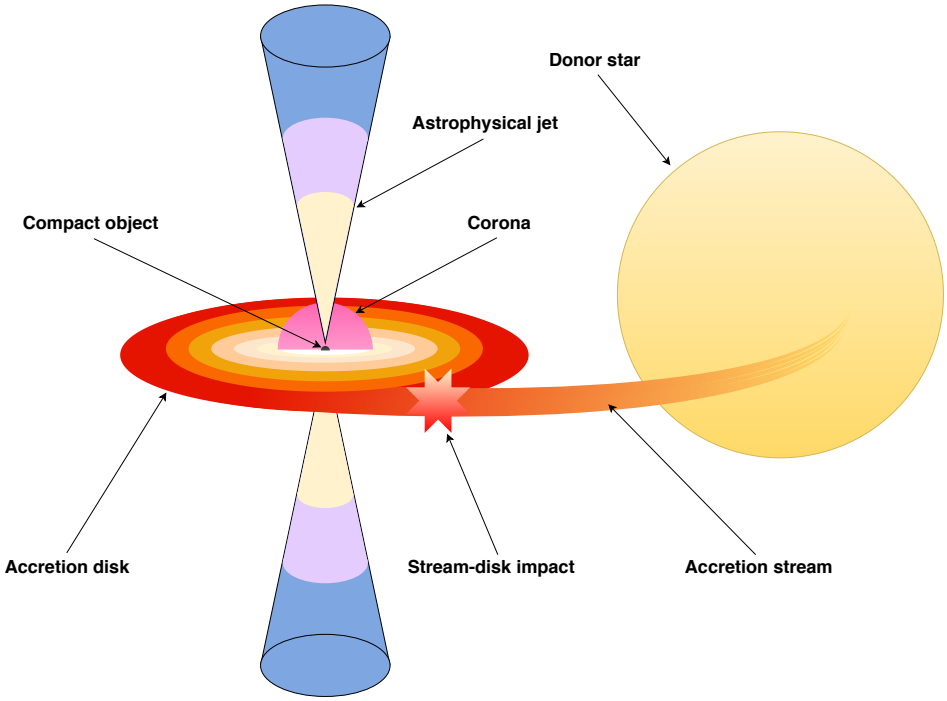

Figure 2: A schematic of an LMXB which is accumulating matter from the donor star to the accretor via the mass-transfer, and this enables the formation of an accretion disk around the accretor.

The first discovery of an XRB was done by the late Riccardo Giacconi – commonly referred as the father of X-ray astronomy – and his team in 1962 using an X-ray detector that was launched with an Aerobee 150 sounding rocket [9, 10, 11]. The target they discovered was Scorpius X-1, the first known X-ray source outside the Solar System. Today, we know that the brightest apparent source of X-rays in the sky after the Sun itself, is the Scorpius X-1 which is an LMXB situated roughly at a distance of 2800 pc [12]. Presently, there are hundreds of XRBs which have been discovered, with the latest catalogues from the years 2006 and 2007 listing properties of 187 known LMXBs [13] and 114 known HMXBs [14] respectively – now over a decade later it is safe to assume the number of discovered XRBs has already doubled.

Basic astrophysical concepts

In order to understand the massive amounts of energy released by the XRBs, one needs to understand the basic astrophysical mechanisms behind it. One of the key mechanisms is called accretion which is the term for matter falling onto some body. Accretion is a fundamental astrophysical process found in a variety of astronomical sources where the growth of a massive object is dependent on from matter in-flow by gravitationally attracting more matter from its surroundings – this is the case from protostars to ultimately AGN. Accretion itself is responsible for the structuring of the known Universe by allowing the formation of galaxies, stars, and planets themselves.

The main source of power in XRBs is the extraction of gravitational potential energy, and this occurs when matter is being extracted from the donor to the accretor, ultimately hitting the compact object – either its surface as is the case with NSs or the accretion disk itself. To have a basic understanding of the scale of energy released by these events, we can perform a simple calculation. Let's say the accretor is an NS which has a mass of $M = 1\ M_{\odot}$, and its radius is $R = 10$ km, thus the gravitational potential energy E_{Acc} released by the accretion of a mass $m = 1$ kg on to its surface is

$$\Delta E_{\mathrm{Acc}} = \frac{GmM}{R} \tag{1}$$

where G is the gravitational constant. Thus, the yield of energy E_{Acc} is roughly 10^{23} erg per accreted kilogram. [15, p. 1] In units more common to the everyday life, that is equal to 10^{16} J which is a tremendous amount of energy even when compared to a nuclear breeder reactor using uranium-235 as its fuel, since the nuclear reactor roughly produces 8×10^{13} joules per kilogram of uranium-235, thus 140 times less than per kilogram of accreted matter.

The reason for this example is to guide us through the following concepts that are needed in order to understand the principles of accretion in XRBs. Starting with the gravitational force F_{Gra} which is defined as

$$F_{\text{Gra}} = \frac{GmM}{R^2}. \tag{2}$$

The gravitational force works against the radiation force

$$F_{\text{Rad}} = \frac{L\kappa m}{4c\pi R^2} \tag{3}$$

where L is the total luminosity and κ is the opacity. Now, when balancing these two forces and specifying κ to be the ratio of the Thomson scattering cross-section for the electron σ_{T} and the proton's mass m_{p} we get the Eddington luminosity, also referred as the Eddington limit, which is the maximum luminosity an astronomical body can achieve in hydrostatic equilibrium. The Eddington luminosity L_{Edd} is defined as

$$L_{\text{Edd}} = \frac{4\pi GMm_{\text{p}}c}{\sigma_{\text{T}}}, \tag{4}$$

and when an astronomical body exceeds the Eddington luminosity, it will generate a powerful stellar wind which originates from its outer layers and expels matter. Now, we can derive the Eddington accretion limit $\dot{M}_{\text{Edd}}$ which gives the accretion rate $\dot{M}$ for a BH that radiates at the Eddington luminosity L_{Edd}, and this rate is

$$\dot{M}_{\text{Edd}} = \frac{4\pi GMm_{\text{p}}c}{\sigma_{\text{T}}\varepsilon c}, \tag{5}$$

where ε is the radiative efficiency which is defined as

$$\varepsilon = \frac{L}{\dot{M}c^2}. \tag{6}$$

[16, 17]

2.1 Compact objects

The densest known objects in the Universe are called compact objects or compact stars. They are characterised by their very high masses and low volumes. Compact objects are the endpoints of stellar evolution, and the type of the compact object is determined and limited by the mass of its original star type. These stellar endpoints include white dwarfs (WDs), NSs, and stellar-mass BHs. There are also hypothetical objects, such as quark stars, which have masses between NSs and stellar-mass BHs but these hypothetical midpoints have not been verified to exist yet even though there are a few objects that do not fit the NS range and are not BHs. Compact objects differ dramatically from ordinary stars, since they do not have nuclear fusion reactions in their cores as ordinary stars do. [18]

NSs are the evolution endpoints of stars which had a mass of 8–10 $M_\odot$ and above. NSs are formed when these massive stars collapse, and the electron degeneration pressure is not able to prevent the compact object from maintaining a stable WD [19, 20], and hence further gravitational collapse is inevitable to a more dense object. To our current understanding, NSs are the densest stars in the known Universe, if we exclude hypothetical star types which would be situated between NSs and stellar-mass BHs. NSs have a maximum mass of 2–3 $M_\odot$, and this limit is known as the Oppenheimer–Volkoff limit or as the Tolman–Oppenheimer–Volkoff limit, and NSs with a higher mass than 3 $M_\odot$ will collapse to a stellar-mass BH or to a hypothetical denser collapsed star core between a stellar-mass BH and a NS. NSs which are a part of XRB systems bring interesting additional features to the overall system, for instance NSs have a solid surface, something BHs do not, and when matter hits the surface with great velocity, powerful X-rays are produced. Additionally, NSs have powerful magnetic fields, which can prevent in certain cases the accumulation of matter close to the NS itself. [18, pp. 292–298] [21, 22]

Based on Einstein's general relativity, BHs are the ultimate endpoints of stellar life cycles. Only the most massive stars with masses M roughly beyond 40 $M_\odot$ have the inevitable fate of ending their life as a stellar-mass BH, since stars with less mass will end their lives as WDs or NSs. When a star is massive enough and cannot lose enough mass during its evolution, the force of gravity starts to dominate over all the other forces, for instance over the radiation pressure. This will result in the star collapsing to a stellar-mass BH as it has exceeded both the Chandrasekhar limit and the Tolman–Oppenheimer–Volkoff limit.

BHs are singularities without a surface and with gravitational fields so strong that after a certain region called the event horizon nothing can escape the grasp of the enormous gravitational field – not even electromagnetic radiation. BHs as a concept, were first theorised by John Michell and Pierre-Simon Laplace independently in the late 18th century as they considered the existence of non-luminous bodies that have such strong gravitational fields that even light cannot escape them [23]. In the early 20th century, Einstein published a number of publications of his theory of general relativity which also features the possibility of BHs. The Einstein field equations of the theory of general relativity are the fundamental key which relates the geometry space-time with matter, and additionally allows singularities, i.e. BHs, to exist. [24, 25]

The first solution to the Einstein field equations which describes a BH was discovered by Karl Schwarzschild in 1916, and hence is called the Schwarzschild metric [26]. It was also discovered independently nearly at the same time by Johannes Droste [27]. The Schwarzschild metric describes a static BH that has neither electric charge Q nor angular momentum $\mathbf{J}$. The discovery of a solution for a charged and non-rotating BH followed soon after the discovery of the Schwarzschild metric. The metric called Reissner–Nordström metric was discovered independently by Hans Reissner [28], Gunnar Nordström [29], Hermann Weyl [30], and George Barker Jeffery [31] between the years 1916 and 1921. The exact solution for an uncharged and rotating BH named the Kerr metric was discovered in 1963 by Roy Kerr [32]. This was quickly followed by the discovery of the exact solution for a charged and rotating BH in 1965 by Ezra Theodore Newman which was named the Kerr–Newman metric [33, 34].

The event horizon of a Schwarzschild BH is called the Schwarzschild radius r_{S}, and it is expressed as

$$r_{\mathrm{S}} = \frac{2Gm}{c^2} \tag{7}$$

where m is the mass. We can see that the Schwarzschild radius is proportional to the mass, and hence much more massive BHs have significantly larger Schwarzschild radii than stellar-mass BHs.

Outside the Schwarzschild radius is a region called the photon sphere which is the lower bound for any stable orbit, and as the name reveals, where photons travel in orbits due to the enormous gravitational pull from the BH. The photon sphere's radius r_{Ph} for a Schwarzschild BH is

$$r_{\mathrm{Ph}} = \frac{3r_{\mathrm{S}}}{2} \tag{8}$$

where r_{S} is the Schwarzschild radius. There are no circular orbits inside the photon sphere. BHs also have a region outside the event horizon called the ergosphere. The ergosphere, as the name suggests, is derived from words of Greek origin[1], and means a region where it is theoretically possible to extract energy and mass from rotating BHs. Ultimately, the extraction of angular momentum from rotating BHs leads to non-rotating Schwarzschild BHs.

BHs form accretion disks around them which are disk-like structures as matter falls into them while conserving the angular momentum of the matter. The accretion disks with other BHXRB key components along with their primary radiation mechanisms are explained in the Components and radiation mechanisms section. The accretion disks have a minimum orbit where a particle can maintain a stable circular orbit which is determined by general relativity. This orbit is called the innermost stable circular orbit (ISCO), and is an important factor in XRBs as it marks the inner edge of the accretion disk. In the case of Schwarzschild BHs, the ISCO is located at an radius r_{ISCO} of three r_{S} as we can see from the following expression

$$r_{\mathrm{ISCO}} = \frac{6Gm}{c^2}. \tag{9}$$

Fundamental concepts related to extracting energy from rotational BHs are the Penrose process, the Blandford–Znajek process, and the Blandford–Payne process, three mechanisms of great importance when considering the ultimate power sources of astrophysical jets, are explained in the Astrophysical jets subsection.

[1]Ergosphere is a combination of two words of Ancient Greek origin. The prefix "ergo-" itself comes from the word εργον (*ergon*) meaning "work" as we can see from the Proto-Hellenic origin of the word **wergon* (cognates of the word obviously include the Old English *weorc*). Sphere comes from the word σφαρα (*sfara*) meaning "sphere".

2.2 Classification and evolution of X-ray binaries

XRBs are classified into different categories depending on the mass of the donor star. These categories are usually divided into LMXBs, intermediate-mass X-ray binaries (IMXBs), and HMXBs. The common nomenclature refers to LMXBs as having a donor star with a mass $M \leq 1.0$–$1.2\ M_{\odot}$. The accretor of an LMXB can be a NS or a stellar-mass BH. In LMXBs the donor star is always less massive than the accretor. There are also several other more specific classification levels, such as microquasars, X-ray bursters, and soft X-ray transients. Microquasars are XRBs with powerful astrophysical jets which are often relativistic and appear to have superluminal motion. Often the groups also overlap with each other, for instance a target may be an LMXB, and additionally a microquasar at the same time. Today, we know that 90 % of the known XRBs can be classified into two distinctive main groups, the LMXBs and the HMXBs. These two groups are different due to a variety of physical characteristics, such as the mass of the donor star, the magnetic field strength, and orbital parameters. The remaining ten percent are classified into other groups, such as the IMXBs. [13, 35, 36]

The star types that are found with XRBs as being the donor star most frequently are briefly explained in this section. Donor stars in LMXBs include a wide range of star types ranging from the stars in the main-sequence to WDs, and these donor stars can be observed in the infrared and optical wavelengths [13]. The Sun and roughly 90 % of the stars in the Universe belong to a group known as the main-sequence stars which are stars that are fusing hydrogen into helium in their cores. Main-sequence stars have a variety of stars with different masses, ranging from the small M-type stars, commonly known as red dwarfs, to powerful O-type stars. The main-sequence stars eventually will start to have more of helium as they age, and this leads to the expansion of the stars – and results in subgiant stars or subgiants. They are smaller than giant stars, such as red giants, but significantly larger than their predecessors in the main-sequence. They are within the same mass range, since they do not lose mass that significantly.

The physical characteristics between LMXBs and HMXBs are quite different as they have a different matter flow process. The LMXBs have a mass-transfer process called the Roche lobe overflow (RLO), where the accretor's and donor's gravitational potentials are overlapping, and thus allowing the material to be accreted from the donor star to the accretor. HMXBs on the contrary have a mass-transfer process mainly dominated by stellar wind accretion (SWA) which is explained on page 37. In both cases, RLO and SWA, the matter flow allows the formation of an accretion disk around the compact object. [35]

The Roche lobe is defined as the region surrounding the binary star system where the material of the star is gravitationally bound to it. The Roche lobes of binary stars are dependent on the proximity of the stars in the system as this governs how they are affected [18, pp. 254–257].

In semi-detached binaries one of the stars fills its Roche lobe fully, and when the star exceed its Roche lobe, the hydrostatic equilibrium near the first Lagrangian point is no longer possible. This enables the RLO by allowing the outflow of matter from the exceeded Roche lobe to the companion star's own Roche lobe. Mass transfer by RLO also transports momentum to the accretor. Ultimately, the RLO is the mass-transfer mechanism which allows the mass accretion to the accretor from the donor star in LMXBs as shown in figure 3.

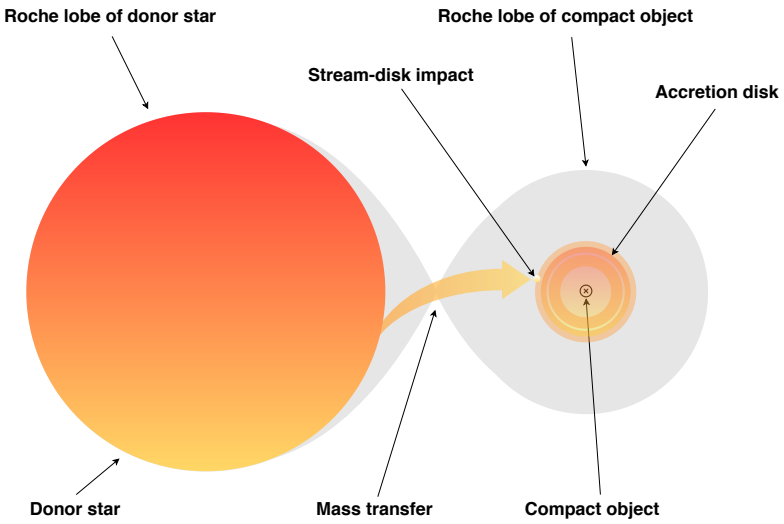

Figure 3: A schematic diagram of the donor star filling and exceeding its Roche lobe, and thus allowing the matter to be transferred to the accretor's Roche lobe.

HMXBs have a mass-transfer process mainly dominated by SWA, in which a small part of the powerful stellar wind coming from the donor star is being accreted onto the compact object, and thus fuels the accretor. All stars exhibit this phenomenon called stellar wind which varies with the star type. Stars which have been through their main-sequence and are in the (sub)giant phases are ejecting a lot more material through stellar wind than main-sequence stars. Their stellar wind is a flow of particles driven by the star's radiation pressure which is being ejected from the star's upper stellar atmosphere. The (sub)giant stars – that are the donor companions of HMXBs – are responsible for feeding the compact objects through SWA (seen in figure 4), and this enables the formation of accretion disks around the compact objects found in HMXBs. [18, 37]

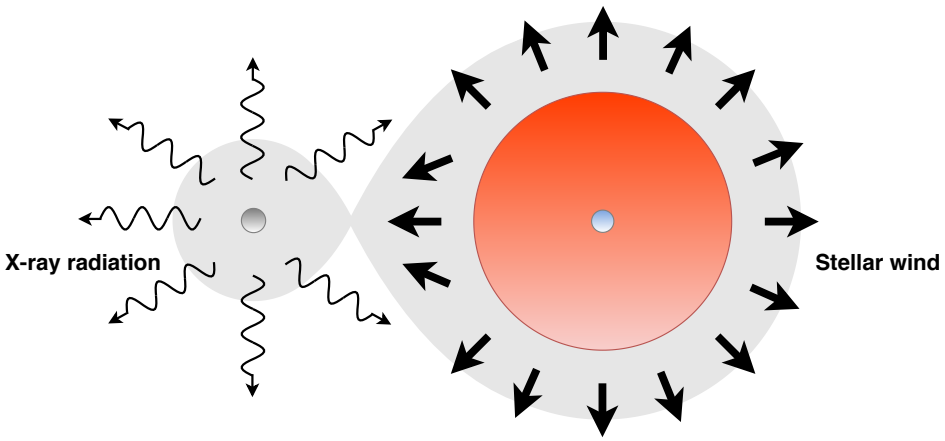

Figure 4: Schematic diagram of the donor star's stellar wind hitting the accretor, and thus allowing the matter to be transferred to the accretor. Thus, ultimately allowing the formation of accretion disk in the accretor. Note, how a portion of the stellar wind is focused and directed towards the accretor due to the gravitational forces in this schematic, although this is not always the case with HMXBs.

There are two main stellar evolution pathways leading to the two main XRB categories – LMXBs and HMXBs. The evolutionary case of LMXBs is shown in figure 5 on page 39, and the evolutionary pathway of HMXBs is shown in figure 6 on page 40.

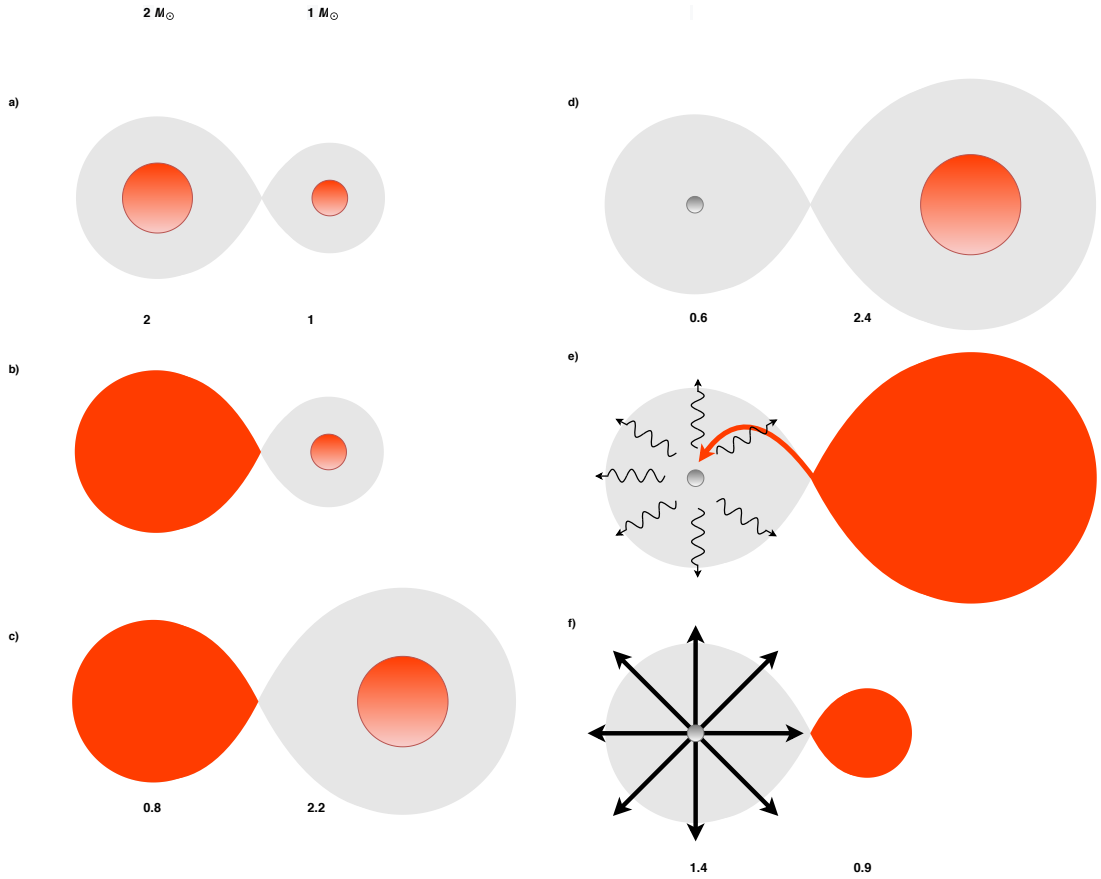

Figure 5: Schematic diagram depicting the evolution of an LMXB. **a)** First, the more massive star of the two main-sequence stars starts evolving independently. **b)** The more massive star continues to evolve, and starts to fill its Roche lobe, and finally fills and exceeds its Roche lobe completely – now, the evolution is no longer independent on either of the stars as the RLO has begun. **c)** The originally less massive star in the binary system has become considerably more massive than it originally was, and the originally more massive companion has evolved to a subgiant star. **d)** The subgiant star further evolves, and finally becomes a WD, while simultaneously the originally less massive star has become even more massive in terms of mass and size. **e)** The (sub-)giant star begins to transfer mass to the WD as it has exceeded its own Roche lobe which enables the WD to become a strong X-ray radiation source. **f)** Finally, the WD exceeds its Chandrasekhar limit and explodes as a supernova. [36] [18, p. 254]

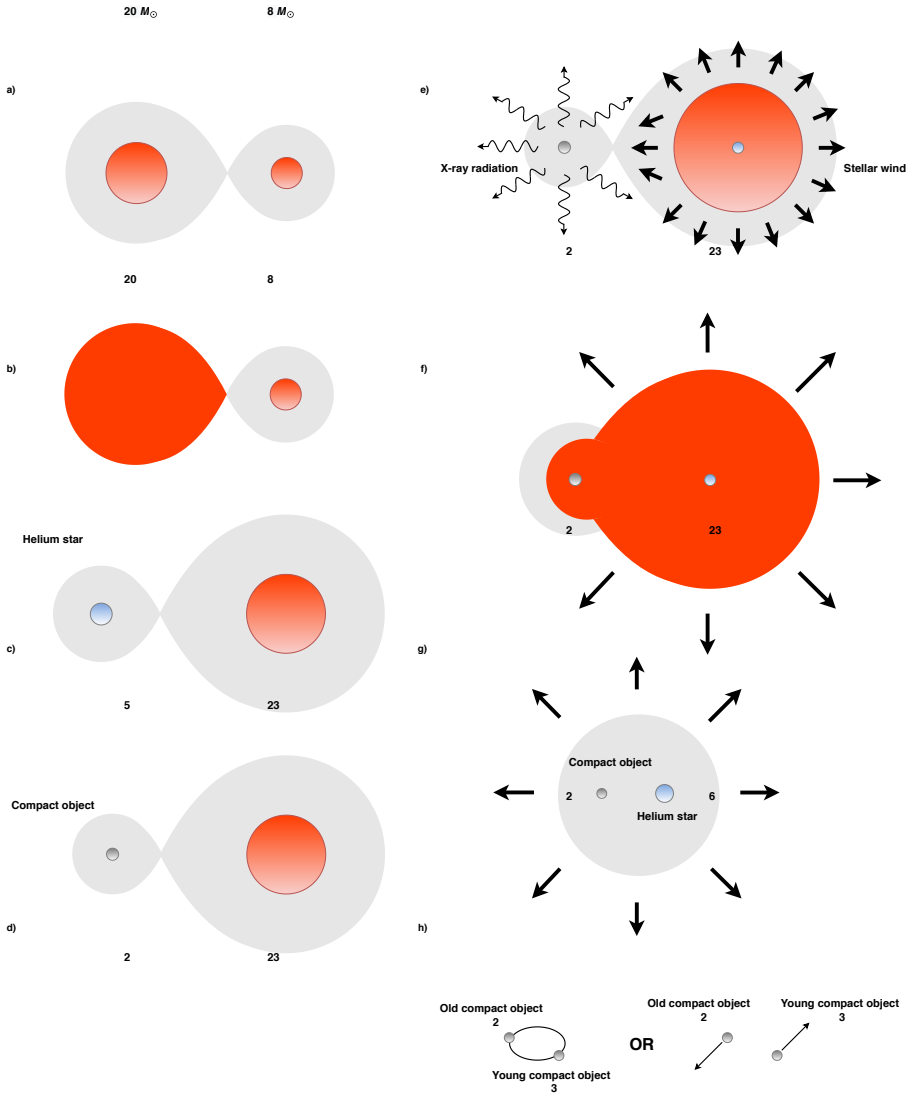

Figure 6: Schematic diagram depicting the evolution of an HMXB. **a)** First, two massive main-sequence stars form a detached binary system. **b)** The more massive star enters a new evolutionary phase after fusing all of its hydrogen, and starts to fills and exceeds its Roche lobe – the RLO to the smaller star has begun. **c)** The more massive star evolves, and it becomes a helium star, **d)** and finally explodes as a supernova which leaves behind a compact object, either a NS or a stellar-mass BH. **e)** The originally less massive star now enters the giant branch in its own evolutionary pathway, and as a result develops a powerful stellar wind which feeds the compact object, and as a result forms an accretion disk around the compact object – an HMXB is born with strong X-ray emission coming from the compact object and its surroundings. **f)** The giant star starts to be depleted from its mass, and has lost its outer layers, resulting in its helium core being exposed. **g)** The helium star will eventually explode as supernova which will leave behind another, younger compact object. **h)** Ultimately, the older and younger compact object will either continue their existence as a binary, or not if the supernova explosion is sufficiently strong enough to break their binary companionship. [18, 36]

2.3 Components and radiation mechanisms

The main XRB components in the system are the accretor with the donor, and the accretion disk, the corona, and the astrophysical jets. The donor star feeds the compact object, and forms an accretion disk around the compact object. The astrophysical jets are being formed from the accretion disk's matter being ejected from the central regions of the accretion disk where the corona is situated.

2.3.1 Accretion disk

The accreting matter from the donor star either through RLO or SWA (and in some cases from both) forms a disk of flattened matter around the compact object known as the accretion disk. Accretion disks are also found with many other astronomical objects, – ranging from young stellar objects with protoplanetary disks to active galactic nuclei. Due to angular momentum, an accretion disk starts to form as the matter cannot free fall directly to the compact object. Accretion disks are ultimately flattened disks of matter orbiting around the central mass, and releasing heat due to gravitational and viscous forces. The accretion disk heats up due to turbulent viscosity which is caused by the more rapidly spinning inner parts colliding with the slower moving outer parts. [38, 39, 40, 41, 42]

Accretion disks can be thin disks or thick disks. Thin accretion disks can be regarded as being two-dimensional which makes them considerably easier to be modelled than thick disks which need three dimensions. The accretion disk can be modelled using different radii to represent a multicolour accretion disk model where each radius represents a different black body with an individual temperature. The temperature of the accretion disk increases inwards until the ISCO is ultimately reached. [39, 40, 41, 42]

Thermal disk radiation

The accretion disk has the radiation spectrum of a multicolour black body. Black body radiation is the result of Planck's law where an ideal object called a black body absorbs and emits over all electromagnetic radiation frequencies. Planck's law is defined as

$$B_{(\nu,T)} = \frac{2h\nu^3}{c^2} \frac{1}{e^{\frac{h\nu}{kT}} - 1} \tag{10}$$

where h is the Planck constant, ν is the frequency, k is the Boltzmann constant, and T is the temperature[2]. [43, 44]

The temperature of the plasma in the accretion disk is dependent from the distance to the accretor. Thus, we need to model the accretion disk as a multicolour accretion disk that is optically thick and geometrically thin which sums up different ring-shaped regions having their own black body radiation profiles (figure 7).

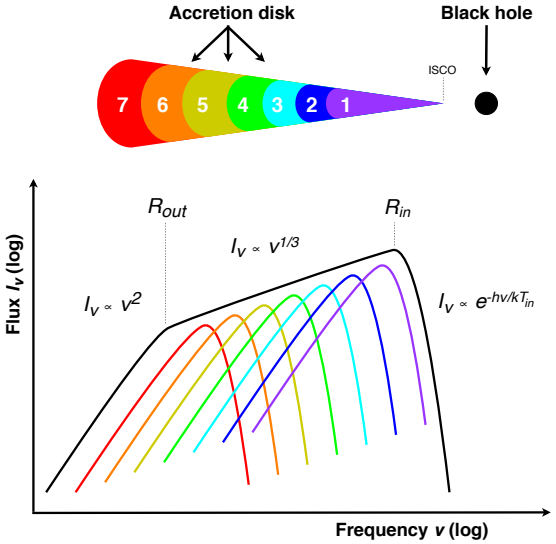

Figure 7: A schematic diagram of the spectrum from a classical multicolour accretion disk. The R_{in} represents the ISCO, and the R_{out} represents the outer radius of the accretion disk. The colours are numbered in the cross-section of the accretion disk above the diagram, and they represent the different ring-shaped regions that are summed up in the multicolour accretion disk model.

[2]This equation can be reduced to $B_{(\nu)} = \frac{\sigma}{\pi} T^4$ when we integrate over all frequencies, where σ is the Stefan–Boltzmann constant and π is the mathematical constant.

2.3.2 Astrophysical jets

Astrophysical jets or simply jets are powerful, high-energy streams of energy and matter – and quite often relativistic. The jets in XRBs are observed at radio frequencies and in other higher energy frequencies as well, ultimately spanning from radio to X-rays – and perhaps even to gamma-rays. Astrophysical jets are associated with AGN as well, and they both stem ultimately from accretion onto compact objects, i.e. the material forming the astrophysical jets comes from the accretion flow in both XRBs and AGN. Synchrotron radiation is the emission mechanism of the astrophysical jets. This can be seen with the spectra of radio jets which is non-thermal, and the brightness temperature is high while exhibiting linear polarisation in most cases. The synchrotron emission in the jet can also be self-absorbed. Flares are also frequently observed in the astronomical jets, and this is a clear indication of instabilities in the accretion disk itself. [45, pp. 1–21]

As the astrophysical jets are emerging from a region close to the compact object, it means that their velocities need to exceed the escape velocity of the region they are situated in. For example, the astrophysical jets observed from GRS 1915+105 have a velocity of $0.92c$, and its jets often show superluminal motion [46].

The astrophysical jets are produced extremely near to the compact object, and the powering mechanism or mechanisms to achieve relativistic velocities are still uncertain. The current hypotheses include extracting rotational and gravitational energy from the BH, and then ultimately allowing the formation of astrophysical jets through magnetohydrodynamical (MHD) processes, i.e. the magnetic properties and behaviour of electrically conducting fluids. The standard model of astrophysical jet formation is the Blandford–Znajek model, where the astrophysical jets in BH binaries are collimated disk winds that are launched, accelerated and collimated by the magnetic forces. The energy source for these astrophysical jets is the extraction of gravitational and rotational energy. In this model the magnetised and rotating inflow of matter in the accretion disk spirals towards the compact object, and thus twists the frozen magnetic field lines into a rotating helical coil. This results in some of the matter being expelled due to the magnetocentrifugal forces, and finally being lifted and collimated into the jet outflow because of the sheer magnetic pressure and compressing forces. A schematic diagram depicting the MHD acceleration and collimation model can be seen in figure 8 on the next page. [47]

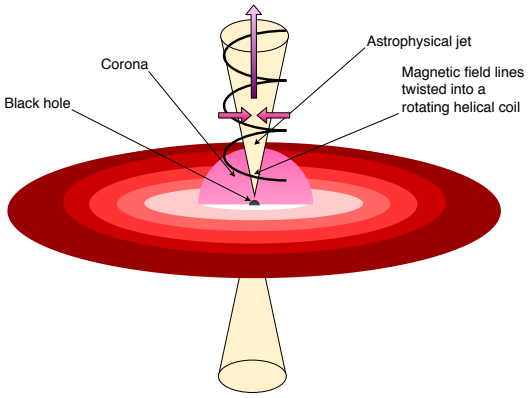

Figure 8: A schematic diagram depicting the MHD acceleration and collimation model.

Synchrotron radiation

Synchrotron radiation, also called magnetobremsstrahlung radiation, is an important radiation mechanism in astrophysics – especially with XRBs. In synchrotron radiation the charged particles are accelerated by powerful magnetic fields. As the charged particle, e.g. an electron or a positron, is accelerated by the high-power magnetic field, it emits electromagnetic radiation to the direction of its velocity vector. The emission pattern of the electromagnetic radiation is collimated forward in a narrow cone along the direction of motion of the charged particle, and the emitted synchrotron radiation is characterised by its non-thermal power-law spectra and polarisation. The non-relativistic form of synchrotron radiation is called cyclotron radiation where velocities of the charged particles are not approaching the speed of light c. [18, pp. 107–108, 332–335]

The powerful magnetic fields that are found with accretion disks are related to the very existence of the astrophysical jets, and additionally explain the high viscosity in accretion disks. BHs themselves cannot generate magnetic fields nor have magnetic poles, and thus the magnetic fields must be generated and found within the accretion disk and corona. The processes which are able to generate these magnetic fields are still not fully understood, and require more research. Ultimately, the disk wind of the accretion disk and the magnetic field lines through complex interactions near the corona must be responsible for the formation of the astrophysical jets through MHD processes capable of extracting the combination of rotational and magnetic energy, and these are discussed on the next page.

Penrose process

The Penrose process (also called the Penrose mechanism) was first described by Penrose and Floyd in 1971. The Penrose process demonstrates how rotational energy can be removed from rotating BH, if the rotating energy is located in the ergosphere and not inside the event horizon. Penrose and Floyd show how a particle with four-momentum can split into two particles near the BH. Then one of the particles crosses the event horizon, while the other one does not. The particle that is captured by the event horizon has negative mass-energy, and thus the escaping particle can have more mass-energy than in the beginning. This ultimately allows for the particle that escaped and which did not cross the event horizon to carry more mass-energy back than it had in the beginning. When this process cascades with a collision of multiple particles, the end-result particles will have the efficiency to escape the gravity well. [48]

Blandford–Znajek process

The Blandford–Znajek process (also called the Blandford–Znajek mechanism) was introduced by Blandford and Znajek in 1977 to describe a mechanism which can extract energy from a rotating BH. The process of extracting rotational energy from a BH has three main properties – angular momentum, a magnetic field, and the mass of the BH – and results in gravitational energy being transformed into Poynting flux. The Blandford–Znajek process demonstrates how energy and angular momentum are extracted from a BH which is threaded by magnetic field lines that are supported by external currents flowing in the accretion disk, i.e. a magnetised accretion disk. The magnetised accretion disk can have a large enough field strength which will prevent a stable cascade production of electron-positron pairs in the vacuum, and thus results in a force-free magnetosphere. The Blandford–Znajek process shows an efficient mechanism of extracting rotational energy from Kerr BHs that have accretion disks with a strong poloidal magnetic field around the spinning BH by the means of electromagnetic braking resulting from the magnetic fields supported by the external electric currents. It is noteworthy that charge doesn't affect significantly to the overall geometry of the rotating BH. [49]

An extension of the Blandford–Znajek mechanism by MacDonald and Thorne demonstrates that a great portion of the rotational and orbital energy of the accretion disk can be transferred through stationary and axisymmetric magnetosphere [50].

Blandford–Payne process

The Blandford–Payne process (also called the Blandford–Payne mechanism) describes the possibilities of extracting energy and angular momentum magnetically from accretion disks. This is possible by magnetic field lines which are originating from the accretion disk surface and that are extending to large distances from the surface. The Blandford–Payne process is defined by the equations of MHD, and assumes a Keplerian accretion disk which has infinite conductivity, and where the magnetic field strength $\mathbf{B}$ is proportional to the accretion disk radius r. The Blandford–Payne process demonstrates a mechanism where a centrifugally driven outflow of matter is possible from the accretion disk. This requires that the poloidal magnetic field component of the accretion disk makes an angle less than 60° with the surface of the accretion disk. The magnetic field's toroidal component collimates the outflow into two jets which are perpendicular to the accretion disk and that are anti-parallel. The flow is driven by gas pressure of the corona which is extremely hot and magnetically dominated. This ultimately results in matter being ejected as jets from the centre core and can be applied from stellar-mass BHs to supermassive BHs found in galactic nuclei. [51]

2.3.3 Corona

At the centre of an accretion disk is a region called the corona which is the source for the intense X-ray radiation found with XRBs. The corona consists of energetic electrons, often called hot electrons. The corona shows dynamical behaviour as it changes in size and brightness during different periods. Thus, in this thesis the corona is defined as the region where through inverse Compton scattering (often called inverse Comptonisation) of soft seed photons in the plasma cloud of hot electrons takes place. The soft seed photons themselves needed for the inverse Comptonisation are produced from the black body emission from the accretion disk and from the synchrotron emission. Some of the coronal emission, i.e. hard X-rays, is reflected from the accretion disk itself, and thus has a softer appearance to the observer. The corona is responsible for the power law component (hard X-rays) in the hard X-ray spectral states.

Compton scattering

Compton scattering along with inverse Compton scattering and Thomson scattering are one of the most important interactions between electromagnetic radiation and charged entities such as electrons and positrons – especially in astrophysics. In Compton scattering the wavelength of the electromagnetic radiation becomes longer as a photon loses part of its energy to the electron it is colliding. Thomson scattering is the low-energy limit of Compton scattering where the charged particle does not lose energy nor does the wavelength of the photon change. In inverse Compton radiation the effect is opposite than in Compton scattering, i.e. the electron gives part of its energy to the photon, and therefore the electromagnetic radiation becomes more energetic and its wavelength shortens.

Astrophysical applications where the electrons are often relativistic, results in high energy changes with the electromagnetic radiation, especially with large Lorentz factors γ, e.g. visible light becomes X-ray radiation. The Lorentz factor γ is defined as

$$\gamma = \frac{1}{\sqrt{1 - \frac{v^2}{c^2}}} \tag{11}$$

where v is the relative velocity between inertial reference frames.

2.4 Disk–jet connection and spectral states

The disk–jet connection, also referred to as the disk–jet coupling, is the study of the relation between the inflow and outflow of matter in XRBs and AGN. In other words, this defines the connection between the accretion disk to the astrophysical jet formation mechanisms, and how changes in the accretion disk configuration and mass accretion lead to different observed spectral states, and hence the occurrence and disappearance of astrophysical jets. The accretion rate with the accretion history define the spectral state. [45, 52, 53, 54]

XRBs exhibit different periods of X-ray activity ranging from a low luminosity state to a high luminosity state. These states were often referred as the high state, and the low state. What has to be remembered with this nomenclature, is that they were assigned in a time when only 1 to 10 keV X-ray band was predominantly used to study XRBs. This era was in the early 1970s when Tananbaum et al. showed two distinct spectral states that the Cygnus X−1 exhibited [55]. These observations showed clearly a high luminosity state without radio emission, and a low luminosity state with radio emission. The high luminosity state corresponded to a soft thermal X-ray spectrum, while the low luminosity corresponded to a hard non-thermal X-ray spectrum, and hence the names – high/soft (HS) and low/hard (LH) – were created to categorise these distinct spectral states. [54, p. 24] [55]

Observations that followed during the 1980s and 1990s revealed additional spectral states in BHXRBs as they seemed not only to transition between the two states but additionally through intermediate states. These states reveal us more about the different periods of accretion to the compact object, specifically the inflow and outflow of matter in the binary system. Long-term light curves give us the possibility to observe the outburst's length and brightness of individual sources, and reveal the spectral evolution during an outburst. When the spectrum is hard, it is dominated by a power law, i.e. non-thermal or thermal Comptonisation, while the soft spectrum is dominated by thermal emission coming from the accretion disk. A common behaviour with XRB outbursts is that they start with a hard spectra, then start transitioning to soft spectra, and then back to hard – but this is not always the case as there may be failed outbursts in which the source reaches the LH and then returns to a quiescence/off state (QO). [45, 52, 53, 54, 56, 57, 58]

Nowadays, when a greater proportion of the electromagnetic spectrum can be used to determine the spectral states of BHXRBs, we have been able to distinguish even more spectral states which describe the BHXRBs and their properties in even better fashion. The states which were conceived in the 1970s, the hard state and the soft state, can be referred as the canonical states, but a more defined range of states for the whole spectrum can be described as the following states given below, starting with the two main BHXRB spectral states, the LH and the HS. [54, pp. 10–12, 25] [57, 58]

Low/Hard state

The LH is a spectral state characterised by its very hard X-ray spectrum. The non-thermal (or thermal Comptonisation) component often dominates the spectrum, i.e. meaning that the corona dominates. This spectral state is characterised by high-energy X-rays which are produced in Compton scattering of soft photons by energetic electrons, especially in the corona and astrophysical jets, and having a strong disk reflection [18, p. 303]. The astrophysical jets emit mainly in the radio, and are characterised by being typically compact and optically thick. The X-ray spectrum can be fitted with a power law component, and with additional components such as the accretion disk (weak black body) amongst others. The photon law index Γ value is typically ~ 1.7 in the LH, and BHXRBs enter this spectral state at lower mass accretion rates. [45, pp. 15–17] [54, pp. 31–35]

High/Soft state

The HS, also referred as the Thermal Dominant state (TD), is dominated by thermal emission from the accretion disk, and can be fitted with a multicolour black body component, and either does not have a power law component or it is very weak, meaning that the spectral state has a weak corona, and a weak disk reflection. The photon law index Γ values are between 2.1–4.8 in the HS. The accretion rate is highest in this state. In the HS there is no radio emission, and so the astrophysical jets are likely suppressed, i.e. the HS never has a strong radio jet. The HS also exhibits a relatively strong gamma tail. [45, p. 16] [54, pp. 28–31]

Quiescent/Off state

The QO is a low-luminosity version of the LH, and has the presence of astrophysical jets. One of the arguments is whether the QO should be classified as an individual state or a low-luminosity version of the LH itself. This is because it is an extraordinarily faint state, and distinctly non-thermal and hard. A BHXRB reaches the QO at very low accretion rates, and this spectral state can be regarded as the starting point in the hardness–intensity diagram (HID) shown in figure 9 on page 51. BHXRBs spent most of their lives in the QO. The QO can be modelled with a single power law component along with an interstellar absorption component, and the QO has photon law index Γ values typically between 1.5–2.1. [54, pp. 26–26]

Intermediate spectral states

The intermediate BHXRB spectral states are non-canonical states, i.e. not belonging to the aforementioned X-ray spectral states, are situated between the main states, and hence called intermediate spectral states and can be regarded as transition states occurring between the main canonical states, and these include the very high state (VH) which is also referred as the steep power law state (SPL. Furthermore, other intermediate spectral states based on their hardness can be described as the intermediate-soft state (IS) and the intermediate-hard state (IH). The intermediate states exhibit emission from an optically thick accretion disk (the soft component) and from the hot plasma situated above or inside the optically thin disk (the hard component). In simpler terms, the accretion disk and the corona contribute roughly the same amount to the overall emission. [54, pp. 35–40]

2.4.1 Hardness–intensity diagram

The transitions a BHXRB typically goes through in an outburst can be illustrated with a HID (see figure 9) where the X-ray hardness ratio, i.e. hardness, is plotted against the X-ray bolometric intensity, i.e. intensity (both in logarithmic scale). The X-ray hardness ratio is the calculated normalised difference of two exposure corrected counts in two separate energy bands – the high energy and the low energy band. The typical spectral evolution for a BHXRB starts from the QO, and progresses to the LH. Then through a series of intermediate states, i.e. IH and IS, transitions to the HS, and then through intermediate states back to the LH, and finally descends to the QO or reactivates and starts to transition back to the other states as seen in figure 9. It is noteworthy that the outburst can be a failed outburst where the target reaches the LH but then transitions back to the QO possibly through the IH. [47]

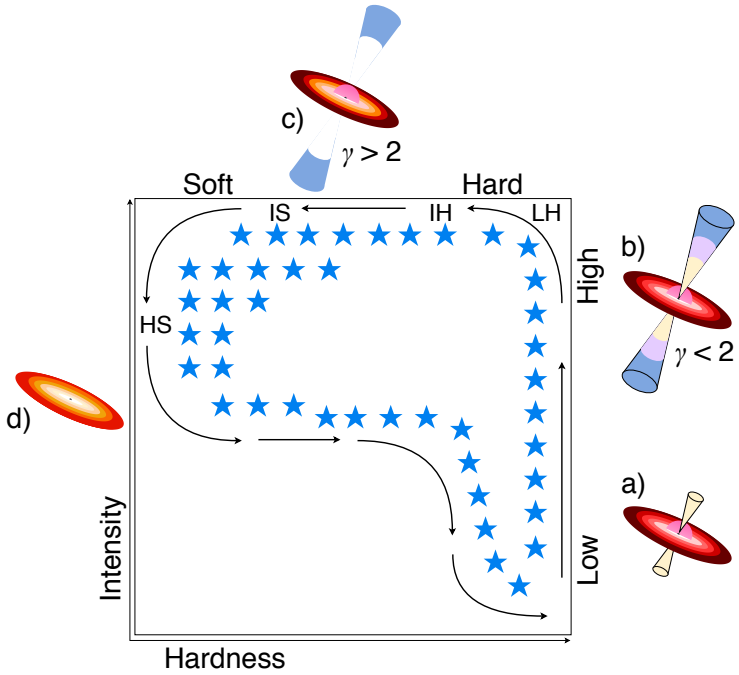

Figure 9: A highly simplified illustration of the "q-shaped" HID of a BHXRB. The LH, IH, IS, and HS correspond to low/hard, intermediate-hard, intermediate-soft and high/soft states, respectively. The blue stars mark approximate locations of different states, and the black arrows indicate the direction as the target evolves from **a)** the QO to **d)** the HS.

3. Observations and data reduction

In this chapter the selected XRB targets are introduced with their selection criteria, and basic astrophysical properties. The work was started by compiling a list of known LMXBs and HMXBs with X-shooter observations, which included the ones selected for the thesis and many others as well. Ultimately, there were four targets discovered that qualified the selection criteria of having (quasi-)simultaneous radio and X-ray observations within ± 5 days that complemented the X-shooter observations. The selected targets are MAXI J1820+070, MAXI J1659−152, SWIFT J1753.5−0127, and GRS 1915+105 – all of the targets are LMXBs that seem to have a stellar-mass BH as the accretor.

The instrumentation section is followed by the data reduction section which explains the data reduction procedures and shows the preliminary plots with raw, reduced, screened and corrected data sets. This section explains and covers the data acquirement methods with the raw data reduction processes and steps, including the correction procedures for telluric absorption and interstellar absorption corrections.

3.1 Selected targets

MAXI J1820+070

The MAXI J1820+070 (ASASSN−18ey) was discovered quite recently during an outburst, it was first discovered by the All-Sky Automated Survey for SuperNovae on the 6th of March 2018 as an optical transient [59], and then later on the 11th of March 2018 [60] discovered with the *Monitor of All-sky X-ray Image* (*MAXI*) instrument on-board the International Space Station [61, 62] as a bright X-ray transient. The target seems to be an LMXB [63]. The MAXI J1820+070 was the main target of this master's thesis as it had the most comprehensive quasi-simultaneous multiwavelength data available, and additionally it was the target of opportunity of the VLT proposal by Koljonen et al. [64] The target's compact object appears to have a mass ranging from 7–8 $M_\odot$ to 9.2 ± 1.3 $M_\odot$. The distance to the target is 2.96 ± 0.33 kpc, and it is one of the brightest X-ray transient sources ever observed. [65, 66, 67]

MAXI J1659−152

The MAXI J1659−152 was discovered on the 25th of September 2010 with the *MAXI* instrument after it first triggered the *Neil Gehrels Swift Observatory's* (*Swift's*) Burst Alert Telescope (BAT). The MAXI J1659−152's BH has a mass of 4–15 $M_\odot$. The donor star is an M-type star, commonly known as a red dwarf, with a mass of 0.15–0.25 $M_\odot$. It has an orbital period of 2.4 hours, which is currently one of the fastest rotational periods known of BHXRBs. [68, 69, 70, 71]

SWIFT J1753.5−0127

The SWIFT J1753.5−0127 was discovered on the 30th of June 2005 with the *Swift's* BAT. The compact object's mass is estimated to be 7.4 ± 1.2 $M_\odot$. The source has an orbital period of 3.2 hours, making it also one of the fastest rotational periods known of BHXRBs along with the MAXI J1659−152. [72, 73, 74]

GRS 1915+105

The GRS 1915+105 is a microquasar with superluminal astrophysical jets, and its accretor has a mass of 12 ± 2 $M_\odot$. The donor star is a K-type main-sequence star or an M-type star with a mass of 0.81 ± 0.53 $M_\odot$. [13, 46, 75, 76, 77, 78]

3.2 Observations with the Very Large Telescope

The VLT is the largest telescope in the Paranal Observatory, and it is operated by the ESO. The VLT is located in the Atacama Desert of northern Chile on Cerro Paranal at an altitude of 2635 m. The VLT itself is an array consisting of four individual telescopes, called unit telescopes. Each of the unit telescopes has a primary mirror of 8.2 m in diameter. The VLT covers the electromagnetic spectrum from ultraviolet wavelengths to mid-infrared wavelengths (λ), i.e. from 300 nm to 20000 nm. The VLT can accommodate a variety of different astronomical instruments, such as the X-shooter. Observations that were used in this master's thesis that came from the VLT were done with two astronomical instruments, the X-shooter, and the VLT spectrometer and imager for the mid-infrared (VISIR). The X-shooter being the main instrument, while the VISIR complemented the X-shooter observations by providing a single additional data set.

3.2.1 X-shooter

The X-shooter is a wideband intermediate resolution spectrograph, and was the first of the second generation instruments of the VLT. The X-shooter was the main instrument of this master's thesis as it is the only instrument in the world that can provide simultaneous broadband observations from the ultraviolet to near-infrared spectrum range. These broadband observations are crucial in order to be able to distinguish the variety of different emission components in BHXRBs. The X-shooter's broadband observations allow the precise identification of these emission components, something that cannot be done with only imaging observations of several wavebands. The X-shooter is a multiwavelength instrument, with its prism-cross-dispersed échelle spectroscopic arms operating in three wavelength regions – the Ultraviolet-Blue (UVB) (300–560 nm), the Visible (VIS) (550–1020 nm), and the Near-Infrared (NIR) (1020–2480 nm). The X-shooter itself consists of a total of four arms, where three of the arms are spectroscopic for the above mentioned wavelength regions, and the fourth arm is used for light imaging mode. The X-shooter operates at intermediate spectral resolution which is dependent on the wavelength being observed, and of the slit widths of the spectroscopic arms. [79]

X-shooter data sets

The X-shooter raw data sets (shown in table 1) were acquired via the ESO's science archive facility [80] with the exception of MAXI J1820+070's data sets, which were still under the proprietary period during the making of this thesis, and thus were acquired directly from the corresponding PI. These data sets can be currently acquired through the ESO's science archive facility with the programme identification code 0101.D-0356(A) [81].

Table 1: The X-shooter data sets used in this thesis.

Target	Observation Time
MAXI J1820+070	2018-04-12T07
	2018-07-13T02
	2018-07-14T03
	2018-07-15T04
	2018-09-30T00
	2018-09-30T01
	2018-10-01T01
MAXI J1659−152	2010-09-25T23
SWIFT J1753.5−0127	2014-08-16T23
	2014-08-17T01
GRS 1915+105	2010-09-19T00
	2010-09-24T23

3.2.2 VLT spectrometer and imager for the mid-infrared

The VISIR is a mid-infrared (MIR) instrument, and operates in three MIR atmospheric windows – M-band (5 μm), N-band (8–13 μm), and Q-band (17–20 μm). Acquiring simultaneous data sets with the X-shooter and VISIR is highly useful in multiwavelength observations of X-ray transients as it enables to have data points between the radio and near-infrared regions, and improves the best-fit spectral models. [82] The VISIR provided a single data set with four values (listed in appendix A) to the MAXI J1820+070's 2018-04-12 observations, and the VISIR observations were courtesy of D. Russell.

3.3 Radio observations

The radio data sets along with the millimetre and submillimetre data sets were acquired with several different radio observatories, and the usage of multiple radio observatories allows the coverage of a large portion of the radio spectrum, which is especially useful in multiwavelength observations of X-ray transients if the observations are simultaneous. The radio observatories with the data sets provided to this master's thesis are explained below along with their observations, and summarised at the end of this section in table 2 on page 60.

The Atacama Large Millimeter/Submillimeter Array

The Atacama Large Millimeter/Submillimeter Array (ALMA) observatory is located in the Atacama region in northern Chile, and has carried out observations since 1995. The ALMA is an interferometer consisting of 66 antennas altogether. Of these antennas, 54 are 12 m in diameter, and 12 are 7 m in diameter. The antennas can be moved to form various configurations, extending from a compact array configuration with a minimum baseline of 150 m to the most extended configuration with a maximum baseline of 16 km. There are currently eight different frequency bands which can be utilised. The frequency bands can be operated once at a time, and they currently extend from 84 GHz to roughly 950 GHz. [83]

The Atacama Pathfinder Experiment

The Atacama Pathfinder Experiment (APEX) is also a telescope located in the Atacama region, and it is a modified ALMA prototype of the 12 m antennas used in ALMA. The main difference to the ALMA interferometer is that the APEX telescope is a single dish that observes at millimetre and submillimetre wavelengths, i.e. in the region between the radio and infrared spectrum. The APEX operates in a variety of different frequencies, ranging from 0.2 THz to 1.5 THz. [84]

The Arcminute Microkelvin Imager

The Arcminute Microkelvin Imager (AMI) is part of the Mullard Radio Astronomy Observatory located in Cambridge, United Kingdom. The AMI itself consists of two separate arrays, the AMI Small Array (AMI-SA) and the AMI Large Array (AMI-LA). Both of the arrays are interferometric arrays. The AMI-SA consists of 10 antennas which all have a diameter of 3.7 meters, while the AMI-LA consists of 8 antennas which all have a diameter of 12.8 meters. The arrays are operating with a total of six frequency channels starting from 13.9 GHz and extending up to 18.2 GHz. [85]

The Karl G. Jansky Very Large Array

The Karl G. Jansky Very Large Array (VLA), also known by its previous name the Very Large Array, is located in New Mexico, United States of America. The VLA consists of 28 separate antennas with each having a diameter of 25 m, and of these antennas, 27 are active and one is used as a spare. The VLA is capable of observing targets from 1.0 GHz to 50 GHz with a resolution from 0.2 arcseconds to 0.04 arcseconds. All of the dish antennas are fitted with ten individual receivers, i.e. having the capability of observing ten different radio bands at the same time. [86, 87, 88, 89, 90]

The Low-Frequency Array

The Low-Frequency Array (LOFAR) is an interferometric array which consists of dipole antennas situated across Europe, and is capable of operating in two different frequency ranges, 30–80 MHz and 120–240 MHz. There are different baseline possibilities ranging from 100 m to 1500 km. [91]

The Radio Astronomical Telescope Academy Nauk – 600

The Radio Astronomical Telescope Academy Nauk – 600 (RATAN–600) is radio telescope located near the town of Zelenchukskaya in the Russian Federation. The RATAN–600 itself consists rectangular radio reflectors that have been placed in a circle with a 576 m diameter, and it operates in many different frequencies, ranging from 1.0 GHz to 22.2 GHz. [92]

The Submillimeter Array

Submillimeter Array (SMA) is radio interferometer located in Hawaii, a state of the United States of America located in the Pacific Ocean. The SMA consists of eight 6 m dishes which can be configured to have a maximum baseline of 509 m. The operating range of SMA is from 180 GHz to 420 GHz, and each of the individual dishes can observe two different radio frequencies at the same time. [93]

The Westerbork Synthesis Radio Telescope

The Westerbork Synthesis Radio Telescope (WSRT) consists of fourteen dishes each with a diameter of 25 m, and is located in Westerbork, the Netherlands. The WSRT is capable of performing observations in a frequency range from 0.1 GHz to 8.3 GHz. The WSRT has five antenna systems available which enable the observations of these different frequency regions. [94, 95]

Radio data sets

The used radio data sets (shown in table 2) in this master's thesis were obtained through literature and private communication through multiple scientists and researchers, and the radio data values are given in appendix A.

Table 2: The radio data sets used in this thesis with their basic information.

Target	**Observatory**	**Observation**	**Courtesy of**
MAXI J1820+070	ALMA	2018-04-12	A. Tetarenko
	SMA	2018-04-12	A. Tetarenko
	VLA	2018-04-12	A. Tetarenko
	LOFAR	2018-07-13 [96]	
	SMA	2018-09-29	A. Tetarenko
MAXI J1659−152	APEX	2010-09-25 [97]	
	WSRT	2010-09-26 [97]	
SWIFT J1753.5−0127	AMI-LA	2014-08-17 [98]	
GRS 1915+105	RATAN–600	2010-09-25	S. Trushkin

3.4 X-ray observations

The X-ray data sets were acquired with two space-based observatories, the *Swift* and the *Rossi X-ray Timing Explorer* (*RXTE*). Their basic instrument specifications and mission details along with the provided X-ray data sets are explained in the following subsections.

The *Neil Gehrels Swift Observatory*

The *Swift* is a multiwavelength observatory launched on November 20, 2004 to a circular low-Earth orbit with an altitude of 700 km. The *Swift* itself has three instruments on-board, the BAT, the X-ray Telescope (XRT), and the UV/Optical Telescope. The XRT operates in the energy range from 0.2 keV to 10 keV, and has a field of view of 23.6 $\times$ 23.6 arcminutes. [99, 100] The *Swift* provided most of the X-ray data sets used in this master's thesis, i.e. for all of the targets except for GRS 1915+105.

The *Rossi X-ray Timing Explorer*

The *RXTE* was an X-ray observatory, which was originally launched on December 30, 1995 into a low-Earth orbit, and seized operations on January 5, 2012. The *RXTE* had three instruments on-board, the Proportional Counter Array (PCA), the High Energy X-ray Timing Experiment, and the All Sky Monitor. The PCA operated in the energy range from 2 keV to 60 keV, and it consisted of five independent xenon-based proportional counter units. [101, 102, 103]

X-ray data sets

The X-ray data sets were first searched through HEASARC's Xamin [7] interface to match the X-shooter data sets' observation periods, after which they were downloaded and reduced by the master's thesis supervisor. The used X-ray data sets are shown in table 3 with their basic information.

Table 3: The used X-ray data sets with their basic information, such as the observation identification number, and the date of observation.

Target	**Instrument**	**Observation and Date**
MAXI J1820+070	*Swift*–XRT	00010627033 (2018-04-12)
		00010754003 (2018-07-13)
		00010754004 (2018-07-14)
		00088657008 (2018-07-15)
		00010627104 (2018-09-30)
		00010627105 (2018-10-01)
MAXI J1659−152	*Swift*–XRT	00434928000 (2010-09-25)
SWIFT J1753.5−0127	*Swift*–XRT	00033140032 (2014-08-16)
GRS 1915+105	*RXTE*–PCA	95701-01-38-00 (2010-09-21)
		95701-01-39-00 (2010-09-28)

3.5 Data reduction

The data reduction of the X-shooter data was performed with a variety of ESO dedicated pipelines, and different language and environment solutions. The author of this thesis performed the X-shooter raw data reduction, its telluric absorption correction, and screening.

3.5.1 Raw data reduction

The reduction from raw X-shooter data to readable numerical data has many steps. The first step after acquiring the raw data sets was to reduce them, and this was performed by using the dedicated X-shooter pipeline [104] – the X-shooter Workflow for Physical Mode Data Reduction (version 3.1.0) – which is an EsoReflex data reduction pipeline environment [105] for the VLT's raw X-shooter data products.

3.5.2 Telluric absorption correction

Ground-based astronomical observations suffer from telluric contamination which is caused by the Earth's atmosphere as it is filled with molecules that absorb and emit their own electromagnetic radiation. As photons arrive from vast distances, i.e. astronomical objects, they make their way through the Earth's atmosphere which then are observed with ground-based observatories along with the electromagnetic radiation caused by the absorption and emission of atmospheric molecules. Hence, the X-shooter data sets that were reduced needed to be corrected for telluric absorption contamination effects, particularly for heavily affected regions, i.e. the near-infrared and visible spectrum (see figure 10), as the ultraviolet portion does not suffer significantly from the telluric contamination. The telluric absorption corrections were performed with the X-shooter's dedicated telluric absorption correction tool Molecfit (version 1.5.1) for the NIR and VIS data sets by writing an individual driver for each data set in separate parameter file (an example is given in appendix B). [106, 107]

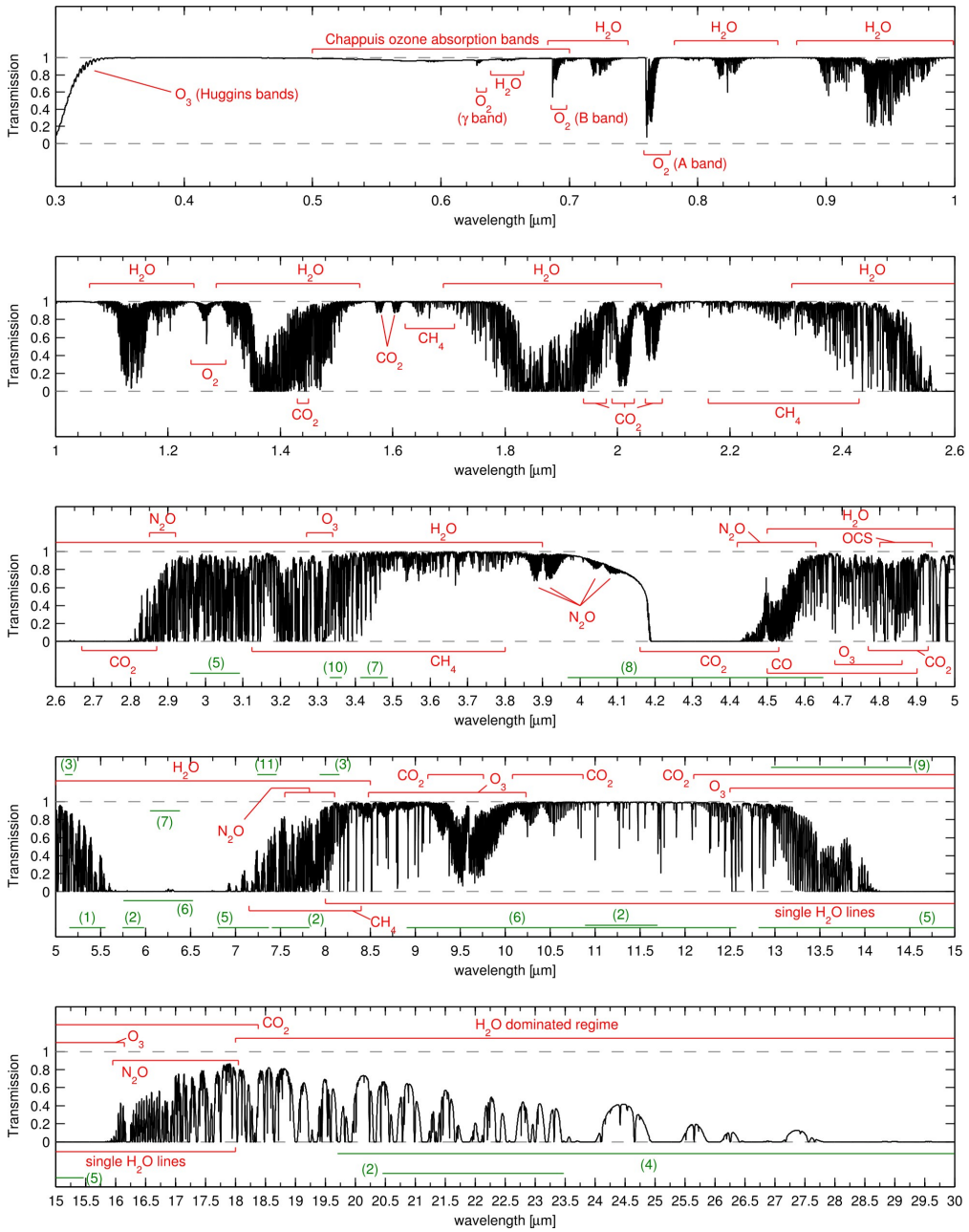

Figure 10: The X-shooter's wavelength regions which are affected by the telluric contamination caused by different molecules, for example water vapour and carbon dioxide [106].

3.5.3 Data screening

The next step was to transform the UVB portion's Flexible Image Transport System (FITS) files to readable American Standard Code for Information Interchange (ASCII) form files in order to combine them with the VIS and NIR portions, and to be able to screen them. This was executed with **fdump** which is part of FTOOLS [108] by HEASARC [109] given in appendix C.

The data sets were next screened for regions which are heavily affected by the Earth's atmospheric opacity, and for overlapping regions. The data sets were screened using Matlab [110]. As mentioned, there are certain regions which are well-known due to the molecules causing them, but there are additionally portions which can vary even daily due to atmospheric conditions, such as temperature. Hence, the data sets were screened for wavelength regions heavily affected which were shown in figure 10, and additionally checked and screened for daily conditions which might have affected the measurements, and visually for conflicting regions, i.e. clear disturbances in the observations. The main wavelengths that were included after screening all the X-shooter data sets, i.e. the UVB, VIS and NIR proportions, are shown in table 4. We can clearly see from table 4 that the data sets needed a considerable amount of screening before qualifying for scientific analysis, and some data sets even required full wavelength portions to be removed due to disturbances or bad quality, e.g. the GRS 1915+105 which had no usable data in the visible and ultraviolet range.

In figure 11 we see the MAXI J1820+070's VIS & NIR data set 2018-04-12T07 before screening, and can clearly distinguish the heavily affected regions such as 0.8–0.9 µm, 1.3–1.5 µm and 1.8–2.0 µm which had to be screened out. After screening the heavily affected regions, the data is ready to be further analysed. The next step was to convert the units to millijanskys (flux) and hertz (frequency). An example of the Matlab code written by the author which was used to screen the X-shooter data sets and to convert the units be found in appendix C.

Table 4: The main included wavelength ranges after screening the X-shooter data sets.

Wavelength region	λ [µm]
UVB	0.315–0.343
	0.347–0.370
	0.398–0.408
	0.412–0.434
	0.436–0.461
	0.473–0.484
	0.488–0.491
	0.507–0.538
VIS	0.555–0.586
	0.590–0.625
	0.638–0.650
	0.670–0.686
	0.694–0.704
	0.709–0.715
	0.730–0.755
	0.770–0.810
	0.961–1.000
NIR	1.018–1.070
	1.190–1.273
	1.520–1.730
	2.020–2.340

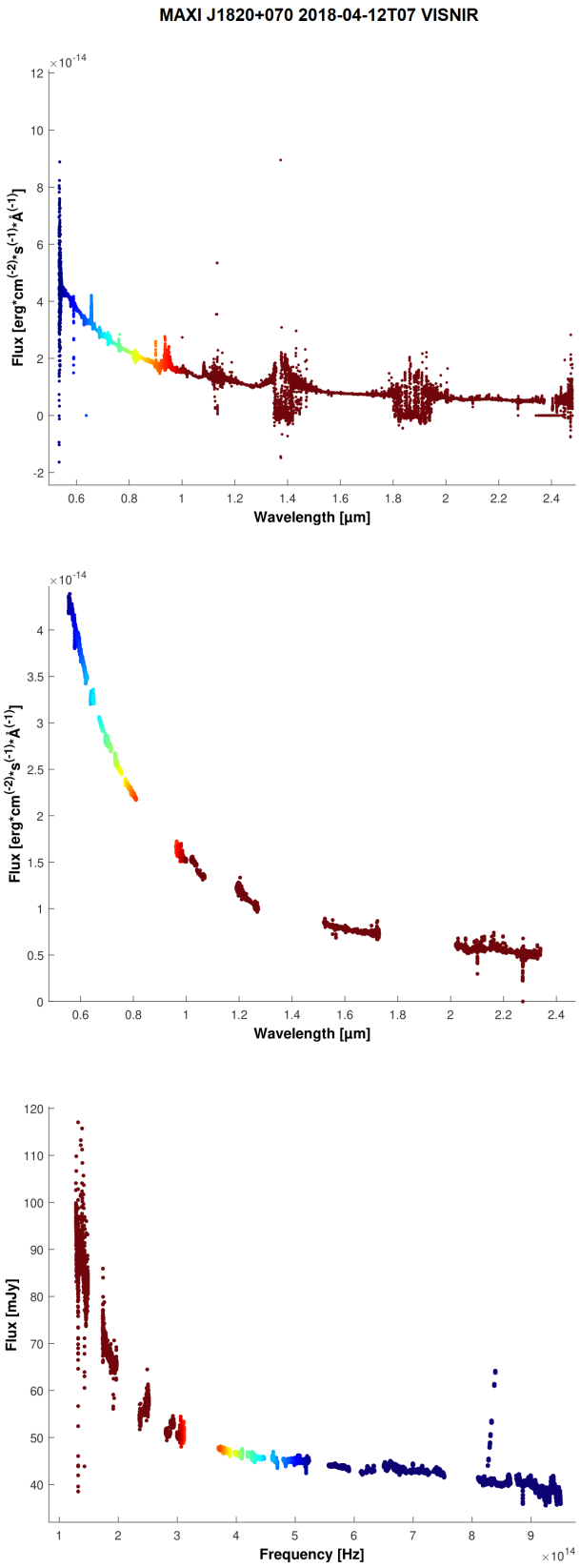

Figure 11: An example of the MAXI J1820+070's VIS & NIR data set 2018-04-12T07 before screening (top), after screening (middle), and finally with the UVB portion added, and the units converted to millijanskys (flux) and hertz (frequency) (bottom).

3.5.4 Interstellar extinction correction

Interstellar extinction, also known as interstellar reddening, is the absorption and scattering of electromagnetic radiation between the source that is emitting the electromagnetic radiation and the observer. The main cause of interstellar extinction is the interstellar medium (ISM), but additionally circumstellar dust, i.e. the dust around a star, can cause extinction as well. The ISM is strongly concentrated on the Galactic plane. The interstellar extinction increases at shorter wavelengths, for example on the visible spectrum blue wavelengths are a lot more affected by attenuation than red wavelengths, and hence results in the astronomical objects emitting light to appear redder than they truly are to the observer. This the reason interstellar extinction is sometimes referred to as interstellar reddening.

Ultimately, this means that the distant astronomical targets which are being observed for example with the X-shooter instrument, require to be corrected due to the interstellar extinction [111]. The R language and environment for statistical computing [112] was used to correct the effects of interstellar reddening of all the X-shooter data sets with the **fm_unred** script which is given in appendix C [113, 114].

As the targets are located at different distances and locations, the amount they needed to be corrected for interstellar extinction varied. This is due to the interstellar extinction being more pronounced on targets the further they are situated from us, i.e. the interstellar reddening increases as the distance increases. Thus, all the targets require a parameter known as $E(B-V)$ with individual values in order to be successfully corrected for their interstellar extinction. The $E(B-V)$ is calculated as $E(B-V) = (B-V) - (B-V)_0$ where $(B-V)$ is the measured colour index of the object, and $(B-V)_0$ is the true colour index of the object. The used $E(B-V)$ values in order to perform the interstellar extinction correction are given below in table 5 for each target.

Table 5: The $E(B-V)$ values of the selected targets.

Target	***E(B–V)***
MAXI J1820+070	0.163 [63]
MAXI J1659–152	0.34 [115]
SWIFT J1753.5–0127	0.45 [116]
GRS 1915+105	6.45 [46]

An example comparison of the same data set when corrected and uncorrected for the effects of interstellar reddening can be seen below in figure 12.

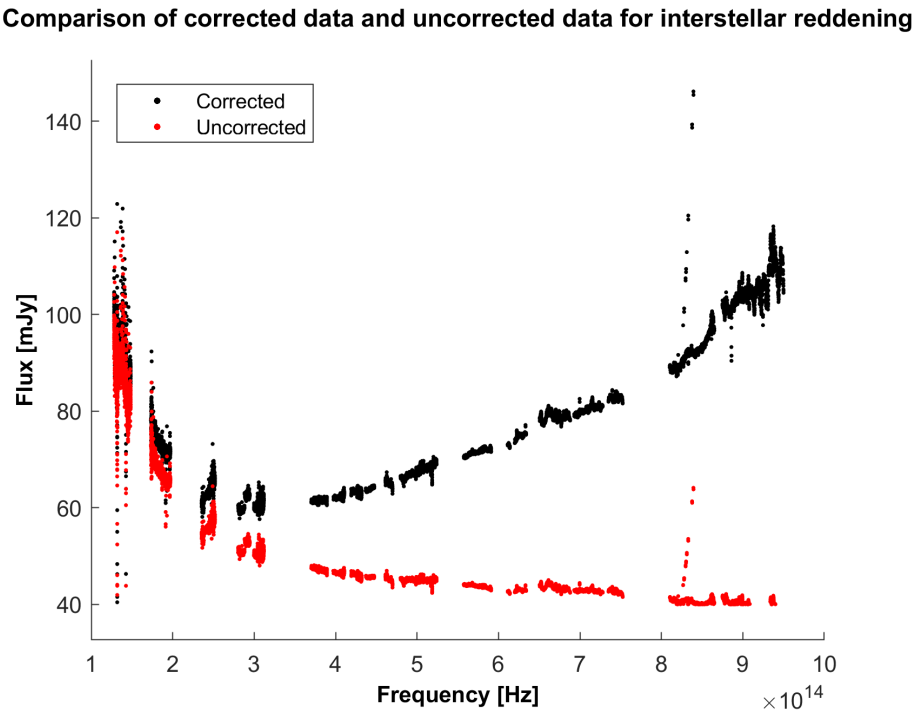

Figure 12: A comparison of the MAXI J1820+070's data set 2018-04-12T07 before and after correcting for the effects of interstellar reddening.

4. Data analysis and results

This chapter presents the results for all of the selected targets at their individual observation periods. This chapter also introduces the program called ISIS used for the spectral fitting procedures, and explains the spectral components used for modelling the observations of the targets. The chapter starts with the necessary background to the spectral fitting program ISIS, and then continues to the spectral model components used in the spectral fittings. Next, the fitting results from all of the targets are presented, and then the individual plots are shown – starting with the MAXI J1820+070. The results show how the target evolved during the observation periods. Next, the individual spectral fitting results for the other targets are presented.

4.1 Spectral fitting, components and models

ISIS is a software developed by the Massachusetts Institute of Technology Center for Space Research, and version 1.6.2-41 was used for the spectral fitting. ISIS was used for the multiwavelength analysis of data sets spanning from the X-ray spectrum to the radio frequencies. After the data reduction procedures from a raw data product to a usable data set, the X-shooter data sets were ready for further analysis and fitting of spectral models with their corresponding (quasi-)simultaneous X-ray and radio observations – and with the VISIR observations in a single case.

The necessary data sets were loaded through a script which was then ran through the terminal with the ISIS program. The data sets were grouped depending on the X-ray data instrument, for example the PCA data was grouped to a minimum signal-to-noise of 5.5 for all channels from 3.5 keV to 22 keV. Two examples of the used ISIS spectral modelling scripts, one for the *Swift*–XRT data sets and one for the *RXTE*–PCA data sets, can be found in appendix D.

The data sets were then modelled with a variety of different physically motivated spectral model components, until a best-fit spectral model was found. Finally, the determined best-fit models were optimised. The best-fit models with the parameters for all of the modelled observations can be found in appendix E. [117, 118, 119, 120, 121, 122, 123]

bbody

The **bbody** component gives a black body spectrum, as explained in the Thermal disk radiation part on page 44 [124].

bknpower

The **bknpower** component consists of two power law components with a break, and the break energy is given in keV. [124]

diskline

The **diskline** component gives the relativistic accretion disk line emission from an accretion disk. The characteristic disk line emission profile of iron is produced by X-irradiation of the cold gas in accretion disk due to relativistic Doppler effect and gravitational redshift, and is dependent on the inclination. [124, 129]

tbabs

The **tbabs** is a multiplicative model component for the interstellar medium grain absorption, and represents the Tuebingen–Boulder interstellar medium absorption model which calculates the cross section for the X-ray absorption by the interstellar medium. The **tbabs** is only for the X-ray data, and the X-shooter data has been corrected separately for the interstellar reddening. [124, 130]

diskir

The **diskir** is an irradiated disk model which consists of two standard components – the standard disk black body, and the Comptonisation of the accretion disk by energetic electrons. The accretion disk is the source for the seed photons needed for the Comptonisation, and this is how the accretion disk, and the energetic electrons are linked together. This means that as the disk temperature changes, it also affects the low-energy shape of the Comptonisation, but not vice versa in the model.

The thermal Comptonisation by the hot corona affects the seed photon spectrum. As the Comptonised component illuminates the disk, a small part of the illuminating spectrum produces the iron line and reflected continuum. The non-reflected fraction is reprocessed and re-emitted as quasi-thermal emission which contributes to the observed disk emission. The Compton tail can irradiate the inner accretion disk, and this can significantly alter the temperature structure of the inner accretion disk when compared to an unilluminated accretion disk. This is normally the case with BHs that are in the LH. The Compton tail is modelled with thermal Comptonisation, and the accretion disk with the standard **diskbb** [124, 125, 126] component.

The **diskir** model uses the **nthcomp** – thermally comptonized continuum – for the Comptonised emission. If there is no Comptonisation and the disk is not irradiated, i.e. $L_c/L_d = 0$ where L_c is the luminosity in the Comptonised emission, and L_d is the intrinsic energy disk luminosity, the **diskbb** and the **diskir** provide the same results. The L_c/L_d is given with the **diskir** parameter diskir(1).LcovrLd, and it gives directly the ratio of luminosity in the Compton tail to that of the unilluminated disk. Altogether, the **diskir** component has nine different parameters, including for example the normalisation parameter from which the apparent inner disk radius can be derived. The **diskir** is the main component that models the X-shooter frequency band, and this component can be used to model several different X-ray spectral states, e.g. the LH and the HS. [124, 127, 128]

4.2 Results

The targets and their observations with their best-fit spectral models are presented in this section. The best-fit models presented in this master's thesis for all of targets are summarised in table 6. The main parameters of all of the best-fit spectral models are given in table 7 on page 72.

Table 6: The summary of all the best-fit spectral models of all the modelled targets.

Target and its best-fit spectral model	**Observation**
MAXI J1820+070	
tbabs(1)∗(bknpower(1)+diskir(1)+diskline(1))	2018-04-12T07
tbabs(1)∗(diskir(1)+bbody(1))	2018-07-13T02
tbabs(1)∗(diskir(1)+bbody(1))	2018-07-14T03
tbabs(1)∗(diskir(1)+bbody(1))	2018-07-15T04
tbabs(1)∗(diskir(1)+bbody(1))	2018-09-30T00
tbabs(1)∗(diskir(1)+bbody(1))	2018-09-30T01
tbabs(1)∗(diskir(1)+bbody(1))	2018-10-01T01
MAXI J1659−152	
tbabs(1)∗(bknpower(1)+diskir(1)+diskline(1))	2010-09-25T23
SWIFT J1753.5−0127	
tbabs(1)∗diskir(1)	2014-08-16T23
tbabs(1)∗diskir(1)	2014-08-17T01
GRS 1915+105	
tbabs(1)∗diskir(1)	2010-09-19T00
tbabs(1)∗diskir(1)	2010-09-24T23

Table 7: The summary of the model parameters for all the sources. Here, the abbreviation red. is for reduced, and the diskir(1).kT_disk is represented by kT_d. The kT_d is in units of keV. Here, the * denotes that the parameter is fixed to a certain value.

Observation	Red. χ^2	Γ	kT_d
MAXI J1820+070			
2018-04-12T07	6.27	$1.56^{+0.22}_{-0.14}$	$0.34^{+0.02}_{-0.02}$
2018-07-13T02	2.10	$2.00^\star$	$0.776^{+0.005}_{-0.006}$
2018-07-14T03	1.20	$2.00^\star$	$0.78^{+0.01}_{-0.01}$
2018-07-15T04	0.85	$2.00^\star$	$0.79^{+0.02}_{-0.03}$
2018-09-30T00	0.96	$1.80^{+0.02}_{-0.03}$	$0.20^{+0.04}_{-0.02}$
2018-09-30T01	0.95	$1.80^{+0.02}_{-0.03}$	$0.20^{+0.03}_{-0.03}$
2018-10-01T01	0.90	$1.80^{+0.02}_{-0.04}$	$0.19^{+0.05}_{-0.05}$
MAXI J1659−152			
2010-09-25T23	1.67	$1.700^{+0.003}_{-0.004}$	$0.1309^{+0.0001}_{-0.0006}$
SWIFT J1753.5−0127			
2014-08-16T23	1.10	$1.75^{+0.04}_{-0.04}$	$0.062^{+0.009}_{-0.003}$
2014-08-17T01	1.08	$1.74^{+0.04}_{-0.04}$	$0.058^{+0.008}_{-0.003}$
GRS 1915+105			
2010-09-19T00	1.63	$1.54^{+0.10}_{-0.03}$	$0.47^{+0.03}_{-0.03}$
2010-09-24T23	0.98	$1.69^{+0.07}_{-0.04}$	$0.51^{+0.03}_{-0.05}$

The reduced χ^2 values of MAXI J1820+070's 2018-04-12T07 and 2018-07-13T02 best-fit models are quite high, and this is most likely due to the too small errors in the radio data, as the data had no systematic error.

One of the most interesting results was to be able to determine two new values for the jet break frequency ν_b versus the photon law index Γ for BHXRB systems. These values were added to the jet break frequency ν_b as a function of the photon power law index Γ figure, as shown in figure 13.

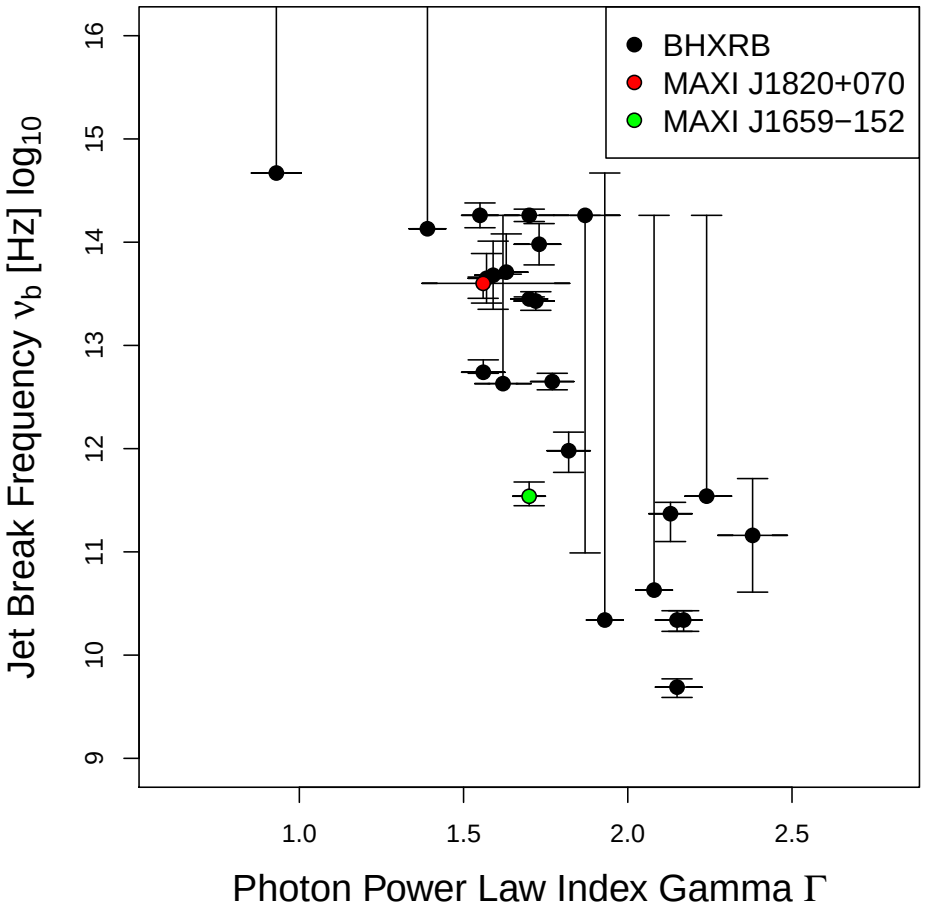

Figure 13: The jet break frequency ν_b as a function of the X-ray photon power law index Γ for BHXRB systems with the addition of the two new values with error bars from the optimised best-fit models of MAXI J1820+070 and MAXI J1659−152. There are two kinds of error bars presented in the plot, the long error bars where the data point is not in the centre are uniform, and the error bars with the data point in the centre are Gaussian.

The individual results that were obtained by fitting spectral models to the available multiwavelength observations are shown below. In the plots the parameter models are shown in red while the data points with error bars are shown in blue, and the residuals are shown below the main plot.

MAXI J1820+070

The best-fit model for the April observations is displayed in figure 14. The spectral model used for the April data set was **tbabs(1)*(bknpower(1)+diskir(1)+diskline(1))**. The obtained jet break frequency ν_b value was $1.65^{+0.25}_{-0.47} \times 10^{-4}$ keV ($\approx 3.99^{+0.57}_{-1.13} \times 10^{13}$ Hz), and the photon law index Γ value was $1.56^{+0.22}_{-0.14}$. The rest of the parameters are given in appendix E.

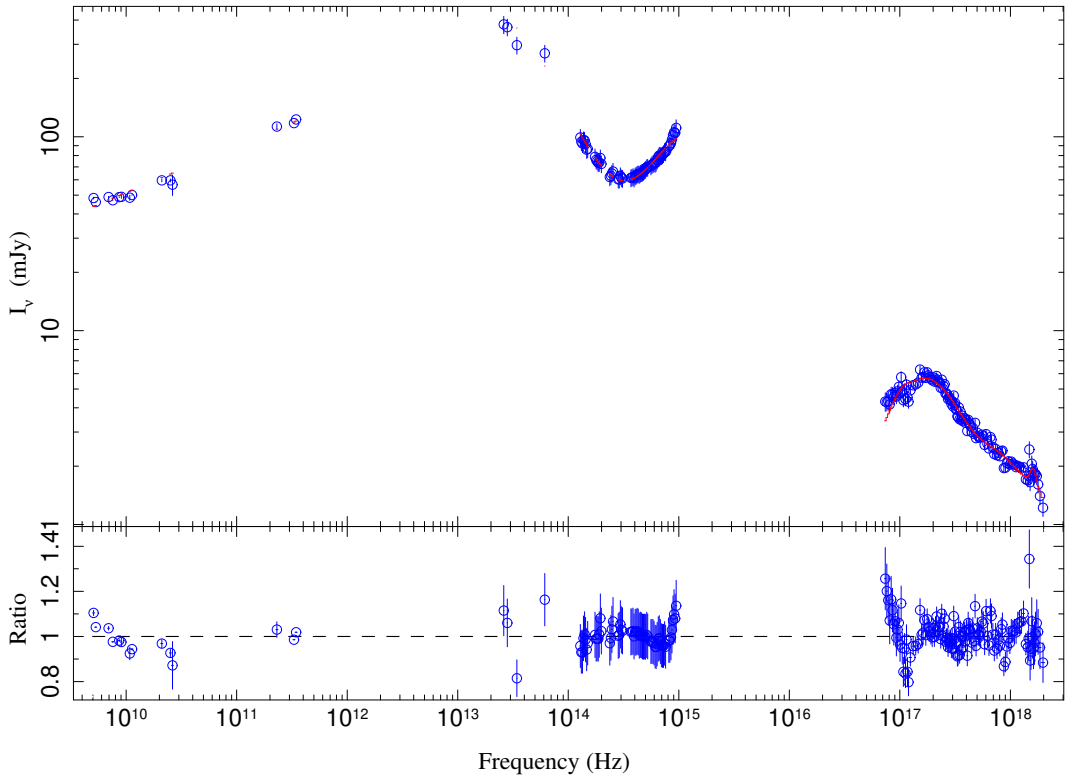

Figure 14: The MAXI J1820+070's 2018-04-12 multiwavelength observations with the best-fit model.

In figure 15 we can see the overall model shown in grey (with exaggerated width), the available data points in blue, and the spectral model components used for the April data set that were **tbabs(1)*(bknpower(1)+diskir(1)+diskline(1))**, shown in cyan, magenta, and gold, respectively. The components shown in the plot are unabsorbed.

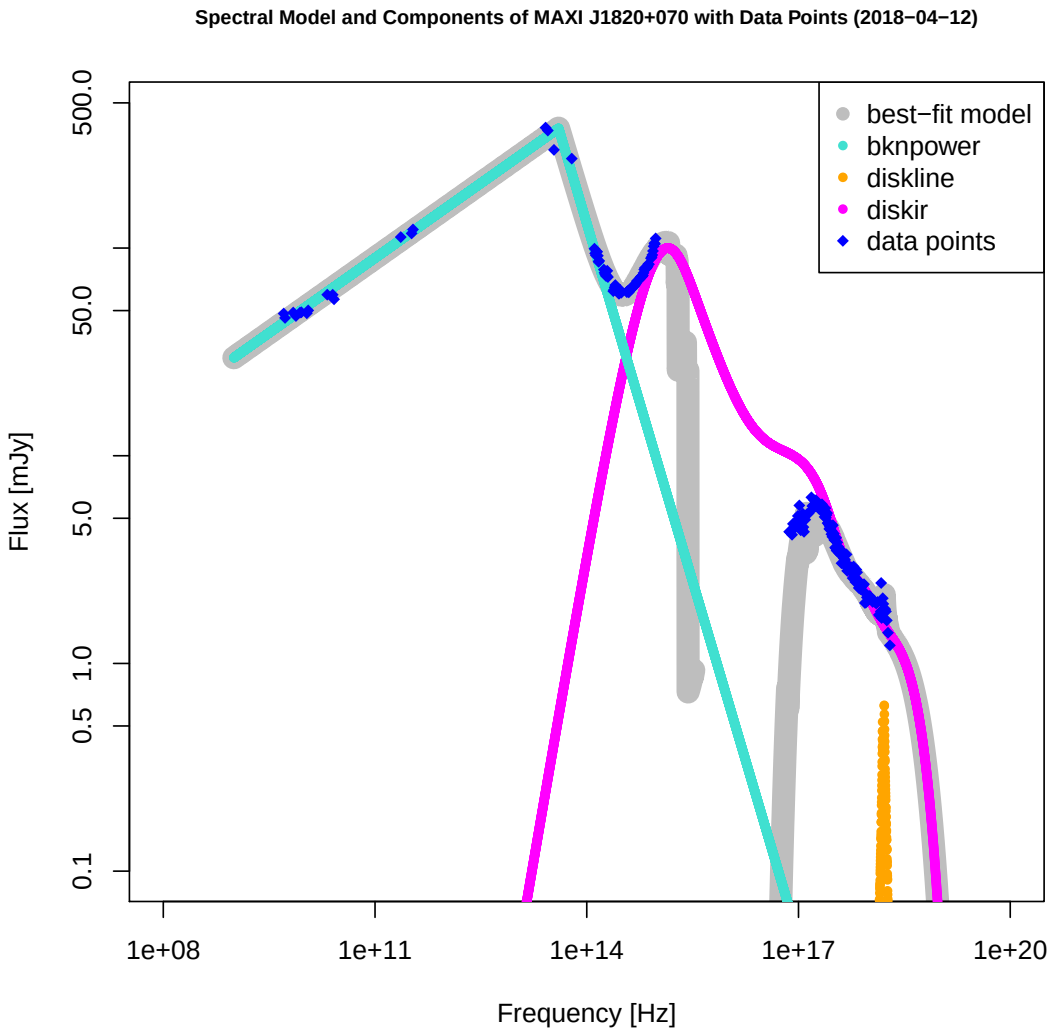

Figure 15: The MAXI J1820+070's 2018-04-12 multiwavelength observations with the spectral components, spectral model, and the data points.

In July 2018 the target clearly becomes less bright in the X-shooter band and radio regions, but has a strong increase of flux in the X-ray portion as seen in figure 16 which shows the all of the July observations in 2018 with the best-fit spectral model. The best-fit spectral model for all of the July observations was **tbabs(1)∗(diskir(1)+bbody(1))**. The spectral component **bknpower** which models the astrophysical jets was not used as there was only a single radio observation for the whole month.

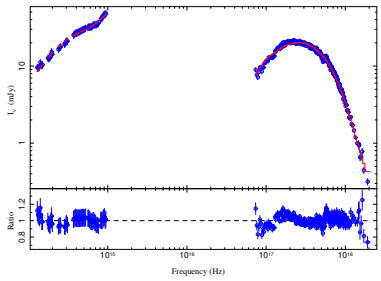

(a) 2018-07-13.

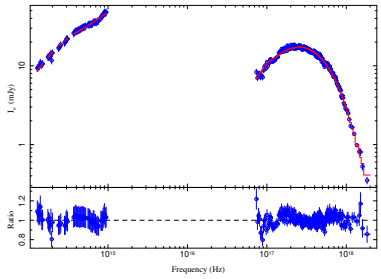

(b) 2018-07-14.

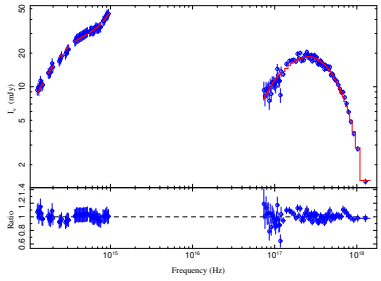

(c) 2018-07-15.

Figure 16: Comparison of the best-fit models for all of the July 2018 observations.

Here, we compare the best-fit models with and without the addition of the spectral component **bbody** to the July 2018 observations. The component **bbody** was used to correct mainly the UVB portion in order to obtain a better fit, and this can be clearly seen in figure 17. The usage of the **bbody** component (figure 17a) significantly improves the X-shooter band's model when compared to the model without the addition of the **bbody** (figure 17b). The best-fit model without the **bbody** was also tried after the UVB band was removed, i.e. after removing the region consisting of 7.0–9.3 $\times$ 10^{14} Hz, but this did not improve the best-fit model parameters nor the best-fit of the model **tbabs(1)∗diskir(1)** (given in appendix E). The usage of the **bbody** does not affect considerably the parameters of the **diskir** component, i.e. the main difference is to the fraction of bolometric flux which is thermalised in the outer disk.

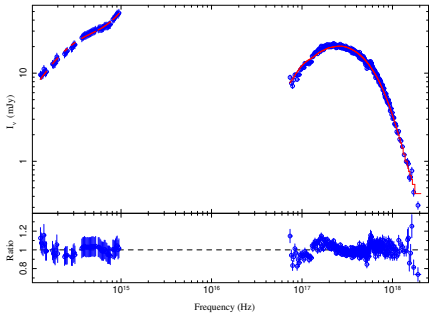

(a) **tbabs(1)∗(diskir(1)+bbody(1))**.

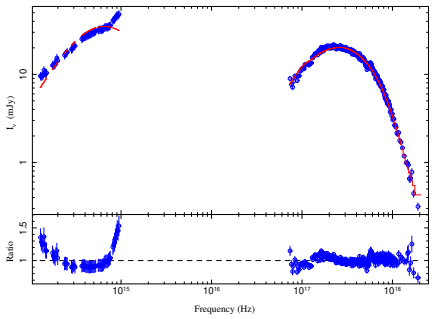

(b) **tbabs(1)∗diskir(1)**.

Figure 17: Comparison of the best-fit models for 2018-07-13 with and without the addition of the **bbody** component. Note how in (b) the model (in red) does not follow the data points (in blue) mainly in the X-shooter band's UVB region.

The spectral model used for all the July 2018 data sets was **tbabs(1)∗(diskir(1) +bbody(1))**, and the 2018-07-13 observation's spectral model can be seen plotted individually in figure 18. The component **bbody** is shown in black.

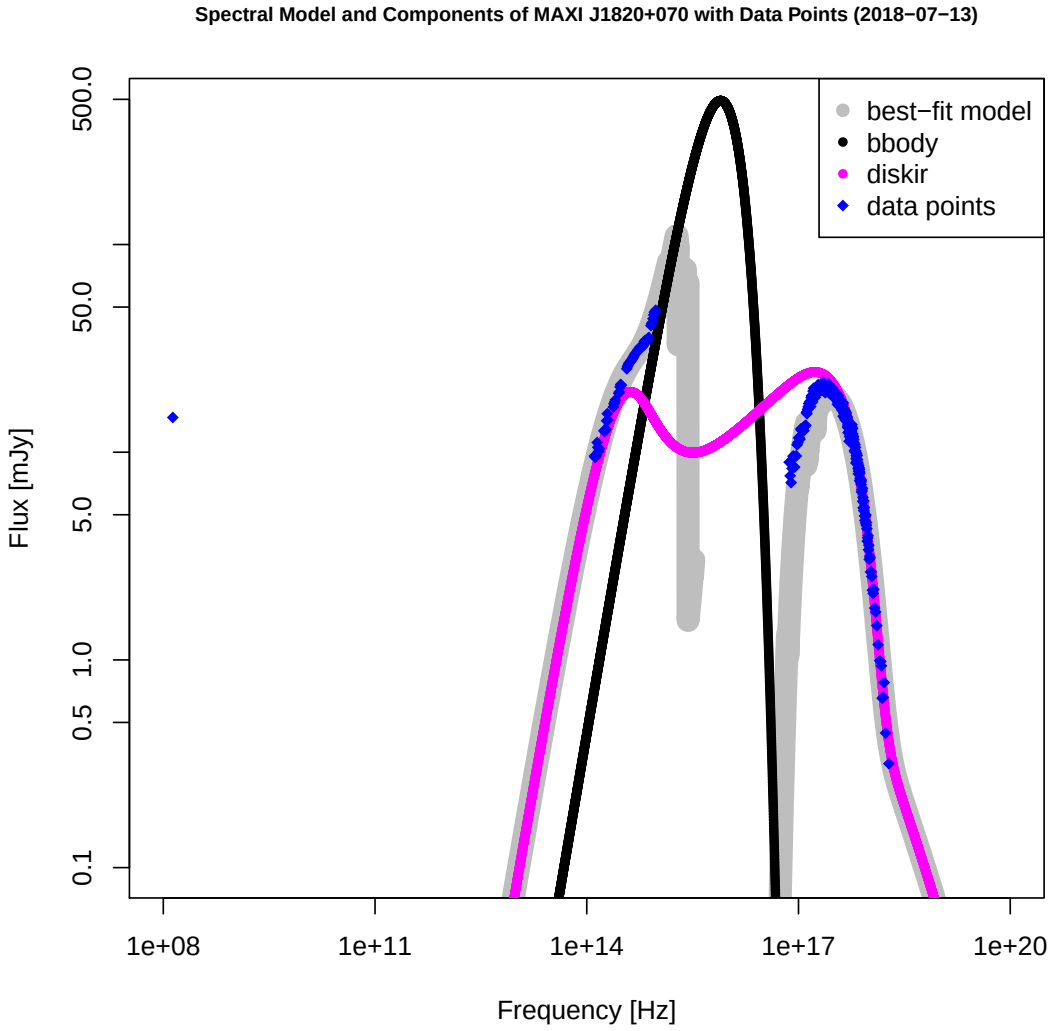

Figure 18: The MAXI J1820+070's 2018-07-13 multiwavelength observations with the spectral components, spectral model, and the data points. The component **bknpower** was not used in the best-fit since there was only a single radio observation available.

Finally, in September and October of 2018, the target has gone to an ever lower brightness state, but it has become harder in the X-ray spectrum. All of the September and October 2018 observations with the best-fit spectral model are presented in figure 19. The best-fit spectral model for all three observations in late September and early October 2018 was **tbabs(1)∗(diskir(1)+bbody(1))**. The usage of the component **bbody** was again due to correcting mainly the UVB portion in the X-shooter band, and thus resulting in a considerably improved best-fit model.

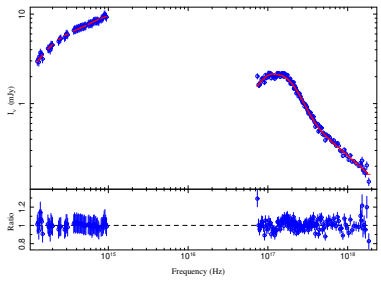

(a) 2018-09-30T00.

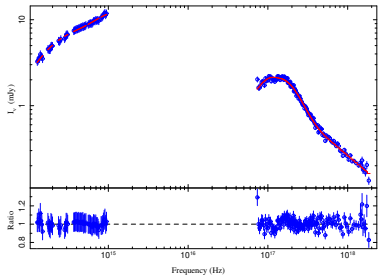

(b) 2018-09-30T01.

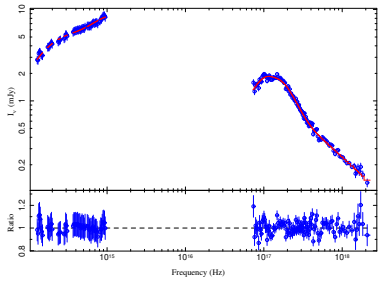

(c) 2018-10-01T01.

Figure 19: Comparison of the best-fit models for all of the late September and early October 2018 multiwavelength observations.

Here, we compare the best-fit models (figure 20) for the late September and the early October multiwavelength observations with and without the addition of the **bbody** component. As in the mid-July fittings, the addition of the **bbody** component significantly improves the overall best-fit, especially in the UVB region of the X-shooter band. However, this time the introduction of the **bbody** component to the best-fit changes significantly the **diskir** parameters, most notably to the electron temperature, the ratio of luminosity in the Compton tail to that of the unilluminated disk, and to the radius of the Compton illuminated disk in terms of the inner disk radius. The addition of the **bbody** component also affects the normalisation parameter. The best-fit parameters for both models, i.e. with and without the **bbody** introduced to the overall model, are given for comparison in appendix E. Additionally, the best-fit parameters are given for the best-fit model **tbabs(1)∗diskir(1)** without the UVB portion (7.0–9.3 $\times 10^{14}$ Hz) of the X-shooter band.

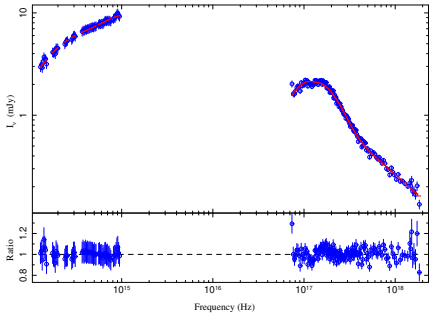

(a) **tbabs(1)∗(diskir(1)+bbody(1))**.

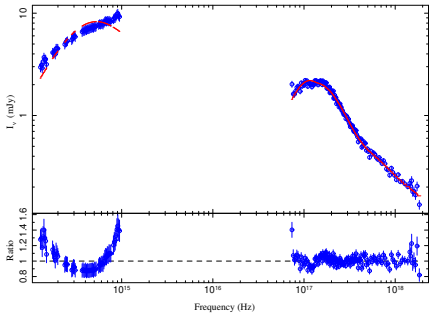

(b) **tbabs(1)∗diskir(1)**.

Figure 20: Comparison of the best-fit models for 2018-09-30 with and without the usage of the **bbody** component. Note again how in (b) the model (in red) does not follow the data points (in blue) mainly in the UVB region of the X-shooter band.

The spectral model used for the September and October data sets was **tbabs(1)*** (**diskir(1)+bbody(1)**), and an example can be seen plotted individually in figure 21.

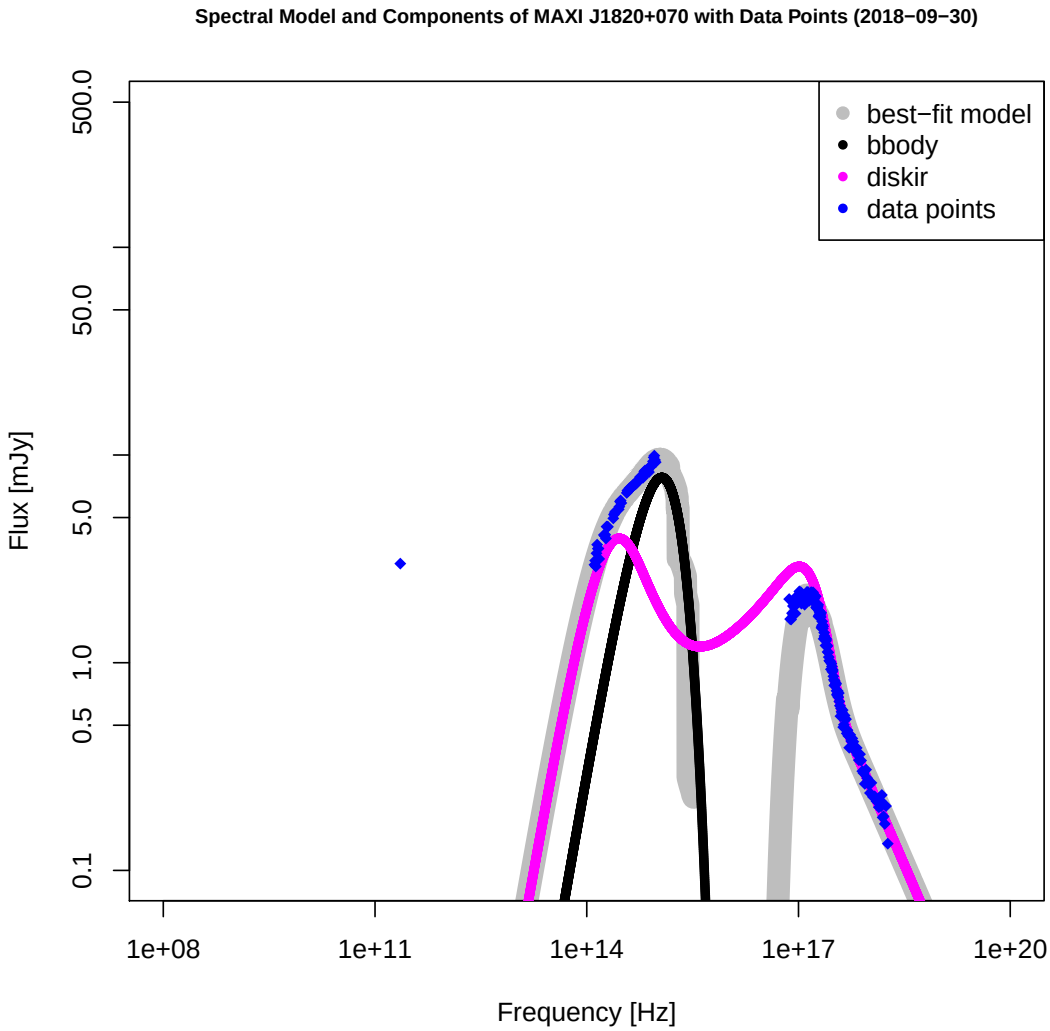

Figure 21: The MAXI J1820+070's 2018-09-30T00 multiwavelength observations with the spectral components, spectral model, and the data points. As there was only a single radio observation, the component **bknpower** was not used in the spectral modelling.

MAXI J1659-152

The best-fit model for the MAXI J1659−152 observations is displayed in figure 22, and the spectral model used was **tbabs(1)∗(bknpower(1)+diskir(1)+diskline(1))**. The two radio observation values were crucial, as they allowed for the usage of the **bknpower** component. This resulted in being able to determine the second jet break frequency ν_b versus the photon law index Γ of this master's thesis. The obtained jet break frequency ν_b value was $1.43^{+0.54}_{-0.27} \times 10^{-6}$ keV ($\approx 3.46^{+1.29}_{-0.66} \times 10^{11}$ Hz), and the photon law index Γ value was $1.700^{+0.003}_{-0.004}$. The rest of the parameters are given in appendix E.

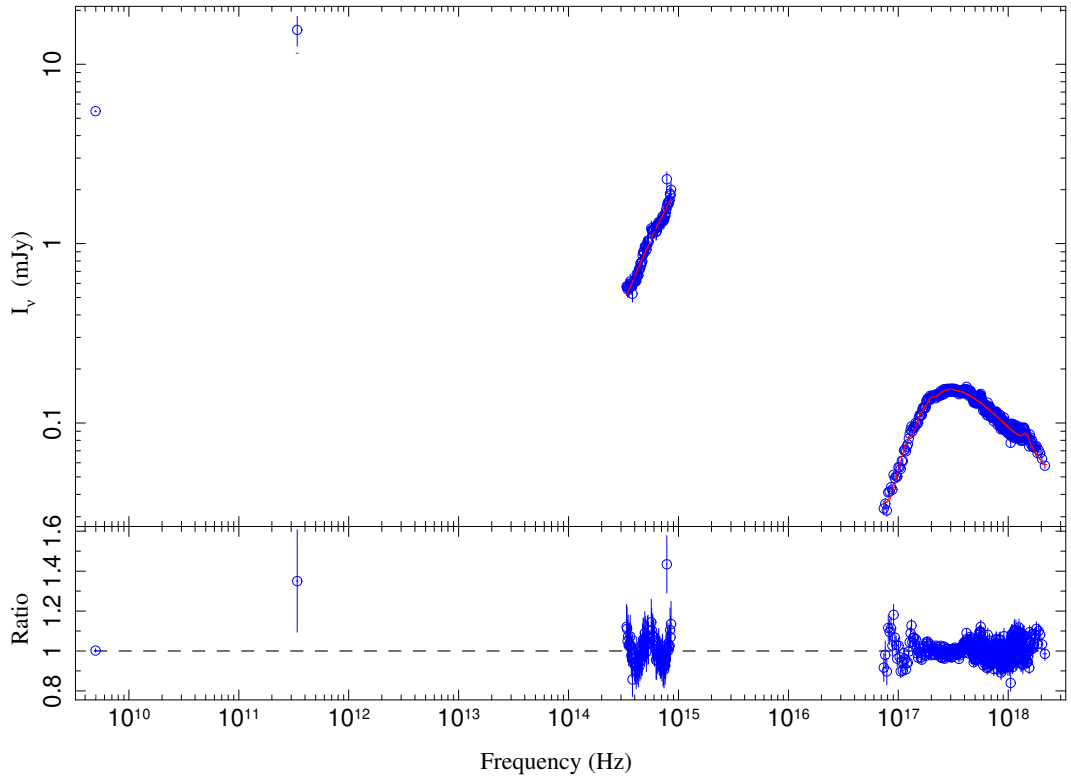

Figure 22: The MAXI J1659−152 multiwavelength observations with the fitted best-fit spectral model.

The spectral model components used for the MAXI J1659−152's data sets were **tbabs(1)∗(bknpower(1)+diskir(1)+diskline(1))**, and are plotted individually in figure 23. The components are unabsorbed.

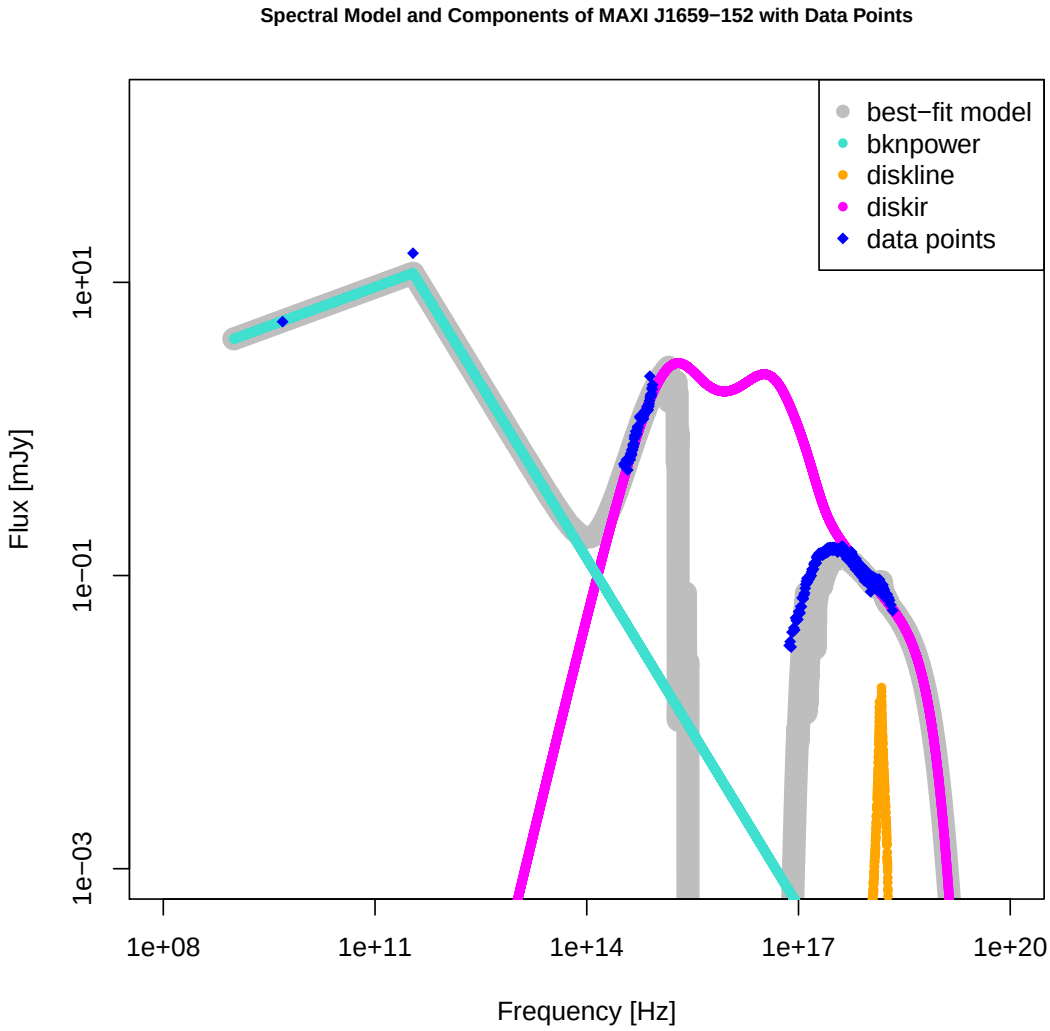

Figure 23: The MAXI J1659−152's observations with the spectral components, spectral model, and the data points.

SWIFT J1753.5-0127

The best-fit model for both of the SWIFT J1753.5−0127's observations was **tbabs(1)∗ diskir(1)** which can be seen plotted in figure 24. The parameters are given in appendix E.

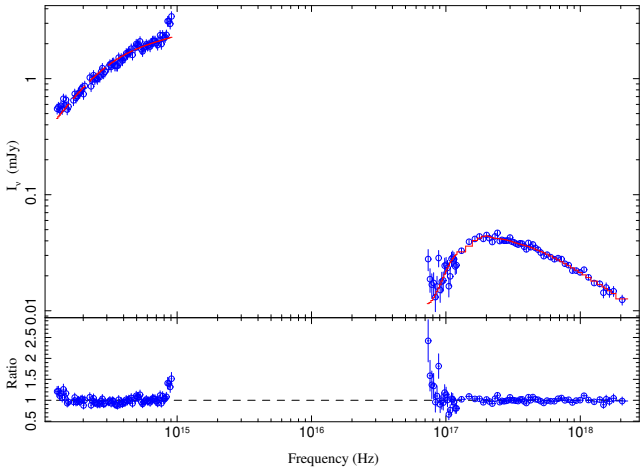

(a) 2014-08-16.

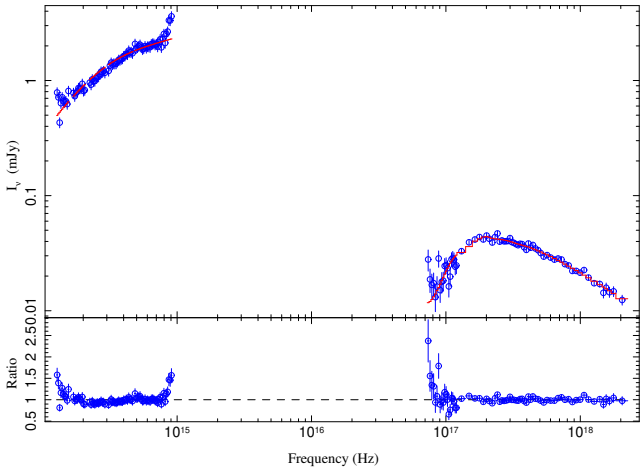

(b) 2014-08-17.

Figure 24: Both of the SWIFT J1753.5−0127's broadband observations with the best-fit spectral model.

The spectral model used for the SWIFT J1753.5−0127's both observations was **tbabs(1)∗diskir(1)**, and an example is presented in figure 25.

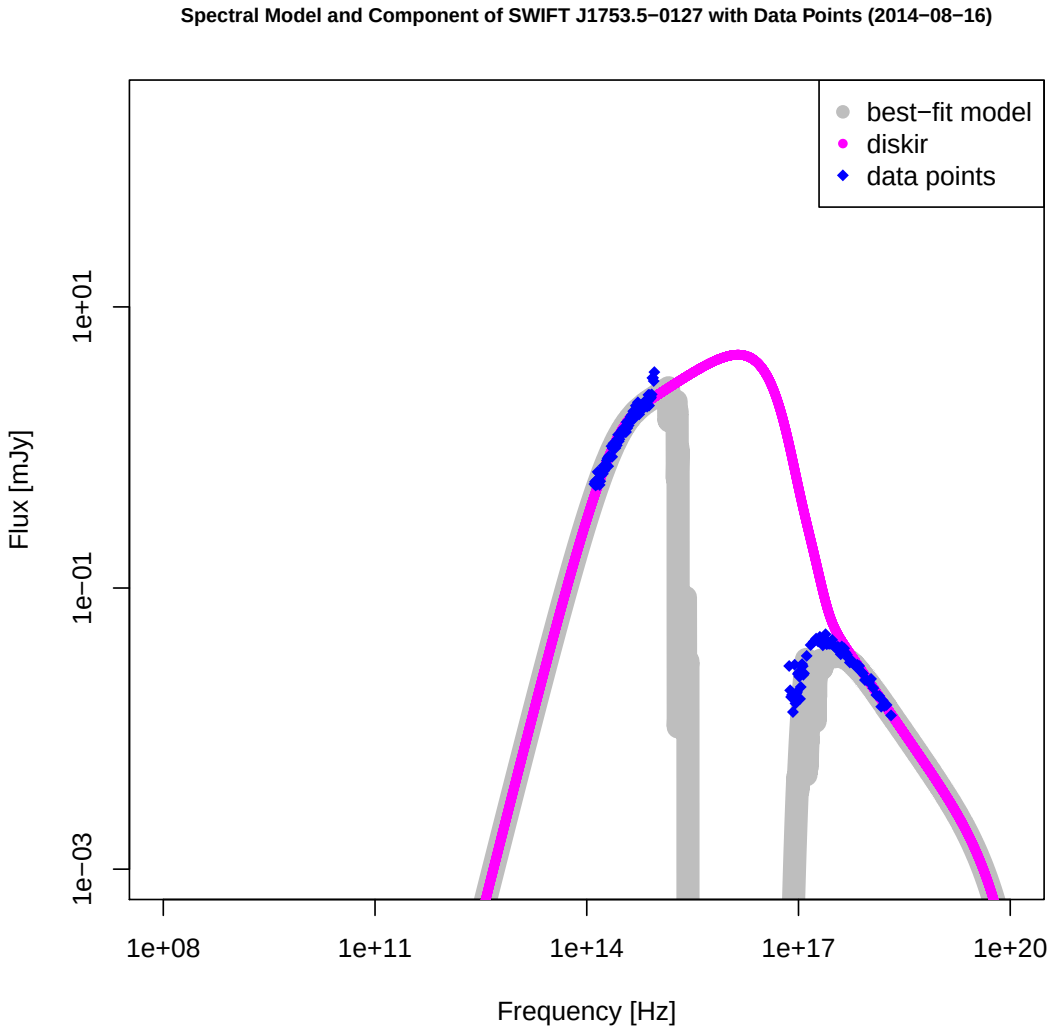

Figure 25: The SWIFT J1753.5−0127's 2014-08-16 multiwavelength observations with the spectral component, spectral model, and the data points.

GRS 1915+105

GRS 1915+105 had no usable data portions in the X-shooter's VIS and UVB ranges, only had a single radio measurement, and additionally had no measurements in the softer X-ray region provided by the *Swift*–XRT – it was the only target which was observed with the *RXTE*–PCA instrument. However, the best-fit spectral model was determined for the target's observations as well, which was **tbabs(1)*diskir(1)** for both of the observations (figure 26). The parameters are given in appendix E.

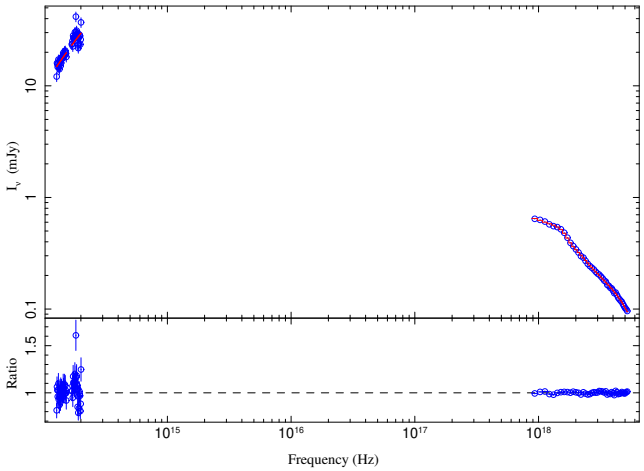

(a) 2010-09-19.

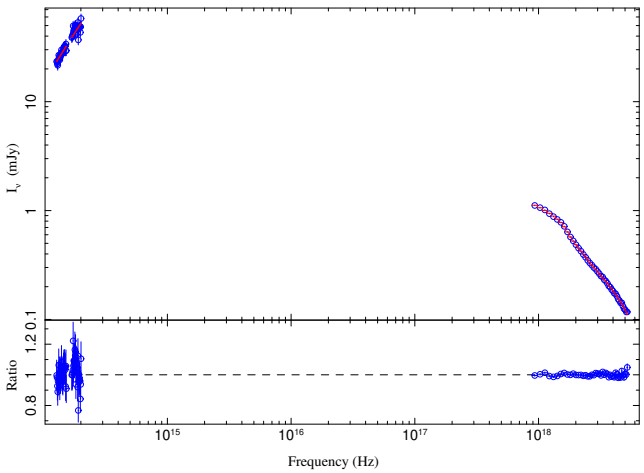

(b) 2010-09-24.

Figure 26: Both of the GRS 1915+105's multiwavelength observations with the best-fit spectral model.

The spectral model used for both of the GRS 1915+105's observations was **tbabs(1)*diskir(1)**, and an example is presented in figure 27.

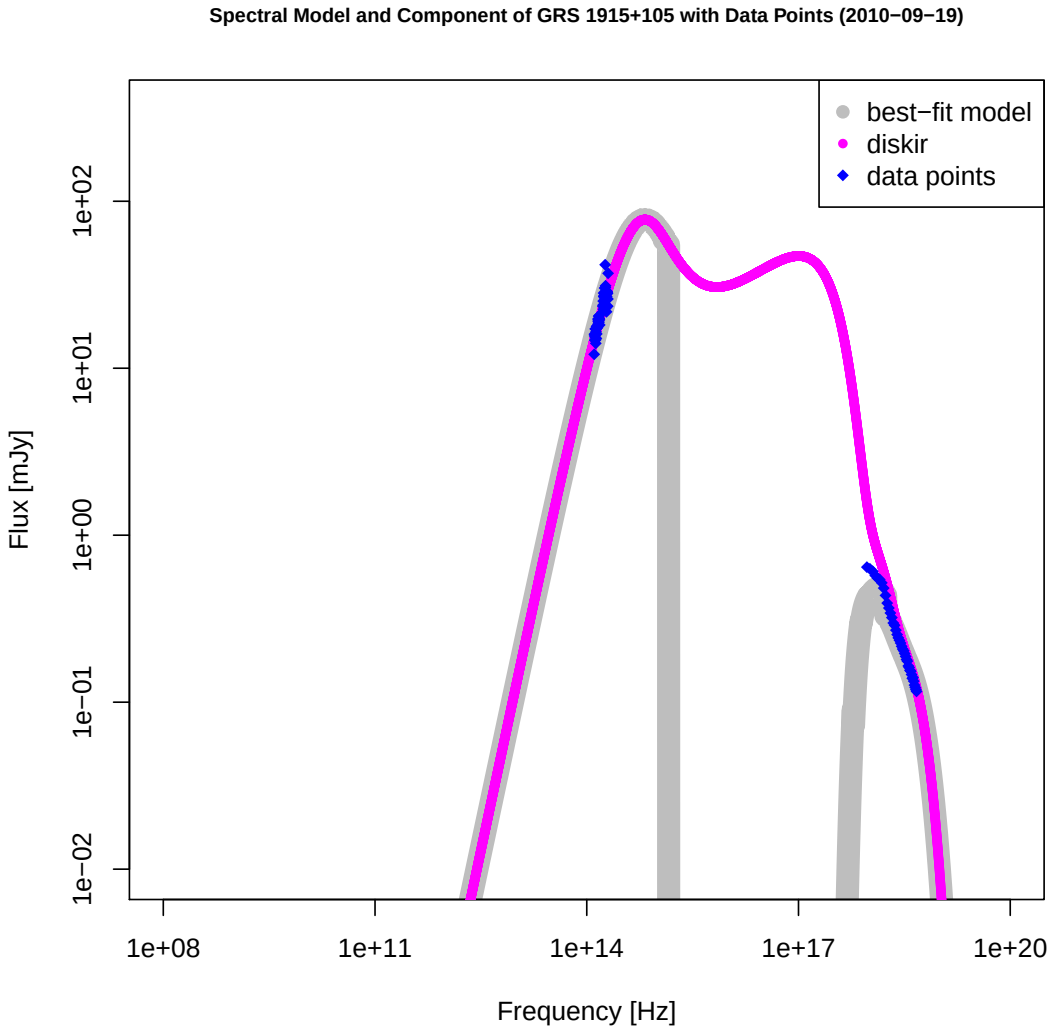

Figure 27: The GRS 1915+105's 2010-09-19 observations with the spectral component, spectral model, and the data points.

5. Discussion

The results of the selected targets were presented in the previous chapter for all of the observation periods. The MAXI J1820+070 was in the low/hard state in mid-April, 2018. This is recognisable from the Γ value of $1.56^{+0.22}_{-0.14}$ which corresponds to the typical low/hard X-ray spectral state's X-ray photon power law Γ value of ~ 1.7. The MAXI J1820+070's first observations from April of 2018 show it being in an active outburst state. The components used in the best-fit spectral model can be used to determine the emission regions responsible in the observations. The spectral component **bknpower** dominates the radio spectrum which is a clear indication of powerful astrophysical jets being present. The radio spectrum is bright with a power law, and thus synchrotron emission is the only option. The spectral component **bknpower** was used to model the conical, compact self-absorbed jet. We can see from figure 15 on page 74 that the astrophysical jets extend from the radio frequencies to the near-infrared wavelengths, and this emission comes from synchrotron radiation. The jet break frequency ν_b is located at $\approx 3.99^{+0.57}_{-1.13} \times 10^{13}$ Hz, and marks the boundary where the optically thin synchrotron emission changes to the optically thick emission during the observation period. The spectral component **diskir** was used to model both the accretion disk and the corona. The **diskir** component's parameter diskir(1).LcovrLd which models the ratio of luminosity in the Compton tail to that of the unilluminated accretion disk has a value of $3.11^{+1.27}_{-0.62}$ in the optimised best-fit model, and this translates to a highly illuminated Compton tail due to thermal Comptonisation. This is consistent with BHXRBs being in the hard state as the diskir(1).LcovrLd value is greater than 1 [127, 128].

The irradiated fraction (diskir(1).fout parameter) has a value of $0.010^{+0.006}_{-0.003}$, and this gives the reflected fraction of the illuminated flux. These results along with the parameters show that the coronal emission dominates the X-ray spectrum. The optical and ultraviolet spectrum emission is the result the from irradiation of the outer accretion disk by the coronal emission.

In mid-July 2018 the target has transitioned to the high/soft state where the accretion disk dominates, i.e. the spectral component **diskir** dominates thermally. There are no indications of astrophysical jets, and if the astrophysical jets are still present they have become significantly weak and are not being observed. The single radio point that was observed is most likely from the fading and optically thin radio emission which originated from the astrophysical jets, or shocks within the astrophysical jets. This transient jet which is emitting in radio is detached from the disk–jet system. The near-infrared to ultraviolet emission has faded compared to the mid-April observations, especially in the near-infrared part of the spectrum. The parameter diskir(1).LcovrLd has a value of $0.19^{+0.03}_{-0.03}$ in the best-fit models for 2018-07-13 and 2018-07-14, and in the best-fit model for 2018-07-15 the value is $0.14^{+0.10}_{-0.09}$, and these are consistent with the soft state where the diskir(1).LcovrLd should be less than 1 [128]. The irradiated fraction parameter, i.e. diskir(1).fout, has now dropped to values roughly $0.0003^{+0.0002}_{-0.0002}$ in the mid-July optimised best-fit models. The photon power law index Γ value of was fixed to 2.0 which represents a typical value for a black hole X-ray binary in the high/soft state. This along with the diskir(1).LcovrLd parameter's values in July being significantly lower than in the April's low/hard state, is a clear indication that the target has indeed transitioned to the soft state during July of 2018, and the black body emission is coming from the multicolour accretion disk.

The observations carried out in late September and early October of 2018 shows that the target has transitioned to the hard-intermediate state, and is transitioning from the previous soft state to the hard state. The photon power law index Γ value is between $1.80^{+0.02}_{-0.04}$ in all of the observations, and this translates to a typical hard spectrum with a Γ value of ~ 1.7. The diskir(1).fout values have remained the same as in the mid-July best-fits, and the values are $0.0003^{+0.0002}_{-0.0001}$ in the final observations of MAXI J1820+070, and these translate to a less reflected fraction of the illuminated flux than in the mid-April's hard state.

Furthermore, we can see how the MAXI J1820+070 evolved and transitioned between the periods of observations, starting from the low/hard state in mid-April, then transitioning to the high/soft state in mid-July. Then, finally shifting back towards the low/hard state – although less bright – in the observations carried out in late September and early October. These fit well to the classical "q-shaped" hardness–intensity diagram where the source starts from the hard state, transitions to the soft state, and then starts transcending back to the harder state.

The MAXI J1820+070 and its abundance of available multiwavelength data sets, most notably in April, proved to be the most valuable observation of this master's thesis. Additionally, the spectral component **bbody** was introduced to improve the fit, particularly at the UVB region, for the mid-July, late September and early October observations. However, more research is needed whether the extra **bbody** truly models a physical process that needs the excess black body component, or whether for instance the X-shooter's UVB region's observations were suffering from over correcting their interstellar extinction, and thus these data sets should be compared to other UVB data sets, e.g. the Ultra-Violet/Optical Telescope on-board *Swift*.

The determined results were verified with literature, and the spectral states reported in this master's thesis are in line with publications by Shidatsu et al. [131, 132] and Buisson et al. [133] who report in their research that the target was in the aforementioned spectral states during the corresponding observation periods. Furthermore, the determined spectral results are consistent with the observations carried with the *MAXI* [61] on-board the International Space Station [134]. The obtained photon law index Γ from April, 2018 with a value of $1.56^{+0.22}_{-0.14}$ is close to the reported value by Shidatsu et al. of ~ 1.5 [131]. The obtained photon law index Γ is also consistent with a BHXRB in the LH state, and thus additionally verifies the obtained results for mid-April, 2018. The MAXI J1820+070's mid-April observations provided the possibility of determining a novel value pair for the ν_b as a function of the Γ for BH systems [6].

A study by Veledina et al. [135] show that the optical emission during March and April of 2018 is most likely due to an irradiated accretion disk or by the scattering of the accretion disk's optically thin outflow. Kara et al. [136] presented that the corona's height was shrinking during the decay from the first hard state (March–April 2018), and Bright et al. [137] reported an isolated radio flare occurring between the hard to soft state transition period.

The results of MAXI J1659−152 indicate that it was in the low/hard state which can be seen from the photon power law index Γ value of $1.700^{+0.003}_{-0.004}$, and the diskir(1).LcovrLd parameter's value of $3.146^{+0.007}_{-0.006}$, which are both clear indicators of the hard spectral state where the coronal emission from Comptonisation dominates in the X-ray spectrum. These results are consistent with results presented by Kaur. et al. [138] who used the same X-shooter data available. Furthermore, the results are consistent with the light curves from the *MAXI* instrument [139], and publications by Muñoz-Darias et al. [140] and Kalamkar et al. [141] provide additional support to the spectral properties and state of the source presented in this thesis. Further simultaneous multiwavelength observations are highly encouraged for this target as well – particularly with the VISIR and X-shooter in cooperation along with radio and X-ray observations – in order to have additional radio and VISIR data points to further determine the jet break frequency ν_b and its shifting during the different spectral states.

The SWIFT J1753.5−0127 was in the low/hard state as well, and this was verified with the light curves from the *MAXI* instrument [142]. The spectral component **diskir** was used to model both of the observations, and the emission originates from the irradiating corona. The results were compared to results by Rahoui et al. [116] which used the very same X-shooter data sets with simultaneous X-ray and ultraviolet observations performed with the *Swift* telescope's and additionally radio data from the Australia Telescope Compact Array – though the radio data was only upper limits at two wavelengths due to poor weather conditions. Rahoui et al. also modelled the observations only with the **diskir** component, and additionally with the **diskir** and with an additional **bbody** and **bknpower** component, respectively. The Γ values of $1.78^{+0.02}_{-0.02}$ for the model **tbabs(1)∗(diskir(1)**, and $1.70^{+0.03}_{-0.03}$ for the model **tbabs(1)∗(diskir(1)+bbody(1))** by Rahoui et al. match the Γ value of $1.74^{+0.05}_{-0.04}$ obtained for both of the best-fit models in this master's thesis. The publication by Rahoui et al. [116] shows that the X-shooter's UVB proportion was screened out completely, and the ultraviolet observations taken with the *Swift's* telescope do not fully match the X-shooter's UVB fluxes presented in this master's thesis. The X-shooter's UVB region seems to be affected in each of the other observations used in this thesis – and hence might be why the UVB proportion was not used in Rahoui et al. [116].

The case with the GRS 1915+105 proved to be slightly more troublesome as it lacked significant usable data portions in the X-shooter region, and had only a single radio observation that was observed after the X-shooter core observations. Thus, the spectral model along with the spectral state – hard state – could be determined, but calling this a proper multiwavelength observation would be stretching it. Previously Steeghs et al. [77] have studied the GRS 1915+105 with the very same X-shooter observations, and they have only concentrated on the NIR portion of the overall X-shooter coverage – i.e. the very same portion that remained after screening out the severely affected VIS and UVB regions.

Ultimately, this master's thesis presents results for all the set goals which were fulfilled, and additionally this master's thesis succeeds in presenting two novel value pairs to the photon law index Γ versus the jet break frequency ν_b that was originally published in Koljonen et al. [6]. The new values are from two separate targets, the first value was determined from the MAXI J1820+070's April observations from 2018 with a photon law index Γ value of $1.56^{+0.22}_{-0.14}$ and a jet break frequency ν_b value of $3.99^{+0.57}_{-1.13} \times 10^{13}$ Hz, and the second value was determined from the MAXI J1659−152's observations with a photon law index Γ value of $1.700^{+0.003}_{-0.004}$ and a jet break frequency ν_b value of $3.46^{+1.29}_{-0.66} \times 10^{11}$ Hz. Both of the new value pairs show additional support to the research by Koljonen et al. as the values fit well to the original jet break frequency ν_b as a function of the X-ray photon power law index Γ scatter plot for black hole systems [6]. Thus, further simultaneous multiwavelength studies are highly recommended especially with contemporaneous X-shooter and VISIR observations along with dedicated concurrent radio and X-ray monitoring. These will further validate whether the empirical connection is present at all accreting black hole systems at different spectral states, e.g. during quiescent.

6. Conclusion

This master's thesis studied low-mass BHXRBs which are double star systems where a non-degenerate main-sequence donor star feeds the accretor, i.e. a stellar-mass BH or a NS, through Roche lobe overflow. The matter flowing from the donor to the accretor forms an optically thick and geometrically thin accretion disk around the accretor which is hot and radiating in the X-ray spectrum. XRBs undergo periods of different accretion rates, and these translate to two classical spectral states – i.e. the LH, and the HS – along with multiple intermediate and more refined spectral states, e.g. the VH, the QO, and the hypersoft state. The accretion disk and astrophysical jets are related to each other through the disk–jet connection, and this disk–jet connection is responsible for the different spectral states that are dependent on the accretion flow parameters. XRBs exhibit quasi-steady and highly collimated astrophysical jets in the hard spectral state, whereas this feature is never the case in the soft spectral state – although there have been research performed which hypothesise the presence of astrophysical jets called "dark jets" even in the soft state. XRBs not only radiate in the X-ray wavelengths but across the whole electromagnetic spectrum, and there are many contributing emission mechanisms taking place in the different parts of the XRBs – these include the astrophysical jets, the accretion disk, and the centre region of the accretion disk called the corona – and at different periods of accretion flow within the system. The emission features associated with XRBs include radio and millimetre emission from the astrophysical jets, mid-infrared to ultraviolet emission from multiple possible emission mechanisms, and X-ray emission from the accretion flow itself.

The emission processes at the VLT's X-shooter bands, i.e. from the near-infrared to the ultraviolet spectrum, are most likely a combination of several contributing factors which can traced to the synchrotron radiation coming from the astrophysical jets, the X-ray irradiated emission coming from the heated accretion disk, and the synchrotron emission coming from the inner accretion flow – which are dependent on the state of the accretion.

Thus, the usage of the X-shooter instrument is an ideal observation method to distinguish the different possible emission mechanisms in the near-infrared to the ultraviolet regions at different observation periods, and is currently the only instrument capable of simultaneous and broadband observations in this wavelength region. Contemporaneous observations with the VISIR instrument offer valuable complementary mid-infrared measurements to the X-shooter's spectrum range, and thus further enhance the possibility of distinguishing the different emission processes taking place in the mid-infrared to the ultraviolet region. These research methods are especially vital when conducting research on X-ray binary outbursts, their disk–jet connection, and the spectral states they display during different periods of accretion flow. Additionally, the least known dominating emission processes in low-mass X-ray binaries are situated in the visible to the near-infrared wavelengths, and thus observations with the X-shooter can provide substantial new results to this particular wavelength region.

The overall aim of this master's thesis was provide more insight to the unanswered research questions which can help in determining the origins of the disk–jet connection, and its direct applications – e.g. what enables the astrophysical jets to be formed, launched and suppressed, what are the fundamental properties of the astrophysical jets and the accretion disk, what is the energy and particle distribution in the astrophysical jets, what are the large-scale physical structures of the accretion disk – especially in the X-shooter bands. The answers for these research questions would ultimately solve whether the astrophysical jets and their fundamental properties and processes are ubiquitous to all accreting black hole systems that range from stellar-mass black hole X-ray binaries to supermassive black holes found in active galactic nuclei.

The novel results were verified by the master's thesis supervisor. The novel broadband multiwavelength observation campaign results are currently in preparation to be published in upcoming publications.

It is without a doubt that we need further multiwavelength observation campaigns of black hole X-ray binary transients in the near-future. Not only is there clear a need to study low-mass X-ray binaries and other X-ray transients more frequently to be able to determine the fundamental processes governing the astrophysical jets, there is additionally a fundamental need to widen the research to consist of low-mass X-ray binary stars in a variety of different evolutionary stages in order to unify the models related to the disk–jet connection, and its applications to active galactic nuclei, i.e. do active galactic nuclei have a hardness–intensity diagram of their own that can be modelled and unified using the black hole X-ray binaries hardness–intensity diagram as a proxy?

Fortunately, there are plans and aims to set up at least two new instruments capable of broadband observations spanning from the near-infrared to the ultraviolet wavelengths. These near-future ground-based instruments that are being established are the Son of X-shooter (SOXS) and the Nordic Optical Telescope's Transient Explorer (NTE). Both of the upcoming instruments will provide additional coverage to the X-shooter's covered wavelength bands.

The SOXS instrument will be installed on the New Technology Telescope which is located at ESO's La Silla Observatory in Chile. The main purpose of SOXS is to be a dedicated instrument suitable of devoted follow-up observations of transient sources, e.g. black hole X-ray binaries. The SOXS instrument will cover the ultraviolet, visible and near-infrared bands at wavelengths of 350–2000 nm. [143, 144] The NTE will cover the wavelengths from 335 nm to 2200 nm, and is expected to capture its first light in 2021. [145] Both the SOXS instrument and the NTE instrument follow design principles and ideas of the successful X-shooter instrument, and these instruments will provide additional much needed spectral coverage to black hole X-ray binaries.

Acknowledgements

I would like to thank all of the individuals who contributed in providing the radio and mid-infrared data sets for the MAXI J1820+070 observations used in this master's thesis. These data sets were generously provided by A. Tetarenko (VLA, SMA, & ALMA), S. Trushkin (RATAN–600), and D. Russell (VLT's VISIR).

References

[1] Koljonen, K. I. I. et al. The hardness–intensity diagram of Cygnus X-3: Revisiting the radio/X-ray states. *Monthly Notices of the Royal Astronomical Society,* 2010, Vol. 406, Issue 1, pp. 307–319. DOI https://doi.org/10.1111/j.1365-2966.2010.16722.x.

[2] Koljonen, K. I. I. et al. Unsupervised spectral decomposition of X-ray binaries with application to GX 339-4. *Monthly Notices of the Royal Astronomical Society,* 2015, Vol. 447, Issue 4, pp. 2981–2991. DOI https://doi.org/10.1093/mnras/stu2663.

[3] Koljonen, K. I. I. et al. Evidence of spreading layer emission in thermonuclear superbursts. *The Astrophysical Journal,* 2016, Vol. 829, Number 2. DOI https://doi.org/10.3847/0004-637X/829/2/91.

[4] Russell, T. D. et al. The accretion–ejection coupling in the black hole candidate X-ray binary MAXI J1836 -194. *Monthly Notices of the Royal Astronomical Society,* 2014, Vol. 439, Issue 2, pp. 1390–1402. DOI https://doi.org/10.1093/mnras/stt2498.

[5] Russell, T. D. et al. Rapid compact jet quenching in the Galactic black hole candidate X-ray binary MAXI J1535-571. *Monthly Notices of the Royal Astronomical Society,* Accepted for publication. DOI https://doi.org/10.1093/mnras/staa2650.

[6] Koljonen, K. I. I. et al. A connection between plasma conditions near black hole event horizons and outflow properties. *The Astrophysical Journal,* 2015, Vol. 814, Number 2. DOI https://doi.org/10.1088/0004-637X/814/2/139.

[7] High Energy Astrophysics Science Archive Research Center. Xamin Web Interface. (Online) Available https://heasarc.gsfc.nasa.gov/xamin/xamin.jsp.

[8] Psaltis, D. Accreting neutron stars and black holes: A decade of discoveries. In Lewin, W. & van der Klis, M. (eds.). *The Compact Stellar X-ray Sources.* Cambridge University Press, 2006, pp. 1–38.

[9] Giacconi, R. et al. Evidence for X-rays from sources outside the Solar System. *Physical Review Letters,* 1962, Vol. 9, Number 11. DOI https://doi.org/10.1103/PhysRevLett.9.439

[10] Giacconi, R. Nobel lecture: The dawn of X-ray astronomy. *Reviews of Modern Physics,* 2003, Vol. 75.

[11] The European Southern Observatory. Announcement – Riccardo Giacconi (1931–2018). 11 December 2018. (Online) Accessed 9 September 2019. Available https://www.eso.org/public/announcements/ann18090/.

[12] Bradshaw, C. F. et al. High-resolution parallax measurements of Scorpius X-1. *The Astrophysical Journal Letters,* 2004, Vol. 512, Number 2. DOI https://doi.org/10.1086/311889.

[13] Liu, Q. Z. et al. A catalogue of low-mass X-ray binaries in the Galaxy, LMC, and SMC (Fourth edition). *Astronomy & Astrophysics,* 2007, Vol. 469, Number 2, pp. 807–810. DOI https://doi.org/10.1051/0004-6361:20077303.

[14] Liu, Q. Z. et al. Catalogue of high-mass X-ray binaries in the Galaxy (4th edition). *Astronomy & Astrophysics,* 2006, Vol. 455, Number 3, pp. 1165–1168. DOI https://doi.org/10.1051/0004-6361:20064987.

[15] Frank, J., King, A., & Raine, D. *Accretion Power in Astrophysics.* Third edition. Cambridge, Cambridge University Press, 2002.

[16] Philip Armitage – University of Colorado. ASTR 3730: Astrophysics 1 – Lecture 18: Stars: Eddington limit. 2003. (Online) Accessed 2 February 2020. Available https://jila.colorado.edu/~pja/astr3730/lecture18.pdf.

[17] Garrett – University of Oxford. Radiative Processes in Astrophysics – High-Energy Astrophysics: Lecture 7. 2012. (Online) Accessed 2 February 2020. Available http://www-astro.physics.ox.ac.uk/~garret/teaching/lecture7-2012.pdf.

[18] Karttunen, H., Kröger, P., Oja, H., Poutanen, M. & Donner, K. J. *Fundamental Astronomy.* Fifth edition. Springer, 2007.

[19] Chandrasekhar, S. & Milne, E. A. The highly collapsed configurations of a stellar mass. *Monthly Notices of the Royal Astronomical Society,* 1931, Vol. 91, Issue 5, pp. 456–466. DOI https://doi.org/10.1093/mnras/91.5.456.

[20] Chandrasekhar, S. On stars, their evolution and their stability. *Reviews of Modern Physics,* 1984, Vol. 56, Issue 2 pp. 137–147. DOI https://link.aps.org/doi/10.1103/RevModPhys.56.137.

[21] Oppenheimer, J. R. & Volkoff, G. M. On massive neutron cores. *Physical Review,* 1939, Vol. 55, Issue 4. DOI https://doi.org/10.1103/PhysRev.55.374

[22] Tolman, R. C. Static solutions of Einstein's field equations for spheres of fluid. *Physical Review,* 1939, Vol. 55, Issue 4. DOI https://doi.org/10.1103/PhysRev.55.364

[23] Montgomery, C. et al. Michell, Laplace and the origin of the black hole concept. *Journal of Astronomical History and Heritage,* 2009, Vol. 12, Number 2, pp. 90–96. Available http://articles.adsabs.harvard.edu/full/2009JAHH...12...90M.

[24] Einstein, A. Die Feldgleichungen der Gravitation. *Sitzungsberichte der Preussischen Akademie der Wissenschaften zu Berlin,* 1915, pp. 844–847. Available http://articles.adsabs.harvard.edu/cgi-bin/get_file?pdfs/SPAW./1915/1915SPAW.....844E.pdf.

[25] Einstein, A. Die Grundlage der allgemeinen Relativitätstheorie. *Annalen der Physik,* 1916, Vol. 354, Issue 7. DOI https://doi.org/10.1002/andp.19163540702.

[26] Schwarzschild, K. Über das Gravitationsfeld eines Massenpunktes nach der Einsteinschen Theorie. *Sitzungsberichte der Preussischen Akademie der Wissenschaften zu Berlin,* 1916, pp. 189–196. Available http://articles.adsabs.harvard.edu/cgi-bin/get_file?pdfs/SPAW./1916/1916SPAW.....189S.pdf.

[27] Droste, J. The field of a single centre in Einstein's theory of gravitation, and the motion of a particle in that field. *Koninklijke Nederlandsche Akademie van Wetenschappen Proceedings,* 1917, pp. 197–215. Available https://www.dwc.knaw.nl/DL/publications/PU00012346.pdf.

[28] Reissner, H. Über die Eigengravitation des elektrischen Feldes nach der Einsteinschen Theorie. *Annalen der Physik,* 1916, Vol. 355, Issue 9. DOI https://doi.org/10.1002/andp.19163550905.

[29] Nordström, G. On the energy of the gravitation field in Einstein's theory. *Koninklijke Nederlandsche Akademie van Wetenschappen Proceedings,* 1918, Vol. 20, Issue 2.

[30] Weyl, H. Zur Gravitationstheorie. *Annalen der Physik,* 1917, Vol. 359, Issue 18. DOI https://doi.org/10.1002/andp.19173591804.

[31] Jeffery, G. B. The field of an electron on Einstein's theory of gravitation. *Proceedings of the Royal Society of London. Series A,* 1921, Vol. 99, Issue 697. DOI https://doi.org/10.1098/rspa.1921.0028.

[32] Kerr, R. P. Gravitational Field of a Spinning Mass as an Example of Algebraically Special Metrics. *Physical Review Letters,* 1963, Vol. 11, Number 5. DOI https://doi.org/10.1103/PhysRevLett.11.237

[33] Newman, E. T. & Janis, A. I. Note on the Kerr spinning-particle metric. *Journal of Mathematical Physics,* 1965, Vol. 6. DOI https://doi.org/10.1063/1.1704350.

[34] Newman, E. T. et al. Metric of a rotating, charged mass. *Journal of Mathematical Physics,* 1965, Vol. 6. DOI https://doi.org/10.1063/1.1704351. power

[35] Charles, P. A. & Coe, M. J. Optical, ultraviolet and infrared observations of X-ray binaries. In Lewin, W. & van der Klis, M. (eds.). *Compact Stellar X-ray Sources.* Cambridge University Press, 2006, pp. 215–266.

[36] Tauris, M. & , M. J. Formation and evolution of compact stellar X-ray sources. In Lewin, W. & van den Heuvel, E. (eds.). *Compact Stellar X-ray Sources.* Cambridge University Press, 2006, pp. 623–666.

[37] Castor, J. I. et al. Radiation-driven winds in Of stars. *The Astrophysical Journal,* 1975, Vol. 195. DOI https://doi.org/10.1086/153315.

[38] Page, D. N. & Thorne, K. S. Disk-accretion onto a black hole. I. Time-averaged structure of accretion disk. *The Astrophysical Journal,* 1974, Vol. 191. DOI https://doi.org/10.1086/152990.

[39] Shakura, N. I. & Sunyaev, R. A. Black holes in binary systems. Observational appearance. *Astronomy & Astrophysics,* 1973, Vol. 24, pp. 337–355. Available http://articles.adsabs.harvard.edu/full/1973A%26A....24..337S.

[40] Shakura, N. I. & Sunyaev, R. A. A theory of the instability of disk accretion on to black holes and the variability of binary X-ray sources, galactic nuclei and quasars. *Monthly Notices of the Royal Astronomical Society,* 1976, Vol. 175, Issue 3, pp. 613–632. DOI https://doi.org/10.1093/mnras/175.3.613.

[41] Shapiro, S. L. et al. A two-temperature accretion disk model for Cygnus X-1: Structure and spectrum. *The Astrophysical Journal,* 1976, Vol. 204. DOI https://doi.org/10.1086/154162.

[42] Narayan, R. & Yi, I. Advection-dominated accretion: Underfed black holes and neutron stars. *The Astrophysical Journal,* 1995, Vol. 452. DOI https://doi.org/10.1086/176343.

[43] Planck, M. Ueber das Gesetz der Energieverteilung im Normalspectrum. *Annalen der Physik,* 1901, Vol. 309, Issue 1. DOI https://doi.org/10.1002/andp.19013090310.

[44] Planck, M. *The theory of heat radiation.* P. Blakiston's Son & Co., Philadelphia, PA, 1914.

[45] Fender, R. Jets from X-ray binaries. In Lewin, W. & van der Klis, M. (eds.). *Compact Stellar X-ray Sources.* Cambridge University Press, 2006.

[46] Fender, R. P. et al. MERLIN observations of relativistic ejections from GRS 1915+105. *Monthly Notices of the Royal Astronomical Society,* 1999, Vol. 304, Issue 4, pp. 865–876. DOI https://doi.org/10.1046/j.1365-8711.1999.02364.x.

[47] Koljonen, K. I. I. The multiwavelength spectral and timing nature of the microquasar Cygnus X-3. *Aalto University publication series DOCTORAL DISSERTATIONS, 129/2013,* Aalto University, 2013. Available http://urn.fi/URN:ISBN:978-952-60-5297-7.

[48] Penrose, R. & Floyd, R. M. Extraction of rotational energy from a black hole. *Nature Physical Science,* 1971, Vol. 229, Issue 6, pp. 177–179. DOI https://doi.org/10.1038/physci229177a0.

[49] Blandford, R. D. & Znajek, R. L. Electromagnetic extraction of energy from Kerr black holes. *Monthly Notices of the Royal Astronomical Society,* 1977, Vol. 179, Issue 3, pp. 433–456. DOI https://doi.org/10.1093/mnras/179.3.433.

[50] MacDonald, D. & Thorne, K. K. Black-hole electrodynamics: An absolute-space/universal-time formulation. *Monthly Notices of the Royal Astronomical Society,* 1982, Vol. 198, Issue 2, pp. 345–382. DOI https://doi.org/10.1093/mnras/198.2.345.

[51] Blandford, R. D. & Payne, D. G. Hydromagnetic flows from accretion discs and the production of radio jets. *Monthly Notices of the Royal Astronomical Society,* 1982, Vol. 199, Issue 4, pp. 883–903. DOI https://doi.org/10.1093/mnras/199.4.883.

[52] Fender, R. Relativistic outflows from X-ray binaries ('Microquasars'). In Guthmann, A. W. et al. (eds.) *Relativistic Flows in Astrophysics.* Springer, 2002, pp. 101–122.

[53] Fender, R. 'Disc–jet' coupling in black hole X-ray binaries and active galactic nuclei.). In Belloni, T. (ed.) *The Jet Paradigm.* Springer, 2010, pp. 115–142.

[54] McClintock, J. E. & Remillard, R. A. Black hole binaries. In Lewin, W. & van der Klis, M. (eds.). *Compact Stellar X-ray Sources.* Cambridge University Press, 2006.

[55] Tananbaum, H. et al. Observation of a correlated X-ray transition in Cygnus X-1. *The Astrophysical Journal,* 1972, Vol. 177. DOI https://doi.org/10.1086/181042.

[56] Jeroen, H. Observational overview of state transitions in X-ray binaries. (Online) Accessed 1 September 2019. Available https://cxc.harvard.edu/cdo/accr10/pres/Homan_Jeroen.pdf.

[57] van der Klis, M. Rapid X-ray variability. In Lewin, W. & van der Klis, M. (eds.). *Compact Stellar X-ray Sources.* Cambridge University Press, 2006.

[58] Done, C. et al. Modelling the behaviour of accretion flows in X-ray binaries. *The Astronomy and Astrophysics Review,* 2007, Vol. 15, pp. 1–66. DOI https://doi.org/10.1007/s00159-007-0006-1.

[59] Tucker, M. A. et al. ASASSN-18ey: The rise of a new black hole X-ray binary. *The Astrophysical Journal Letters,* 2018, Vol. 867, Number 1. DOI https://doi.org/10.3847/2041-8213/aae88a.

[60] Kawamuro, T. et al. MAXI/GSC detection of a probable new X-ray transient MAXI J1820+070. *The Astronomer's Telegram,* 11 March 2018, Number 11399. Available http://www.astronomerstelegram.org/?read=11399.

[61] Matsuoka, M. et al. The MAXI mission on the ISS: Science and instruments for monitoring all-sky X-ray images. *Publications of the Astronomical Society of Japan,* 2009, Vol. 61. DOI https://doi.org/10.1093/pasj/61.5.999.

[62] Mihara, T. et al. Gas Slit Camera (GSC) onboard MAXI on ISS. *Publications of the Astronomical Society of Japan,* 2011, Vol. 63. DOI https://doi.org/10.1093/pasj/63.sp3.S623.

[63] Baglio, M. C. et al. Optical observations of MAXI J1820+070 suggest it is a black hole X-ray binary. *The Astronomer's Telegram,* 14 March 2018, Number 11418. Available http://www.astronomerstelegram.org/?read=11418.

[64] Abstracts – ESO Observing Programmes. Disentangling the emission processes of X-ray binary outbursts with X-Shooter. (Online) Available http://archive.eso.org/wdb/wdb/eso/abstract/query?progid=0101.D-0356(A).

[65] Torres, M. A. P. et al. Dynamical confirmation of a black hole in MAXI J1820+070. *The Astrophysical Journal Letters,* 2020, Vol. 882, Number 2. DOI https://doi.org/10.3847/2041-8213/ab39df.

[66] Torres, M. A. P. et al. The binary mass ratio in the black hole transient MAXI J1820+070. *The Astrophysical Journal Letters,* 2020, Vol. 893, Number 2. DOI https://doi.org/10.3847/2041-8213/ab863a.

[67] Atri, P. et al. A radio parallax to the black hole X-ray binary MAXI J1820+070. *Monthly Notices of the Royal Astronomical Society,* 2020, Vol. 493, Issue 1, pp. L81–L86. DOI https://doi.org/10.1093/mnrasl/slaa010.

[68] Kuulkers, E. et al. MAXI J1659−152: The shortest orbital period black-hole transient in outburst. *Astronomy & Astrophysics,* 2013, Vol. 552, Article number A32. DOI https://doi.org/10.1051/0004-6361/201219447.

[69] Corral-Santana, J. M. et al. BlackCAT: A catalogue of stellar-mass black holes in X-ray transients. *Astronomy & Astrophysics,* 2016, Vol. 587, Article number A61. DOI https://doi.org/10.1051/0004-6361/201527130.

[70] Science & Exploration. Black hole-star pair orbiting at dizzying speed. 19 March 2013. (Online) Accessed 14 September 2019. Available http://www.esa.int/Science_Exploration/Space_Science/Black_hole-star_pair_orbiting_at_dizzying_speed/.

[71] Jonker, P. G. et al. The black hole candidate MAXI J1659−152 in and towards quiescence in X-ray and radio. *Monthly Notices of the Royal Astronomical Society,* 2012, Vol. 423, Issue 4, pp. 3308–3315. DOI https://doi.org/10.1111/j.1365-2966.2012.21116.x.

[72] Zurita, C. et al. Swift J1753.5−0127: The black hole candidate with the shortest orbital period. *The Astrophysical Journal,* 2008, Vol. 681, Number 2. DOI https://doi.org/10.1086/588721.

[73] Shaw, A. W. et al. No evidence for a low-mass black hole in Swift J1753.5−0127. *Monthly Notices of the Royal Astronomical Society,* 2016, Vol. 463, Issue 2, pp. 1314–1322. DOI https://doi.org/10.1093/mnras/stw2092.

[74] Shaw, A. W. et al. The curious case of Swift J1753.5−0127: A black hole low-mass X-ray binary analogue to Z cam type dwarf novae. *Monthly Notices of the Royal Astronomical Society,* 2019, Vol. 482, Issue 2, pp. 1840–1857. DOI https://doi.org/10.1093/mnras/sty2787.

[75] INTEGRAL Science Data Centre. Science with INTEGRAL. (Online) Accessed 14 September 2019. Available http://www.isdc.unige.ch/integral/outreach/science/.

[76] Mirabel, I. F. et al. A superluminal source in the Galaxy. *Nature,* 1994, Vol. 371, Number 6492, pp. 46–48. DOI https://doi.org/10.1038/371046a0.

[77] Steeghs, D. et al. The not-so-massive black hole in the microquasar GRS1915+105. *The Astrophysical Journal,* 2013, Vol. 768. DOI https://doi.org/10.1088/0004-637X/768/2/185.

[78] Reid, M. J. et al. A parallax distance to the microquasar GRS 1915+105 and a revised estimate of its black hole mass. *The Astrophysical Journal,* 2014, Vol. 796, Number 1. DOI https://doi.org/10.1088/0004-637X/796/1/2.

[79] Vernet, J. et al. X-shooter, the new wide band intermediate resolution spectrograph at the ESO Very Large Telescope. *Astronomy & Astrophysics,* 2011, Vol. 536, Article number A105. DOI https://doi.org/10.1051/0004-6361/201117752.

[80] ESO Science Archive Facility. X-shooter raw data query form. (Online) Available http://archive.eso.org/wdb/wdb/eso/xshooter/form.

[81] Observational Raw Data Query Results. List of MAXI J1820+070 X-shooter raw files. (Online) Available http://archive.eso.org/wdb/wdb/eso/eso_archive_main/query?prog_id=0101.D-0356(A)&max_rows_returned=10000.

[82] Lagage, P. O. et al. Successful commissioning of VISIR: The mid-infrared VLT instrument. *The Messenger,* 2004, Number 117, pp. 12–16. Available http://www.eso.org/sci/publications/messenger/archive/no.117-sep04/messenger-no117-12-16.pdf.

[83] Wootten, A. et al. The Atacama Large Millimeter/Submillimeter Array. *Proceedings of the IEEE,* 2009, Vol. 97, Number 8, pp. 1463–1471. DOI https://doi.org/10.1109/JPROC.2009.2020572.

[84] Güsten, R. et al. The Atacama Pathfinder EXperiment (APEX) – a new submillimeter facility for southern skies –. *Astronomy & Astrophysics,* 2006, Vol. 454, Number 2, pp. L13–L16. DOI https://doi.org/10.1051/0004-6361:20065420.

[85] Zwart, J. T. L. et al. The Arcminute Microkelvin Imager. *Monthly Notices of the Royal Astronomical Society,* 2008, Vol. 391, Issue 4, pp. 1545–1558. DOI https://doi.org/10.1111/j.1365-2966.2008.13953.x.

[86] Healy, K. R. A window on the plasma Universe: The Very Large Array. *Astrophysics and Space Science,* 1995, Vol. 227, pp. 83–91. DOI https://doi.org/10.1007/BF00678068.

[87] The National Radio Astronomy Observatory. Welcome to the Very Large Array!. 21 August 2019. (Online) Accessed 8 September 2019. Available http://www.vla.nrao.edu/.

[88] The National Radio Astronomy Observatory. Very Large Array. (Online) Accessed 17 April 2020. Available https://public.nrao.edu/telescopes/vla/.

[89] Thompson, A. R. et al. The Very Large Array. *The Astrophysical Journal Supplement Series,* 1980, Vol. 44. DOI https://doi.org/10.1086/190688.

[90] Napier, P. J. et al. The Very Large Array: Design and performance of a modern synthesis radio telescope. *Proceedings of the IEEE,* 1983, Vol. 71, Number 11, pp. 1295–1320. DOI https://doi.org/10.1109/PROC.1983.12765.

[91] van Haarlem, M. P. et al. LOFAR: The LOw-Frequency ARray. *Astronomy & Astrophysics,* 2013, Vol. 556, Article number A2. DOI https://doi.org/10.1051/0004-6361/201220873.

[92] Parijskij, Y. N. et al. RATAN-600: The world's biggest reflector at the 'cross roads'. *IEEE Antennas and Propagation Magazine,* 1993, Vol. 35, Number 4, pp. 7–12. DOI https://doi.org/10.1109/74.229840.

[93] Ho, P. T. P. et al. The Submillimeter Array. *The Astrophysical Journal Letters,* 2004, Vol. 616, Number 1. DOI https://doi.org/10.1086/423245.

[94] Baars, J. W. M. et al. The synthesis radio telescope at Westerbork. *Proceedings of the IEEE,* 1973, Vol. 61, Number 9, pp. 1258–1266. DOI https://doi.org/10.1109/PROC.1973.9255.

[95] Casse, J. L. et al. The synthesis radio telescope at Westerbork. The 21 cm continuum receiver system. *Astronomy & Astrophysics,* 1974, Vol. 31. DOI .

[96] Broderick, J. et al. LOFAR observations of MAXI J1820+070 (ASASSN-18ey) during its recent state transition. *The Astronomer's Telegram,* 25 July 2018, Number 11887. Available http://www.astronomerstelegram.org/?read=11887.

[97] van der Horst, A. J. et al. Broad-band monitoring tracing the evolution of the jet and disc in the black hole candidate X-ray binary MAXI J1659-152. *Monthly Notices of the Royal Astronomical Society,* 2013, Vol. 436, Issue 3, pp. 2625–2638. DOI https://doi.org/10.1093/mnras/stt1767.

[98] Rushton, A. P. et al. Disc–jet quenching of the Galactic black hole Swift J1753.5-0127. *Monthly Notices of the Royal Astronomical Society,* 2016, Vol. 463, Issue 1, pp. 628–634. DOI https://doi.org/10.1093/mnras/stw2020.

[99] Gehrels, N. et al. The *Swift* gamma-ray burst mission. *The Astrophysical Journal,* 2004, Vol. 611, Number 2. DOI https://doi.org/10.1086/422091.

[100] Gehrels, N. et al. Erratum: "The *Swift* gamma-ray burst mission" (ApJ, 611, 1005 [2004]). *The Astrophysical Journal,* 2005, Vol. 621, Number 1. DOI https://doi.org/10.1086/427409.

[101] Bradt, H. V. et al. X-ray Timing Explorer mission. *Astronomy & Astrophysics Supplement Series,* 1993, Vol. 97, pp. 355–360. Available http://articles.adsabs.harvard.edu/pdf/1993A%26AS...97..355B.

[102] NASA's HEASARC: Observatories. The Rossi X-ray Timing Explorer. 4 April 2012. (Online) Accessed 8 August 2019. Available https://heasarc.gsfc.nasa.gov/docs/xte/rxte.html.

[103] Jahoda, K. et al. Calibration of the *Rossi X-Ray Timing Explorer* Proportional Counter Array. *The Astrophysical Journal Supplement Series,* 2006, Vol. 163, Number 2. DOI https://doi.org/10.1086/500659.

[104] Modigliani, A. et al. The X-shooter pipeline. *Proceedings SPIE, Observatory Operations: Strategies, Processes, and Systems III,* 2010, Vol. 7737. DOI https://doi.org/10.1117/12.857211.

[105] Freudling, W. et al. Automated data reduction workflows for astronomy – The ESO Reflex environment. *Astronomy & Astrophysics,* 2013, Vol. 559, Article number A96. DOI https://doi.org/10.1051/0004-6361/201322494.

[106] Smette, A. et al. Molecfit: A general tool for telluric absorption correction I. Method and application to ESO instruments. *Astronomy & Astrophysics,* 2015, Vol. 576, Article number A77. DOI https://doi.org/10.1051/0004-6361/201423932.

[107] Kausch, W. et al. Molecfit: A general tool for telluric absorption correction II. Quantitative evaluation on ESO-VLT/X-Shooter spectra. *Astronomy & Astrophysics,* 2015, Vol. 576, Article number A78. DOI https://doi.org/10.1051/0004-6361/201423909.

[108] Blackburn, J. K. FTOOLS: A FITS data processing and analysis software package. *Astronomical Data Analysis Software and Systems IV: Astronomical Society of the Pacific Conference Series,* 1995, Vol. 77. Available https://www.adass.org/adass/proceedings/adass94/blackburnj.html.

[109] FDUMP – ftools.futils FDUMP. January 1992. (Online) Accessed 11 March 2019. Available https://heasarc.gsfc.nasa.gov/lheasoft/ftools/fhelp/fdump.txt.

[110] MATLAB. *The MathWorks Inc.,* 2019. https://www.mathworks.com/.

[111] Fitzpatrick, E. L. Correcting for the effects of interstellar extinction. *Publications of the Astronomical Society of the Pacific,* 1999, Vol. 111, Number 755. DOI https://doi.org/10.1086/316293.

[112] R Core Team. R: A language and environment for statistical computing. *R Foundation for Statistical Computing,* 2017. https://www.R-project.org/.

[113] Arnab, C. et al. astrolabe: Astronomy Users Library for R. *R Foundation for Statistical Computing,* 2014. http://CRAN.R-project.org/package=astrolibR.

[114] RDocumentation. fm_unred. *R Foundation for Statistical Computing,* 2014. https://www.rdocumentation.org/packages/astrolibR/versions/0.1/topics/fm$_$unred/.

[115] D'Avanzo, P. et al. EM optical/NIR observations of MAXI J1659-152. *The Astronomer's Telegram,* 2 October 2010, Number 2900. Available http://www.astronomerstelegram.org/?read=2900.

[116] Rahoui, F. et al. Optical and near-infrared spectroscopy of the black hole Swift J1753.5-0127. *The Astrophysical Journal,* 2015, Vol. 810, Number 2. DOI https://doi.org/10.1088/0004-637X/810/2/161.

[117] Houck, J. C. & DeNicola, L. A. ISIS: An Interactive Spectral Interpretation System for high resolution X-ray spectroscopy. *Astronomical Data Analysis Software and Systems IX: Astronomical Society of the Pacific Conference Series,* 2000, Vol. 216. Available https://www.adass.org/adass/proceedings/adass99/P2-39/.

[118] The Interactive Spectral Interpretation System. ISIS Home Page. 2 February 2019. (Online) Accessed 11 August 2019. Available http://space.mit.edu/cxc/isis/.

[119] Houck, J. C. ISIS 1.0 Technical Manual. Available https://space.mit.edu/cxc/isis/manual.pdf.

[120] The Interactive Spectral Interpretation System. Loving ISIS – Confessions of a Former XSPEC User. 7 October 2013. (Online) Accessed 14 August 2019. Available https://space.mit.edu/home/mnowak/isis_vs_xspec/.

[121] Nowak, Michael. Private communication. 4 November 2019.

[122] Wilms, J. et al. On the absorption of X-rays in the interstellar medium. *The Astrophysical Journal,* 2000, Vol. 542, Number 2. DOI https://doi.org/10.1086/317016.

[123] Arnaud, K. et al. Xspec: An X-ray spectral fitting package – Users' guide for version 12.11. March 2020. (Online) Accessed 11 March 2020. Available https://heasarc.gsfc.nasa.gov/xanadu/xspec/manual/XspecManual.html.

[124] Arnaud, K. et al. XSPEC Models. (Online) Accessed 11 March 2020. Available https://heasarc.gsfc.nasa.gov/xanadu/xspec/manual/node129.html.

[125] Mitsuda, K. et al. Energy spectra of low-mass binary X-ray sources observed from Tenma. *Publications of the Astronomical Society of Japan,* 1984, Vol. 36. Available https://ui.adsabs.harvard.edu/abs/1984PASJ...36..741M/abstract.

[126] Makishima, K. et al. Simultaneous X-ray and optical observations of GX 339−4 in an X-ray high state. *The Astrophysical Journal,* 1986, Vol. 308. DOI https://doi.org/10.1086/164534.

[127] Gierliński, M. et al. X-ray irradiation in XTE J1817−330 and the inner radius of the truncated disc in the hard state. *Monthly Notices of the Royal Astronomical Society,* 2008, Vol. 388, Issue 2, pp. 753–760. DOI https://doi.org/10.1111/j.1365-2966.2008.13431.x.

[128] Gierliński, M. et al. Reprocessing of X-rays in the outer accretion disc of the black hole binary XTE J1817−330. *Monthly Notices of the Royal Astronomical Society,* 2009, Vol. 392, Issue 3, pp. 1106–1114. DOI https://doi.org/10.1111/j.1365-2966.2008.14166.x.

[129] Fabian, A. C. et al. X-ray fluorescence from the inner disc in Cygnus X-1. *Monthly Notices of the Royal Astronomical Society,* 1989, Vol. 238, Issue 3, pp. 729–736. DOI https://doi.org/10.1093/mnras/238.3.729.

[130] Anders, E. & Grevesse, N. Abundances of the elements: Meteoritic and solar. *Geochimica et Cosmochimica Acta,* 1989, Vol. 53, Issue 1, pp. 197–214. DOI https://doi.org/10.1016/0016-7037(89)90286-X.

[131] Shidatsu, M. et al. X-ray, optical, and near-infrared monitoring of the new X-ray transient MAXI J1820+070 in the low/hard state. *The Astrophysical Journal,* 2018, Vol. 868. DOI https://doi.org/10.3847/1538-4357/aae929.

[132] Shidatsu, M. et al. X-ray and optical monitoring of state transitions in MAXI J1820+070. *The Astrophysical Journal,* 2019, Vol. 874. DOI https://doi.org/10.3847/1538-4357/ab09ff.

[133] Buisson, D. J. K. et al. MAXI J1820+070 with NuSTAR I. An increase in variability frequency but a stable reflection spectrum: Coronal properties and implications for the inner disc in black hole binaries. *Monthly Notices of the Royal Astronomical Society,* 2019, Vol. 490, Issue 1, pp. 1350–1362. DOI https://doi.org/10.1093/mnras/stz2681.

[134] RIKEN, JAXA, MAXI Team. MAXI J1820+070. http://maxi.riken.jp/star_data/J1820+071/J1820+071_00055058g_lc_all.gif.

[135] Veledina, A. et al. Evolving optical polarisation of the black hole X-ray binary MAXI J1820+070. *Astronomy & Astrophysics,* 2019, Vol. 623, Article number A75. DOI https://doi.org/10.1051/0004-6361/201834140.

[136] Kara, E. et al. The corona contracts in a black-hole transient. *Nature,* 2019, Vol. 565, pp. 198–201. DOI https://doi.org/10.1038/s41586-018-0803-x.

[137] Bright, J. S. et al. An extremely powerful long-lived superluminal ejection from the black hole MAXI J1820+070. *Nature Astronomy,* 2020, Vol. 4, pp. 697–703. DOI https://doi.org/10.1038/s41550-020-1023-5.

[138] Kaur, R. et al. Very Large Telescope/X-shooter spectroscopy of the candidate black hole X-ray binary MAXI J1659-152 in outburst. *The Astrophysical Journal Letters,* 2012, Vol. 746, Number 2. DOI https://doi.org/10.1088/2041-8205/746/2/L23.

[139] RIKEN, JAXA, MAXI Team. MAXI J1659-152. http://maxi.riken.jp/star_data/J1659-152/J1659-152_00055058g_lc_all.gif.

[140] Muñoz-Darias, T. et al. The black hole candidate MAXI J1659−152: Spectral and timing analysis during its 2010 outburst. *Monthly Notices of the Royal Astronomical Society,* 2020, Vol. 415, Issue 1, pp. 292–300. DOI https://doi.org/10.1111/j.1365-2966.2011.18702.x.

[141] Kalamkar, M. et al. The identification of MAXI J1659−152 as a black hole candidate. *The Astrophysical Journal Letters,* 2011, Vol. 731, Number 1. DOI https://doi.org/10.1088/2041-8205/731/1/L2.

[142] RIKEN, JAXA, MAXI Team. Swift J1753.5−0127. http://maxi.riken.jp/star_data/J1753-014/J1753-014_00055058g_lc_all.gif.

[143] Schipani, P. et al. The new SOXS instrument for the ESO NTT. *Proceedings SPIE, Ground-based and Airborne Instrumentation for Astronomy VI,* 2016, Vol. 9908. DOI https://doi.org/10.1117/12.2231866.

[144] Claudi, R. et al. The common path of SOXS (Son of X-shooter). *Proceedings SPIE, Ground-based and Airborne Instrumentation for Astronomy VII,* 2016, Vol. 10702. DOI https://doi.org/10.1117/12.2314576.

[145] University of Copenhagen. NOT Transient Explorer (NTE). (Online) Accessed 23 May 2020. Available https://nte.nbi.ku.dk.

A. Appendix A – VISIR and radio data sets

This appendix consists of the VISIR set data values available for MAXI J1820+070 (table A1) which were used in this master's thesis, and all of the radio data values available for all of the targets (table A2) which were used in this master's thesis.

Table A1: The VISIR data values of MAXI J1820+070 (2018-04-12T07)

Frequency [Hz]	Flux [mJy]	Error [mJy]
6.160825e13	270.888	27.0888
3.426606e13	296.607	29.6607
2.805634e13	367.804	36.7804
2.593750e13	378.189	37.8189

Table A2: The radio data set values used in this thesis.

Target	Date	Freq. [Hz]	Flux [mJy]	Err. [mJy]
MAXI J1820+070	2018-04-12	5e9	47.6	0.5
		7e9	49.4	0.4
		9e9	48.8	0.9
		11e9	49.4	1.5
		21e9	56.7	4.2
		26e9	56.1	6.8
		232e9	97	22
		343e9	125	13
		5.3e9	46.0	0.1
		7.5e9	46.6	0.1
		8.5e9	48.	0.2
		11.1e9	49.2	0.2
		20.7e9	58.7	1.1
		25.5e9	60.5	1.1
		226.6e9	110.6	3.7
		234.6e9	114.5	4.7
		336.4e9	119.9	0.2
		338.4e9	120.5	0.2
		348.4e9	121.1	0.2
		350.4e9	121.0	0.2
	2018-07-13	136.5e6	14.7	5.1
	2018-09-29	228.1e9	3.0	0.6
MAXI J1659-152	2010-09-25	4.9e9	5.39	0.05
	2010-09-26	3.45e11	15.8	3.0
SWIFT J1753.5-0127	2014-08-17	1.5e11	0.2585	0.002585
GRS 1915+105	2010-09-25	4.8e9	39	3.9

B. Appendix B – Molecfit driver

```
\#\#\# Driver for MOLECFIT
\# user working directory only important for REFLEX workflow and GUI
\# not used by molecfit itself.
user\_workdir: /home/abinios/data\_wkf/reflex\_end\_products/MAXI\_J1820/File\_name.tpl
\#\# INPUT DATA
\# Data file name (path relative to the current directory or absolute path)
filename: /home/abinios/data\_wkf/reflex\_end\_products/MAXI\_J1820/File\_name.fits
\# ASCII list of files to be corrected for telluric absorption using the
\# transmission curve derived from the input reference file (path of list and
\# listed files relative to the current directory or absolute path; default: "none")
listname: none
\# Type of input spectrum -- 1 = transmission (default); 0 = emission
trans: 1
\# Names of the file columns (table) or extensions (image) containing:
\# Wavelength  Flux  Flux\_Err  Mask
\# - Flux\_Err and/or Mask can be avoided by writing 'NULL'
\# - 'NULL' is required for Wavelength if it is given by header keywords
\# - parameter list: col\_lam, col\_flux, col\_dflux, and col\_mask
columns: WAVE FLUX ERR QUAL
\# Default error relative to mean for the case that the error column is missing
default\_error: 0.01
\# Multiplicative factor to convert wavelength to micron
\# (e.g. nm -> wlgtomicron = 1e-3)
wlgtomicron: 0.001
\# Wavelengths in vacuum (= vac) or air (= air)
vac\_air: air
\# ASCII or FITS table for wavelength ranges in micron to be fitted
\# (path relative to the current directory or absolute path; default: "none")
wrange\_include: /home/abinios/Downloads/include\_xshoo\_vis.dat
\# ASCII or FITS table for wavelength ranges in micron to be excluded from the
\# fit (path relative to the current directory or absolute path; default: "none")
wrange\_exclude: none
\# ASCII or FITS table for pixel ranges to be excluded from the fit
\# (path relative to the current directory or absolute path; default: "none")
prange\_exclude: /home/abinios/Downloads/exclude\_xshoo\_vis.dat
\#\# RESULTS
\# Directory for output files (path relative to the current directory or absolute path)
output\_dir: /home/abinios/molecfit-output
\# Name for output files
\# (supplemented by "\_fit" or "\_tac" as well as ".asc", ".atm", ".fits",
\# ".par, ".ps", and ".res")
output\_name: molecfit\_xshoo\_vis\_1
\# Plot creation: gnuplot is used to create control plots
\# W - screen output only (incorporating wxt terminal in gnuplot)
\# X - screen output only (incorporating x11 terminal in gnuplot)
\# P - postscript file labelled '<output\_name>.ps', stored in <output\_dir>
\# combinations possible, i.e. WP, WX, XP, WXP (however, keep the order!)
\# all other input: no plot creation is performed
plot\_creation: none
\# Create plots for individual fit ranges? -- 1 = yes; 0 = no
plot\_range: 0
\#\# FIT PRECISION
\# Relative chi2 convergence criterion
ftol: 0.001
\# Relative parameter convergence criterion
xtol: 0.001
\#\# MOLECULAR COLUMNS
\# List of molecules to be included in the model
\# (default: 'H2O', N\_val: nmolec)
list\_molec: H2O O2
\# Fit flags for molecules -- 1 = yes; 0 = no (N\_val: nmolec)
fit\_molec: 1 1
\# Values of molecular columns, expressed relatively to the input ATM profile
\# columns (N\_val: nmolec) [1 = 100\%]
relcol: 1.0 1.0
\#\# BACKGROUND AND CONTINUUM
\# Conversion of fluxes from phot/(s*m2*mum*as2) (emission spectrum only) to
\# flux unit of observed spectrum:
\# 0: phot/(s*m\^{}2*mum*as\^{}2) [no conversion]
\# 1: W/(m\^{}2*mum*as\^{}2)
\# 2: erg/(s*cm\^{}2*A*as\^{}2)
\# 3: mJy/as\^{}2
\# For other units the conversion factor has to be considered as constant term
\# of the continuum fit.
flux\_unit: 0
\# Fit of telescope background -- 1 = yes; 0 = no (emission spectrum only)
fit\_back: 0
\# Initial value for telescope background fit (range: [0,1])
```

```
telback: 0.1
\# Polynomial fit of continuum --> degree: cont\_n
fit\_cont: 1
\# Degree of coefficients for continuum fit
cont\_n: 3
\# Initial constant term for continuum fit (valid for all fit ranges)
\# (emission spectrum: about 1 for correct flux\_unit)
cont\_const: 5e-14
\#\# WAVELENGTH SOLUTION
\# Refinement of wavelength solution using a polynomial of degree wlc\_n
fit\_wlc: 1
\# Polynomial degree of the refined wavelength solution
wlc\_n: 0
\# Initial constant term for wavelength correction (shift relative to half
\# wavelength range)
wlc\_const: 0.0
\#\# RESOLUTION
\# Fit resolution by boxcar -- 1 = yes; 0 = no
fit\_res\_box: 0
\# Initial value for FWHM of boxcar relative to slit width (>= 0. and <= 2.)
relres\_box: 0.0
\# Voigt profile approximation instead of independent Gaussian and Lorentzian
\# kernels? -- 1 = yes; 0 = no
kernmode: 0
\# Fit resolution by Gaussian -- 1 = yes; 0 = no
fit\_res\_gauss: 1
\# Initial value for FWHM of Gaussian in pixels
res\_gauss: 1.0
\# Fit resolution by Lorentzian -- 1 = yes; 0 = no
fit\_res\_lorentz: 0
\# Initial value for FWHM of Lorentzian in pixels
res\_lorentz: 0.5
\# Size of Gaussian/Lorentzian/Voigtian kernel in FWHM
kernfac: 30.0
\# Variable kernel (linear increase with wavelength)? -- 1 = yes; 0 = no
varkern: 1
\# ASCII file for kernel elements (one per line; normalisation not required)
\# instead of synthetic kernel consisting of boxcar, Gaussian, and Lorentzian
\# components (path relative to the current directory or absolute path; default: "none")
kernel\_file: none
\#\# AMBIENT PARAMETERS
\# If the input data file contains a suitable FITS header, the keyword names of
\# the following parameters will be read, but the corresponding values will not
\# be used. The reading of parameter values from this file can be forced by
\# setting keywords to NONE.
\# Observing date in years or MJD in days
obsdate
obsdate\_key
\# UTC in s
utc
utc\_key
\# Telescope altitude angle in deg
telalt
telalt\_key
\# Humidity in \%
rhum
rhum\_key
\# Pressure in hPa
pres
pres\_key
\# Ambient temperature in deg C
temp
temp\_key
\# Mirror temperature in deg C
m1temp
m1temp\_key
\# Elevation above sea level in m (default is Paranal: 2635m)
geoelev
geoelev\_key
\# Longitude (default is Paranal: -70.4051)
longitude
longitude\_key
\# Latitude (default is Paranal: -24.6276)
latitude
latitude\_key
\#\# INSTRUMENTAL PARAMETERS
\# Slit width in arcsec (taken from FITS header if present)
slitw: 0.9
slitw\_key: ESO INS SLIT1 WID
\# Pixel scale in arcsec (taken from this file only)
pixsc: 0.16
pixsc\_key: NONE
\#\# ATMOSPHERIC PROFILES
```

```
\# Reference atmospheric profile
ref\_atm: equ.atm
\# Specific GDAS-like input profile (P[hPa] HGT[m] T[K] RELHUM[\%]) (path
\# relative to the installation directory or absolute path). In the case of "none", no GDAS
\# profiles will be considered. The default "auto" performs an automatic
\# retrieval.
gdas\_dir: data/profiles/grib
gdas\_prof: auto
\# Grid of layer heights for merging ref\_atm and GDAS profile. Fixed grid = 1
\# (default) and natural grid = 0.
layers: 1
\# Upper mixing height in km (default: 5) for considering data of a local meteo
\# station. If emix is below geoelev, rhum, pres, and temp are not used for
\# modifying the corresponding profiles.
emix: 5.0
\# PWV value in mm for the input water vapour profile. The merged profile
\# composed of ref\_atm, GDAS, and local meteo data will be scaled to this value
\# if pwv > 0 (default: -1 -> no scaling).
pwv: -1.
\# internal GUI specific parameter
clean\_mflux: 1
end
```

C. Appendix C – Data reduction scripts

This appendix consists of examples to perform a file format conversion from FITS to ASCII files, an example to screen the X-shooter data sets, convert the units and combine the data sets as a single file with Matlab, and an example to perform interstellar extinction corrections with R.

FTOOLS fdump file format conversion from FITS to ASCII example

```
fdump ORIGINAL_XSHOOTER_UVB.fits ASCII_XSHOOTER_UVB.asc
columns=@colnames.lis rows=- prhead=no
```

where the file **colnames.lis** is defined as

```
WAVE
FLUX
```

Matlab script for data screening

```
Lambda1=table2array(lambda1);                    % From ASCII file
Flux1=table2array(flux1);
Lambda2=table2array(lambda2);                    % From ASCII file
Flux2=table2array(flux2);
Lambda3a=table2array(lambda3);                   % From ASCII file
Lambda3=Lambda3a/1000;
Flux3=table2array(flux3);
figure()
plot(Lambda1,Flux1);
hold on
plot(Lambda2,Flux2);
hold on
plot(Lambda3,Flux3);
% Regions to be included
LambdaNIRa=Lambda1(387:1260);                % 1.0175--1.07
LambdaNIRb=Lambda1(3262:4645);               % 1.19--1.273
LambdaNIRc=Lambda1(8761:12260);              % 1.52--1.73
LambdaNIRd=Lambda1(17092:22424);             % 2.02--2.34
LambdaNIR=[LambdaNIRa; LambdaNIRb; LambdaNIRc; LambdaNIRd]
FluxNIRa=Flux1(387:1260);
FluxNIRb=Flux1(3262:4645);
FluxNIRc=Flux1(8761:12260);
FluxNIRd=Flux1(17092:22424);
FluxNIR=[FluxNIRa; FluxNIRb; FluxNIRc; FluxNIRd]
LambdaVISa=Lambda2(1058:2612);            % 0.555--0.586
LambdaVISb=Lambda2(2818:4561);            % 0.590--0.625
LambdaVISc=Lambda2(5207:5811);            % 0.638--0.650
LambdaVISd=Lambda2(6807:7611);            % 0.670--0.686
LambdaVISe=Lambda2(8006:8510);            % 0.694--0.704
LambdaVISf=Lambda2(8756:9060);            % 0.709--0.715
LambdaVISg=Lambda2(9806:11060);           % 0.730--0.755
LambdaVISh=Lambda2(11805:13809);          % 0.770--0.810
LambdaVISi=Lambda2(21353:23306);          % 0.961--1.000
LambdaVIS=[LambdaVISa; LambdaVISb; LambdaVISc; LambdaVISd; LambdaVISe; LambdaVISf; LambdaVISg; LambdaVISh; LambdaVISi]
FluxVISa=Flux2(1058:2612);
```

```
FluxVISb=Flux2(2818:4561);
FluxVISc=Flux2(5207:5811);
FluxVISd=Flux2(6807:7611);
FluxVISe=Flux2(8006:8510);
FluxVISf=Flux2(8756:9060);
FluxVISg=Flux2(9806:11060);
FluxVISh=Flux2(11805:13809);
FluxVISi=Flux2(21353:23306);
FluxVIS=[FluxVISa; FluxVISb; FluxVISc; FluxVISd; FluxVISe; FluxVISf; FluxVISg; FluxVISh; FluxVISi]
angNIR=10^4*LambdaNIR;                          % Microns to Ångströms
angVIS=10^4*LambdaVIS;                          % Microns to Ångströms
angUVB=10^4*Lambda3;
ang2NIR=angNIR.*angNIR;
ang2VIS=angVIS.*angVIS;
ang2UVB=angUVB.*angUVB;
JyNIR=3.34*(10^4)*ang2NIR.*FluxNIR;
mJyNIR=3.34*(10^7)*ang2NIR.*FluxNIR;
JyVIS=3.34*(10^4)*ang2VIS.*FluxVIS;
mJyVIS=3.34*(10^7)*ang2VIS.*FluxVIS;
c=299792458;
metriNIR=LambdaNIR*10^-6;                % Wavelength in meters
metriVIS=LambdaVIS*10^-6;                % Wavelength in meters
metriUVB=Lambda3*10^-6;                  % Wavelength in meters
HzNIR=c./metriNIR;
HzVIS1=c./metriVIS;
HzVIS=HzVIS1(859:10733);
JanskyUVB=3.33564095e+4.*Flux3.*ang2UVB;        % Jansky conversion
mJanskyUVB1=3.33564095e+7.*Flux3.*ang2UVB;      % Millijansky conversion
Freq3=c./metriUVB;
Freq3a=Freq3(832:2185);
Freq3b=Freq3(2383:3559);
Freq3c=Freq3(4974:5448);
Freq3d=Freq3(5645:6684);
Freq3e=Freq3(6842:8097);
Freq3f=Freq3(8697:9231);
Freq3g=Freq3(9467:9587);
Freq3h=Freq3(10417:11965);
HzUVB=[Freq3a; Freq3b; Freq3c; Freq3d; Freq3e; Freq3f; Freq3g; Freq3h]
Hz=[HzNIR; HzVIS; HzUVB];
JanskyNIR=3.33564095e+4.*FluxNIR.*ang2NIR;        % Jansky conversion
mJanskyNIR=3.33564095e+7.*FluxNIR.*ang2NIR;       % Millijansky conversion
JanskyVIS=3.33564095e+4.*FluxVIS.*ang2VIS;        % Jansky conversion
mJanskyVIS1=3.33564095e+7.*FluxVIS.*ang2VIS;      % Millijansky conversion
mJanskyVIS=mJanskyVIS1(859:10733);
Flux3a=mJanskyUVB1(832:2185);                           % 8.75--9.50
Flux3b=mJanskyUVB1(2383:3559);                          % 8.65--8.10
Flux3c=mJanskyUVB1(4974:5448);                          % 7.525--7.35
Flux3d=mJanskyUVB1(5645:6684);                          % 7.28--6.93
Flux3e=mJanskyUVB1(6842:8097);                          % 6.88--6.505
Flux3f=mJanskyUVB1(8697:9231);                          % 6.34--6.2
Flux3g=mJanskyUVB1(9467:9587);                          % 6.11--6.14
Flux3h=mJanskyUVB1(10417:11965);                        % 5.91--5.57
mJanskyUVB=[Flux3a; Flux3b; Flux3c; Flux3d; Flux3e; Flux3f; Flux3g; Flux3h]
mJansky=[mJanskyNIR; mJanskyVIS; mJanskyUVB];
error=0.01*mJansky;
out=[Hz, mJansky, error];
save('MJ1820-10-01T01.txt', 'out', '-ascii')
type('MJ1820-10-01T01.txt')
out=[Hz, mJansky, error];
save('MJ1820-10-01T01.dat', 'out', '-ascii')
type('MJ1820-10-01T01.dat')
```

Example of fm_unred

```
require("astrolibR");
data <- read.table("X-shooter_data.dat");
wavelength <- 299792458/data[,1];
flux <- data[,2];
flux_unred <- fm_unred(wavelength,flux,0.163)$funred;
frequency <- 299792458/wave
flux_err <- flux_unred*0.1
plot(frequency,flux_unred);
d <- cbind(frequency,flux_unred,flux_err);
write.table(d,"X-shooter_data_unred.txt",col.names=FALSE,row.names=FALSE,sep=" ");
```

D. Appendix D – ISIS example scripts

This appendix consists of two examples that can be used to perform spectral analysis with the Interactive Spectral Interpretation System. The first example is for multiwavelength data sets that have *Swift*–XRT X-ray data, and the second is for multiwavelength data sets that have *RXTE*–PCA X-ray data.

Example for *Swift*–XRT observations

```
Rmf_OGIP_Compliance=0;
variable xrt = load_data("Swift-X-ray-data.pha");
variable temp1 = read_radio("Radio-data.dat", 100);
variable radio1 = load_radio(temp1);
variable temp2 = read_radio("X-shooter-unreddened-data.txt", 100);
variable radio2 = load_radio(temp2);
variable temp3 = read_radio("VISIR-data.dat", 100);
variable radio3 = load_radio(temp3);
group(xrt;min_sn=[20.,20.,20.,20.,10.],bounds=[0.5,1.5,1.8,3.,6.],unit="kev");
notice_values(xrt,0.3,10.;unit="kev");
xspec_abund("wilm");
xlog;
ylog;
load_par("Spectral_model.par");
eval_counts;
fancy_plot_unit("Hz","mJy");
plot_unfold({1,2,3,4};power=2,res=3);
```

Example for *RXTE*–PCA observations

```
variable pca = load_data("Rossi-X-ray-data.pha");
variable temp1 = read_radio("GRS24_unredtrim1.txt", 100);
variable temp1 = read_radio("Radio-data.dat", 100);
variable radio1 = load_radio(temp1);
variable temp2 = read_radio("X-shooter-unreddened-data.txt", 100);
variable radio2 = load_radio(temp2);
set_sys_err_frac(pca,Double_Type[129]+0.005);
group(pca;min_sn=[5.5],unit="kev");
notice_values(pca,3.5,22.;unit="kev");
xspec_abund("wilm");
xlog;
ylog;
load_par("Spectral_model.par");
eval_counts;
fancy_plot_unit("Hz","mJy");
plot_unfold({1,2,3};power=2,res=3);
```

E. Appendix E – Best-fit model parameters

This appendix gives all of the optimised best-fit model parameters for the targets.

MAXI J1820+070

2018-04-12

tbabs(1)*(bknpower(1)+diskir(1)+diskline(1))

idx	param	tie-to	freeze	value	min	max	
1	tbabs(1).nH	0	0	0.08828035	0.07750182	0.1014959	10^22
2	bknpower(1).norm	0	0	4611.046	4558.889	4665.101	
3	bknpower(1).PhoIndx1	0	0	0.7598575	0.7590989	0.7605986	
4	bknpower(1).BreakE	0	0	0.0001650306	0.0001182442	0.0001900229	keV
5	bknpower(1).PhoIndx2	0	0	2.148686	1.872561	2.32051	
6	diskir(1).norm	0	0	76634	57191.31	103548.7	
7	diskir(1).kT_disk	0	0	0.3384056	0.3163212	0.3632103	keV
8	diskir(1).Gamma	0	0	1.559569	1.419412	1.777209	
9	diskir(1).kT_e	0	0	5	5	7.583663	keV
10	diskir(1).LcovrLd	0	0	3.113699	2.494599	4.38298	
11	diskir(1).fin	0	1	0.1	0	1	
12	diskir(1).rirr	0	0	1.013237	1.009057	1.017379	
13	diskir(1).fout	0	0	0.01037896	0.007147462	0.0162959	
14	diskir(1).logrout	0	0	4.191154	4.074932	4.301831	
15	diskline(1).norm	0	0	0.1128261	0.05817229	0.1950677	
16	diskline(1).LineE	0	0	6.611024	6.305218	6.86476	keV
17	diskline(1).Betor10	0	1	-2	-10	20	
18	diskline(1).Rin_M	0	1	10	6	1000	
19	diskline(1).Rout_M	0	1	1000	0	1000000	
20	diskline(1).Incl	0	0	55.05528	30.63712	90	deg

Parameters[Variable] = 20[16]
Data bins = 213
Chi-square = 1235.985
Reduced chi-square = 6.274033

2018-07-13

tbabs(1)*(diskir(1)+bbody(1))

idx	param	tie-to	freeze	value	min	max	
1	tbabs(1).nH	0	0	0.0930217	0.09078039	0.09530791	10^22
2	diskir(1).norm	0	0	17931.38	17480.72	18403.46	
3	diskir(1).kT_disk	0	0	0.7762191	0.7706991	0.7816693	keV
4	diskir(1).Gamma	0	1	2	1.001	5	
5	diskir(1).kT_e	0	1	100	5	1000	keV
6	diskir(1).LcovrLd	0	0	0.1917358	0.1734942	0.2102924	
7	diskir(1).fin	0	1	0.1	0	1	
8	diskir(1).rirr	0	1	10	1.0001	10	
9	diskir(1).fout	0	1	0.0002968439	0	0.1	
10	diskir(1).logrout	0	0	4.961119	4.936631	4.981515	
11	bbody(1).norm	0	0	0.748578	0.0421728	38.11862	
12	bbody(1).kT	0	0	0.01151433	0.004046854	0.02134383	keV

Parameters[Variable] = 12[7]
Data bins = 358
Chi-square = 735.4182
Reduced chi-square = 2.095209

2018-07-13 (without bbody)

tbabs(1)*(diskir(1))

idx	param	tie-to	freeze	value	min	max	
1	tbabs(1).nH	0	0	0.09346688	0	100000	10^22
2	diskir(1).norm	0	0	17903.98	0	1e+10	
3	diskir(1).kT_disk	0	0	0.7762215	0.01	5	keV
4	diskir(1).Gamma	0	1	2	1.001	5	
5	diskir(1).kT_e	0	1	100	5	1000	keV
6	diskir(1).LcovrLd	0	0	0.1918338	0	10	
7	diskir(1).fin	0	1	0.1	0	1	
8	diskir(1).rirr	0	1	10	1.0001	10	
9	diskir(1).fout	0	0	0.0008994993	0	0.1	
10	diskir(1).logrout	0	0	4.78948	3	7	

Parameters[Variable] = 10[6]
Data bins = 358
Chi-square = 846.5676
Reduced chi-square = 2.405021

2018-07-13 (without bbody, and without UVB region)

```
tbabs(1)*diskir(1)
 idx  param          tie-to  freeze         value         min         max
  1  tbabs(1).nH         0     0         0.093272           0      100000  10^22
  2  diskir(1).norm      0     0            17903           0       1e+10
  3  diskir(1).kT_disk   0     0        0.7763482        0.01           5  keV
  4  diskir(1).Gamma     0     1                2       1.001           5
  5  diskir(1).kT_e      0     1              100           5        1000  keV
  6  diskir(1).LcovrLd   0     0        0.1915108           0          10
  7  diskir(1).fin       0     1              0.1           0           1
  8  diskir(1).rirr      0     1               10      1.0001          10
  9  diskir(1).fout      0     0     0.0006846129           0         0.1
 10  diskir(1).logrout   0     0         4.848696           3           7

 Parameters[Variable] = 10[6]
           Data bins = 350
          Chi-square = 760.5315
   Reduced chi-square = 2.210847
```

2018-07-14

```
tbabs(1)*(diskir(1)+bbody(1))
 idx  param          tie-to  freeze         value         min         max
  1  tbabs(1).nH         0     0       0.08985111  0.08674338  0.09303858  10^22
  2  diskir(1).norm      0     0         15013.74    14493.84    15566.71
  3  diskir(1).kT_disk   0     0        0.7794718   0.7717016   0.7871246  keV
  4  diskir(1).Gamma     0     1                2       1.001           5
  5  diskir(1).kT_e      0     1              100           5        1000  keV
  6  diskir(1).LcovrLd   0     0        0.1887792   0.1623034   0.2159829
  7  diskir(1).fin       0     1              0.1           0           1
  8  diskir(1).rirr      0     1               10      1.0001          10
  9  diskir(1).fout      0     0     0.0002639123  0.0001041959  0.0004606458
 10  diskir(1).logrout   0     0         5.013247    5.013247    5.125368
 11  bbody(1).norm       0     0       0.01762055  0.007014656    37.27237
 12  bbody(1).kT         0     0      0.002587555  0.001490755  0.02255907  keV

 Parameters[Variable] = 12[8]
           Data bins = 298
          Chi-square = 349.1348
   Reduced chi-square = 1.203913
```

2018-07-15

```
tbabs(1)*(diskir(1)+bbody(1))
 idx  param          tie-to  freeze         value         min         max
  1  tbabs(1).nH         0     0       0.08876626  0.08070388  0.09810068  10^22
  2  diskir(1).norm      0     0         15844.09    14494.71    17446.87
  3  diskir(1).kT_disk   0     0        0.7860251   0.7639191   0.8073711  keV
  4  diskir(1).Gamma     0     1                2       1.001           5
  5  diskir(1).kT_e      0     1              100           5        1000  keV
  6  diskir(1).LcovrLd   0     0        0.1395613  0.04718627   0.2361346
  7  diskir(1).fin       0     1              0.1           0           1
  8  diskir(1).rirr      0     1               10      1.0001          10
  9  diskir(1).fout      0     0     0.0003808898  0.0003252206  0.0004466219
 10  diskir(1).logrout   0     0         4.985968    4.069576    5.062237
 11  bbody(1).norm       0     0         5.412919  0.008137513    8.103516
 12  bbody(1).kT         0     0       0.02385826  0.001821116  0.02724851  keV

 Parameters[Variable] = 12[8]
           Data bins = 145
          Chi-square = 116.7643
   Reduced chi-square = 0.852294
```

2018-09-30T00

```
tbabs(1)*(diskir(1)+bbody(1))
 idx  param          tie-to  freeze         value         min         max
  1  tbabs(1).nH         0     0       0.04711295  0.04485214  0.04887041  10^22
  2  diskir(1).norm      0     0         72938.72    36942.76    75349.79
  3  diskir(1).kT_disk   0     0        0.2006855   0.1792004   0.2355726  keV
  4  diskir(1).Gamma     0     0         1.795631    1.770019     1.81682
  5  diskir(1).kT_e      0     0         999.9948    112.4451        1000  keV
  6  diskir(1).LcovrLd   0     0         8.527477    6.156023          10
  7  diskir(1).fin       0     1              0.1           0           1
  8  diskir(1).rirr      0     0         2.957133    2.229097    3.166369
  9  diskir(1).fout      0     0     0.0002929757  0.0001882914  0.0004343621
 10  diskir(1).logrout   0     0         4.540488      4.4737    4.632254
 11  bbody(1).norm       0     0      0.001744112           0       1e+10
 12  bbody(1).kT         0     0      0.001697877      0.0001           1  keV
```

```
 Parameters[Variable] = 12[11]
           Data bins = 208
          Chi-square = 188.6468
   Reduced chi-square = 0.9575982

2018-09-30T00 (without bbody)

tbabs(1)*diskir(1)
 idx  param          tie-to  freeze         value         min         max
  1  tbabs(1).nH         0     0       0.0779133           0      100000  10^22
  2  diskir(1).norm      0     0        120196.1           0       1e+10
  3  diskir(1).kT_disk   0     0       0.2391319        0.01           5  keV
  4  diskir(1).Gamma     0     0        1.716684       1.001           5
  5  diskir(1).kT_e      0     0               5           5        1000  keV
  6  diskir(1).LcovrLd   0     0       0.9553281           0          10
  7  diskir(1).fin       0     1             0.1           0           1
  8  diskir(1).rirr      0     0        1.004564      1.0001          10
  9  diskir(1).fout      0     0     0.001666271           0         0.1
 10  diskir(1).logrout   0     0        4.198064           3           7

 Parameters[Variable] = 10[9]
           Data bins = 208
          Chi-square = 341.2159
   Reduced chi-square = 1.714653

2018-09-30T00 (without bbody, and without UVB region)

tbabs(1)*diskir(1)
 idx  param          tie-to  freeze         value         min         max
  1  tbabs(1).nH         0     0       0.08082076           0      100000  10^22
  2  diskir(1).norm      0     0         178841.1           0       1e+10
  3  diskir(1).kT_disk   0     0       0.2095066        0.01           5  keV
  4  diskir(1).Gamma     0     0        1.818542       1.001           5
  5  diskir(1).kT_e      0     0               5           5        1000  keV
  6  diskir(1).LcovrLd   0     0        1.310058           0          10
  7  diskir(1).fin       0     0     5.423961e-13           0           1
  8  diskir(1).rirr      0     0        9.999765      1.0001          10
  9  diskir(1).fout      0     0      0.00131684           0         0.1
 10  diskir(1).logrout   0     0        4.179142           3           7

 Parameters[Variable] = 10[10]
           Data bins = 200
          Chi-square = 265.929
   Reduced chi-square = 1.399626

2018-09-30T01

tbabs(1)*(diskir(1)+bbody(1))
 idx  param          tie-to  freeze         value         min         max
  1  tbabs(1).nH         0     0       0.04707241  0.03818924  0.05296685  10^22
  2  diskir(1).norm      0     0         72598.81    38811.28      145770
  3  diskir(1).kT_disk   0     0        0.2007945   0.1740806   0.2300704  keV
  4  diskir(1).Gamma     0     0        1.795318    1.768236    1.815794
  5  diskir(1).kT_e      0     0        999.8938    112.4933        1000  keV
  6  diskir(1).LcovrLd   0     0        8.555967    6.083235          10
  7  diskir(1).fin       0     1             0.1           0           1
  8  diskir(1).rirr      0     0        2.962846    2.101469    3.111072
  9  diskir(1).fout      0     0     0.0003398773  0.0002189472  0.0005169742
 10  diskir(1).logrout   0     0        4.550743    4.385068     4.67901
 11  bbody(1).norm       0     0      0.002596926           0       1e+10
 12  bbody(1).kT         0     0      0.001899686      0.0001           1  keV

 Parameters[Variable] = 12[11]
           Data bins = 208
          Chi-square = 187.3683
   Reduced chi-square = 0.9511082

2018-10-01

tbabs(1)*(diskir(1)+bbody(1))
 idx  param          tie-to  freeze         value         min         max
  1  tbabs(1).nH         0     0       0.05144583  0.04257649  0.06153916  10^22
  2  diskir(1).norm      0     0         64891.09    31103.78      307161
  3  diskir(1).kT_disk   0     0        0.1933175    0.139348   0.2358804  keV
  4  diskir(1).Gamma     0     0        1.796626    1.756124    1.822771
  5  diskir(1).kT_e      0     0        382.2656    21.55651        1000  keV
  6  diskir(1).LcovrLd   0     0              10    4.429672          10
  7  diskir(1).fin       0     1             0.1           0           1
  8  diskir(1).rirr      0     0        3.333459    1.684683    5.078441
  9  diskir(1).fout      0     0     0.0002797058  0.0001972762  0.0003797695
 10  diskir(1).logrout   0     0        4.605907    4.259178    4.715989
 11  bbody(1).norm       0     0      0.001721017           0       1e+10
 12  bbody(1).kT         0     0      0.001818688      0.0001           1  keV
```

```
 Parameters[Variable] = 12[11]
           Data bins = 176
          Chi-square = 149.2387
   Reduced chi-square = 0.9044767

MAXI J1659-152

2010-09-25

tbabs(1)*(bknpower(1)+diskir(1)+diskline(1))
 idx  param             tie-to  freeze         value         min         max
  1  tbabs(1).nH            0     0        0.3790494   0.3780766   0.3803777  10^22
  2  bknpower(1).norm       0     0         187.9984    185.2918    191.436
  3  bknpower(1).PhoIndx1   0     0        0.8233322   0.8207864   0.824899
  4  bknpower(1).BreakE     0     0     1.430314e-06  1.157793e-06  1.965032e-06  keV
  5  bknpower(1).PhoIndx2   0     0         1.790921    1.772309    1.86305
  6  diskir(1).norm         0     0         214485.1    212781.6    215928.4
  7  diskir(1).kT_disk      0     0        0.1308818   0.1303276   0.131053  keV
  8  diskir(1).Gamma        0     0         1.699649    1.695608    1.703279
  9  diskir(1).kT_e         0     0          6.02297    5.792491     6.05627  keV
 10  diskir(1).LcovrLd      0     0         3.146342    3.139681    3.153056
 11  diskir(1).fin          0     1              0.1           0           1
 12  diskir(1).rirr         0     0         9.999812    9.144158          10
 13  diskir(1).fout         0     0      0.005361542  0.004983243  0.005672867
 14  diskir(1).logrout      0     0                3           3    3.037169
 15  diskline(1).norm       0     0      0.003687299  0.003330557  0.004045031
 16  diskline(1).LineE      0     0         6.008127    5.904781    6.111098  keV
 17  diskline(1).Betor10    0     1               -2         -10          20
 18  diskline(1).Rin_M      0     1               10           6        1000
 19  diskline(1).Rout_M     0     1             1000           0     1000000
 20  diskline(1).Incl       0     0         89.99949    78.79598          90  deg

 Parameters[Variable] = 20[16]
           Data bins = 606
          Chi-square = 983.9932
   Reduced chi-square = 1.667785

SWIFT J1753.5-0127

2014-08-16

tbabs(1)*diskir(1)
 idx  param          tie-to  freeze         value         min         max
  1  tbabs(1).nH         0     0        0.3821068   0.3407073   0.4264585  10^22
  2  diskir(1).norm      0     0          6812765     4853334     7654581
  3  diskir(1).kT_disk   0     0       0.06232882  0.05916369  0.07087187  keV
  4  diskir(1).Gamma     0     0          1.74886    1.709075    1.789594
  5  diskir(1).kT_e      0     0         916.5713           5        1000  keV
  6  diskir(1).LcovrLd   0     0        0.9326608   0.3310955     1.09364
  7  diskir(1).fin       0     0        0.1348308  0.08419424   0.4946617
  8  diskir(1).rirr      0     0         1.011868     1.00536    1.026517
  9  diskir(1).fout      0     0                0           0  5.231008e-05
 10  diskir(1).logrout   0     0                3           3    3.071526

 Parameters[Variable] = 10[10]
           Data bins = 153
          Chi-square = 156.9348
   Reduced chi-square = 1.097446

2014-08-17

tbabs(1)*diskir(1)
 idx  param          tie-to  freeze         value         min         max
  1  tbabs(1).nH         0     0         0.359613    0.321428   0.4106716  10^22
  2  diskir(1).norm      0     0          8310534     5887586     9400412
  3  diskir(1).kT_disk   0     0       0.05812175  0.05506695  0.06617007  keV
  4  diskir(1).Gamma     0     0          1.739939    1.699895    1.782373
  5  diskir(1).kT_e      0     0          831.3374           5        1000  keV
  6  diskir(1).LcovrLd   0     0         1.030523   0.3590373    1.181807
  7  diskir(1).fin       0     0        0.1194478  0.06973042   0.2188824
  8  diskir(1).rirr      0     0         1.008587    1.003641    1.020067
  9  diskir(1).fout      0     0                0           0  4.854868e-05
 10  diskir(1).logrout   0     0                3           3    3.073424

 Parameters[Variable] = 12[11]
           Data bins = 208
          Chi-square = 213.0965
   Reduced chi-square = 1.081708
```

GRS 1915+105

2010-09-19

tbabs(1)*diskir(1)

idx	param	tie-to	freeze	value	min	max	
1	tbabs(1).nH	0	0	17.39675	14.15082	19.99987	10^22
2	diskir(1).norm	0	0	162473.9	90623.2	275937	
3	diskir(1).kT_disk	0	0	0.4701988	0.4376658	0.495362	keV
4	diskir(1).Gamma	0	0	1.535496	1.51156	1.639284	
5	diskir(1).kT_e	0	0	5	5	5.360449	keV
6	diskir(1).LcovrLd	0	0	0.06592364	0.04811983	0.09752459	
7	diskir(1).fin	0	0	0.800445	0.6920369	0.85393	
8	diskir(1).rirr	0	0	1.00104	1.000654	1.001749	
9	diskir(1).fout	0	0	0.001768976	0.001084644	0.00460891	
10	diskir(1).logrout	0	0	4.471114	4.321365	4.621019	

Parameters[Variable] = 10[10]
Data bins = 101
Chi-square = 148.75
Reduced chi-square = 1.634615

2010-09-24

tbabs(1)*diskir(1)

idx	param	tie-to	freeze	value	min	max	
1	tbabs(1).nH	0	0	13.52918	10.53086	16.48838	10^22
2	diskir(1).norm	0	0	99948.21	52450.58	201377	
3	diskir(1).kT_disk	0	0	0.5052084	0.4562036	0.5449039	keV
4	diskir(1).Gamma	0	0	1.694894	1.654178	1.86134	
5	diskir(1).kT_e	0	0	5.045435	5	5.772585	keV
6	diskir(1).LcovrLd	0	0	0.1138841	0.07573562	0.1627434	
7	diskir(1).fin	0	0	0.7807946	0.6147639	0.8424759	
8	diskir(1).rirr	0	0	1.003073	1.001713	1.005644	
9	diskir(1).fout	0	0	0.02390643	0.006131565	0.1	
10	diskir(1).logrout	0	0	4.477916	4.263865	4.682714	

Parameters[Variable] = 10[10]
Data bins = 101
Chi-square = 89.55362
Reduced chi-square = 0.9841058